218
5-1-79

Dr. 2517

SAND79-0002
Unlimited Release
UC-21

MASTER

MASTER MASTER

MASTER

Particle Beam Fusion Progress Report October 1977 Through March 1978

Directorate of Pulsed Energy Programs

Sandia Laboratories
energy report

SAND79-0002
Unlimited Release
Printed February 1979

Distribution
Category UC-21

PARTICLE BEAM FUSION PROGRESS REPORT
OCTOBER 1977 THROUGH MARCH 1978

Directorate of Pulsed Energy Programs 4200
Sandia Laboratories
Albuquerque, New Mexico 87185

3-4

CONTENTS

Page

TECHNICAL OVERVIEW (G. Yonas) 11

PULSED POWER RESEARCH 13

  OVERVIEW (T. H. Martin). 13

  MITE-SELF-MAGNETICALLY INSULATED VACUUM TRANSMISSION LINE EXPERIMENT (J. P. VanDevender) 14

    Introduction. 14
    Apparatus 14
    Power and Energy Transport Experiments. 15
    Comparison with Theory. 19
    Conical Transition to the A-K Feed. 20
    High Stress A-K Feed Experiments. 21
    Pinched Beam Studies. 22

  EBFA 22

    Pulse Forming Lines and Switches (D. L. Johnson). 22
    Trigatron Switches (T. H. Martin) 22
    Marx Generator Test Results (T. H. Martin, D. L. Johnson) 23
    Intermediate Storage Capacitor (D. L. Johnson, T. H. Martin, E. L. Neau). 23
    Gas Pressure Transducer Readouts (D. L. Johnson). 23
    Proto II - Reverse Polarity and Prepulse Level (D. L. Johnson, T. H. Martin). . . . 24
    2-Ω Calibration Pulser (E. L. Neau) 24
    Magnetic Flashover Inhibition Using an Externally Applied Magnetic Field (D. H. McDaniel). 25

  REFERENCES 28

EBFA PROJECT. 29

  OVERVIEW (G. W. Barr). 29

  PROJECT MILESTONE SUMMARY (G. W. Barr) 29

  EBFF 29

    Overview (G. W. Barr) 29
    EBFA/EBFF Radiation Calculations (S. Dupree, G. W. Barr). 32
    EBFA Supporting Systems (W. Boyer, M. Aker, J. Harrison). 32

  EBFA-I 34

    "April 78 Baseline" Design (G. W. Barr) 34
    EBFA Tank Structure (M. Aker) 38
    Marx Generator (M. Aker). 40
    Charging System (D. L. Johnson) 40

CONTENTS (cont)

Page

Marx Generator Trigger System (D. L. Johnson) 40
Transfer Switches (D. L. Johnson) 40
Intermediate Stores (M. Aker) 40
Trigatron Switches (M. Aker). 40
Pulse Forming and Pulse Transforming Lines (M. Aker). 40
Power Flow (M. Aker). 41
Front End (M. Aker) 41

EBFA-II (G. W. Barr) 41

THEORETICAL RESEARCH. 43

OVERVIEW (J. R. Freeman) 43

FUSION TARGET PHYSICS. 44

Beam Preconditioned Magnetic Targets (M. M. Widner, A. V. Farnsworth, Jr.). . . . 44
Scaling of Targets Employing Magnetic Thermoinsulation for Proto II (A. V. Farnsworth, Jr., M. M. Widner, L. Baker) 45
Breakeven and High Gain Magnetic Targets (A. V. Farnsworth, Jr.). 47
Central Igniter Magnetic Targets with Voltage Shaping (M. A. Sweeney, A. V. Farnsworth, Jr.) 48
Two-Dimensional Calculations of Magnetic Thermoinsulation Targets (L. Baker, M. M. Widner). 51
Predicted Temperature at Inner Surface of Shock-Focusing Hemispheres (M. A. Sweeney) 52

STANDOFF AND REACTOR RESEARCH. 52

Diode Focusing and Channel Injection (J. W. Poukey, J. P. Quintenz) 52
Return Current Effects (J. R. Freeman, L. Baker, J. W. Poukey, M. M. Widner, P. A. Miller). 53
Beam Combination for Proto II (T. P. Wright). 55
Improved Radiation Transport Treatment for REB Channels (L. Baker). 55
Hoop Stress in Electron-Beam Hybrid Reactor Chamber Walls (M. A. Sweeney) 56
Estimate of Equilibrium Gas Temperature with Repetitive Operation (M. A. Sweeney) 58

DIODE PHYSICS AND POWER FLOW THEORY. 58

Theory of Double Sheaths in Plasmas (K. D. Bergeron). 58
2-D Electromagnetic Particle Code Results for Coax Propagation (J. W. Poukey, K. D. Bergeron). 60

DIODE CODE DEVELOPMENT AND APPLICATION 62

Diode Code Development (J. P. Quintenz) 62
Combined Diode - Monte Carlo Code for Enhanced Deposition (M. M. Widner, J. P. Quintenz). 63
Ion Diode Simulations (J. W. Poukey, J. P. Quintenz). 63
C-Diode Studies (J. P. Quintenz). 66

CONTENTS (cont)

Page

PARTICLE BEAM SOURCE DEVELOPMENT AND THEORY. 67

Collective Acceleration Book (C. L. Olson). 67
IFA Feasibility Experiments (C. L. Olson) 67
Neutralization of Ion Beams in Magnetic Fields (J. W. Poukey, S. Humphries, Jr.). 68

REFERENCES 69

PARTICLE BEAM SOURCE DEVELOPMENT. 73

OVERVIEW 73

REB CONCENTRATION STUDIES (P. A. Miller, C. W. Mendel, S. A. Goldstein). 73

Multiple Cathode Arrays 75
"Rudakov-Type" Diode Research 75
Pinching Experiments on Both Thick and Thin Flat Targets. 76

CONVOLUTED FEED FOR THE PROTO I ACCELERATOR AND OPTIMIZATION FOR SINGLE-SIDED OPERATION (PROTO I') (S. A. Goldstein, C. W. Mendel). 77

Vacuum Convolute. 78
Oil Convolute 78

NONLINEAR PULSE POWER CIRCUIT ELEMENTS (C. W. Mendel, S. Humphries, Jr.) 81

Introduction. 81
Current Regulator 81
Voltage Regulation. 81

PROTO I SEMISPHERICAL MAGNETICALLY INSULATED ION DIODE (D. J. Johnson, G. W. Kuswa). 83

Introduction. 83
Work Accomplished 83

HIGH CURRENT LINEAR ION ACCELERATOR DEVELOPMENT (S. Humphries, Jr.). 88

Introduction. 88
Beam Neutralization 88
Application of Principles 88
Electron Sources. 88
Pulsed Power Developments 90
Magnetic Insulation Results 90
Injector Studies. 91

PROGRESS ON A FIVE-FRAME X-RAY PINHOLE CAMERA (D. L. Fehl) 93

Introduction. 93
The Five-Frame Camera 93
Future Plans. 93

THE 3 NS PULSED D-T NEUTRON SOURCE (J. Chang, R. J. Leeper). 94

REFERENCES 96

CONTENTS (cont)

Page

TARGET INTERACTION 97

OVERVIEW (A. J. Toepfer) 97

PREHEATED ELECTRON-BEAM TARGET EXPERIMENTS AND SIMULATION (J. N. Olsen, M. M. Widner) 97

MAGNETICALLY INSULATED ("ϕ") TARGET FABRICATION (J. T. Chang). 101

Parylene. 101
Polyimide 102

IMPLOSIONS PHYSICS (F. C. Perry, L. P. Mix, A. J. Toepfer) 103

SCINTILLATOR-PHOTOMULTIPLER RESPONSE TO A SIMULATED REB GENERATOR DT THERMONUCLEAR NEUTRON PULSE 105

DT Thermonuclear Neutron-Signature (R. J. Leeper, J. T. Chang). 105
Monte Carlo Neutron Transport Scintillator Response Calculations (R. J. Leeper) . 106
Monte Carlo Neutron Spectrometer Calculations (R. J. Leeper). 107

REFERENCES 109

APPLICATIONS. 111

REP-RATE PULSE POWER TECHNOLOGY. 111

Overview (K. R. Prestwich). 111

RTF-I, 300-J, 100-pps TEST FACILITY EXPERIMENTS. 112

Data Acquisition System for RTF-I (M. T. Buttram) 112
High Voltage Spark Gap Stability Experiment (M. T. Buttram) 113
Spark Gap Electrode Erosion Experiments (M. T. Buttram, G. J. Rohwein). 114
Liquid-Cooled Rail Gap Switch Design (G. J. Rohwein). 116

TRANSFORMER DEVELOPMENT (G. J. Rohwein). 116

Exposed Primary Transformer 116
3-MV Transformer. 116
Repetitively Pulsed Marx Generator Design Studies 117

REACTOR SYSTEM STUDIES 119

Overview (D. L. Cook, K. R. Prestwich). 119

GENERAL CONCEPTUAL DESIGN 120

Beam Injection Geometry (D. L. Cook). 120
Power Flow Efficiencies (D. L. Cook). 121
X-ray and Debris Attenuation (D. L. Cook, M. A. Sweeney). 121

CONTENTS (cont)

Page

Blast Overpressure (D. L. Cook) 122
Energy Transport Through the Combustion Chamber Gas (D. L. Cook). 123
Reactor Chamber Sizing (D. L. Cook, M. A. Sweeney). 123

ECONOMIC CONSIDERATION 124

Minimum "Economic" Pellet Gain and Yield (D. L. Cook) 124
Effect of Driver Replacement Costs (D. L. Cook, K. R. Prestwich). 125
Parametric Analysis of Power Reactor System Costs (M. Daniels). 125

SPECIFIC REACTOR (POINT) DESIGNS (D. L. Cook). 126

Hybrid Reactor Design Studies 126
Compact Pure-Fusion Reactors. 126
Summary 127

LOW-CURRENT DENSITY DIODE PHYSICS STUDIES. 127

Overview (K. R. Prestwich). 127
Needle Cathode Instabilities (M. T. Buttram). 128
Emission Enhancement (R. S. Clark). 130
Emission Suppression (R. S. Clark). 132

PLASMA INJECTED, MICROSECOND, E-BEAM DIODES. 133

Vacuum Surface Flashover Tests (J. J. Ramirez). 133
Preliminary Tests Using Surface Flashover Plasma Cathode (J. J. Ramirez). 136
Tests with Independently Driven Surface Flashover Plasma Source (J. J. Ramirez) . 137
Tests Using Plasma Guns (D. L. Cook). 139
Summary and Conclsuions (J. J. Ramirez, D. L. Cook) 144

REFERENCES 145

PUBLICATIONS. 147

PRESENTATIONS 149

TECHNICAL OVERVIEW

Our experimental results on pulsed power generation and vacuum electromagnetic energy transport indicated that the basis for producing a 1 MJ output on EBFA has been confirmed. Our theoretical understanding of the magnetically insulated transmission line (MITL) has improved considerably and an improved theoretical design tool is now available. The accelerator itself and the new facility are progressing on schedule and we have begun the necessary long lead steps to prepare for the upgrade of EBFA to be carried out after the first two years of operation. We have made progress in reliably producing focused electron beams at current densities in excess of 10^7 A/cm^2 and are prepared for more definitive deposition physics experiments and the start of multiple beam studies. Our studies of ion beam diodes have been extended to a new and efficient approach which was demonstrated on Proto I and theoretically modeled using numerical techniques. Both electron and ion beams are of continuing interest as drivers of magnetically insulated targets and improved designs are emphasizing higher gains at the relatively low beam power densities which are presently envisioned. The emphasis of our systems studies was changed from that of economics to a preliminary consideration of a specific reactor concept. We investigated the requirements for a compact, modular, gas-filled reactor "combustion chamber" which appears to be economically compatible with our low cost and efficient technology. If we succeed with production of moderate pellet gains (~ 30) with reliable high average power versions of our present devices, it may be possible to produce a relatively inexpensive demonstration power reactor as a first step on the road to a practical power reactor. The requisite repetitive pulse switches and power conditioning components needed for such an experiment are still in their infancy but initial results indicate that flowing gas spark gap switches will satisfy our requirements.

The key technical milestones achieved during this reporting period are summarized below:

1. The principle of efficient energy transport at high power densities in magnetically insulated transmission lines was demonstrated.

2. The EBFA prototype pulse forming lines and their output switches were demonstrated at a level which extrapolates to an EBFA output of 1 MJ.

3. A conceptual design study of a 1981-1983 upgrade of EBFA to the 2 MJ level was completed and a request was made to the Office of Laser Fusion for FY'79-FY'80 plant engineering and design funds.

4. Magnetic target design studies were extended to include cryogenic DT fuel predicting relatively high gains (> 50) at low power levels (≈ 50 TW).

5. Electron beam diode optimization on Proto I (with particular emphasis on prepulse reduction) has permitted us to increase the available current density for thin foil experiments from the 5 to 10 MA/cm^2 range to the 14 to 17 MA/cm^2 range.

6. A magnetically insulated ion diode was tested for the first time on Proto I demonstrating 80 percent ion production efficiency and ion focusing to > 30 kA/cm^2.

7. A study of a multiple stage ion acceleration concept (Pulselac), which is based on the principle of interstage beam space charge neutralization, was initiated.

8. Numerical models of preheated magnetically insulated targets were tested verifying the assumed initial conditions for previous neutron producing experiments.

9. A short pulse (3 ns) DT neutron source has been developed and used to compare measured defector response with a neutron transport code.

10. A continuous run of over 10^6 shots was carried out on the high average power test facility (RTF-1) yielding data which indicates reliable and long life output switch behavior (estimated lifetime > 10^9 shots).

11. An initial conceptual design study for a gas-filled particle beam fusion reactor combustion chamber was begun indicating that

chamber sizing could be predicated on a blast over pressure and that the radius could be < 3 m for a 100 MW_e pure fusion design and < 1.5 m for a hybrid design.

On April 1, 1978, 72 people were assigned to the Particle Beam Fusion Program with an FY'78 operating budget level of $8.7 M.

PULSED POWER RESEARCH

OVERVIEW

Important data showing the transport of electrical power in the terawatt range over 6.5 meters with a power transport efficiency of 100 percent and an energy transport efficiency of 90 percent were obtained. These results were required for EBFA and demonstrated the feasibility of the vacuum interface, magnetically insulated line, and diode concept. The results exceeded expectations and provided a 2 ns rise from zero to peak of a .4 MA current. Magnetically insulated power flow densities exceeding 10^{11} W/cm^2 were achieved over shorter distances. These results indicate that a much smaller beam drift distance to the pellet could be possible. Although about 50 percent of the electron current flows external to the conductor boundary during the 6.5 meter transport, all of the current was recaptured and most was focused to a few mm spot during these experiments.

The MITE (EBFA prototype) continues to function well with a new set of stacked lines simultaneously switching into a common transmission line. The vacuum interface is operating well. The first duplicate of an EBFA module will be constructed by using the similar Marx generator, lines, switches, interfaces and vacuum lines. The same drawings will be used to order the EBFA modules. This device constructed as a modification of Hydra (Hydra Mite) will provide a valuable EBFA proof test while providing a needed research tool for beam focusing, transport, and concentration. Many of the EBFA details have been resolved during this period by providing the new accelerator.

Figure 1 shows the present EBFA design. The main changes are in the location of the water energy storage capacitors, the pulse forming line configuration and the magnetically insulated transport lines. These changes are based on solid dielectric capacitor data and the new line stacking techniques.

Table I shows the present EBFA performance analysis. It is based on the MITE data, Proto II tests, the Hydra Marx tests and computer runs on the projected water capacitors. For

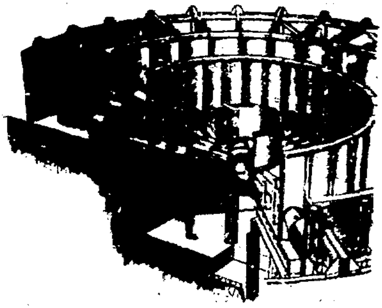

Fig. 1. EBFA I

TABLE I

EBFA I Performance Analysis

Single Module - Present Operating Point

Marx Generator	3.0 MV, 98 kJ
Intermediate Store	2.5 MV, 65 kJ
Pulse Line	2.4 MV, 46 kJ
Vacuum Insulator	2.0 MV, 32 kJ
MITL	1.9 MV, 30 kJ
Diode	1.9 MV, 4 TW

Projected 36 Module EBFA I

	Minimum	Medium	Maximum	Present
Marx Generator				
MJ	2.9	3.5	4.[illegible]	3.[illegible]
MV	2.2	2.9	3.2	3.0
Intermediate Store				
MJ	1.7	[illegible]	2.5	2.3
MV	1.8	2.4	2.8	2.5
Pulse Line				
MJ	.7	1.5	1.8	1.[illegible]
MV	1.8	2.3	2.55	2.4
ns	50	50	50	45
Vacuum Insulator				
MJ	.83	1.0	1.[illegible]	1.1
MV	1.5	1.9	2.1	2.0
ns	50	50	50	45
MITL				
MJ	.59	.97	1.2	1.08
MV	1.4	1.8	2.0	1.9
ns	50	50	50	45
Diode				
TW	14	24	[illegible]	25
ns	45	45	45	45

reference the present operating point of MITE is given and then the projection to a 36 module EBFA I is done. The minimum output projections are based on 70 kV charge on the Marx generator. The medium projection curve on a 90 kV charge and the maximum is 100 kV charge voltage. The present operating point on MITE is 95 kV Marx charge.

Proto II continues to function well and was used on power concentration magnetic insulation experiments reported elsewhere with good results. A new prepulse isolation scheme was proposed and tested and initial parameter studies were completed to reverse the output pulse polarity.

MITE-SELF-MAGNETICALLY INSULATED VACUUM TRANSMISSION LINE EXPERIMENT

Introduction

High current relativistic particle beam accelerators for inertial confinement fusion require the transport of power from the pulse forming lines located at 9 meters from the pellet and delivering ~0.05 GW/cm^2 to the A-K gap, located at 0.5 meters and delivering power at >100 GW/cm^2. We have shown that this power transport and spatial power compression can be done with the MITE combination of 2 meter long water dielectric transmission line, vacuum insulator, and 6.5 meter long self-magnetically insulated, vacuum triplate line.

The long, self-magnetically insulated vacuum transmission line experiment MITE was assembled and tested at full power. Initially only 60 percent of the energy was transported to a calorimeter 6 meters from the diode. The losses were caused by an apparent instability in the electron flow and by an azimuthal asymmetry in the magnetic field at the input to the line. The injection geometry was changed to prevent these losses and 90 percent energy transport at ~100 percent power transport were achieved. The power and energy requirements for one module of EBFA were exceeded by modest amounts. The average power density in the seven meter long line was 1.6 x 10^{10} W/cm^2. Pinch experiments with a modified parapotential cathode produced a well centered hole all the way through a 1.27 cm thick aluminum anode. High electric field stress experiments in the A-K feed were conducted with a 0.34 cm gap between the inner and outer coaxial conductors of a Z_0 = 7.6 Ω feed. The A-K gap shorted after 20 ns under these conditions but the high stressed feed showed no signs of breakdown at this 6 MV/cm level with an average power density of 1.3 x 10^{11} W/cm^2. Higher stress experiments require the development of small cathodes that can avoid shorting while operating at ~4.5 Ω and 0.8 TW.

Apparatus

The schematic diagram of the experiment is shown in Fig. 2. The power flow successively through the vacuum insulator, the vacuum feed region, the 6 meter long self-magnetically insulated triplate transmission line, a tapered transition section, a coaxial A-K feed, and finally to the output through a focused flow diode. The cross sections of the experiment at various points are shown and the area through which power flows are shown as shaded regions. Both the inner and outer lines are sprayed with carbon to facilitate electron emission. The monitors for measuring (a) total current (I_o, I_{T1}, I_{T2}, and T_{T3}), (b) boundary

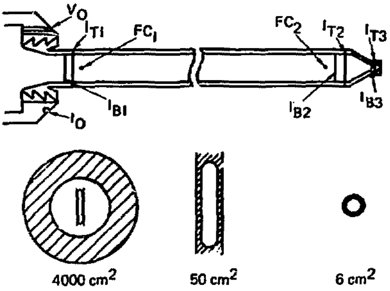

Fig. 2. Schematic diagram of the experiment. The cross-sectional areas through which power flows at the vacuum insulator, triplate line, and A-K feed are shown.

current flowing in the inner conductor (I_{B1}, I_{B2}, and I_{B3}), (c) diode voltage (V_o), and (d) the electron loss current density of the electron flow to the wall (FC1, FC2) are also shown. In addition, the line can be broken at several locations to accommodate a Child-Langmuir space charge limited diode. The C-L diode has a total stopping carbon calorimeter to measure total energy transport and a magnetic spectrometer to measure the time integrated energy spectrum of the electrons crossing the A-K gap. X-ray pinhole cameras view the lines and the anode. The time history of the x-ray dose and the time integrated polar diagram are recorded at the output with a collimated PIN diode and a collimated TLD array.

The data is recorded on a combination of Tektronix 7912 transient digitizers and fast oscilloscopes. The 7912 system allows the data to be reduced and compared to theory quickly. Typical current, corrected voltage, impedance and power waveforms at the input to the transmission line are shown in Fig. 3. The total energy input is typically 32 kJ.

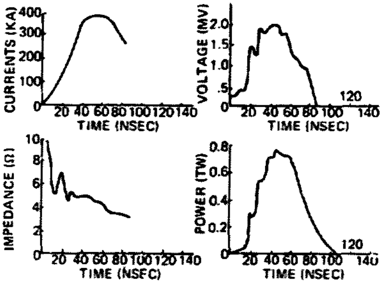

Fig. 3. Typical data at the input to the MITE triplate line is shown.

Power and Energy Transport Experiments

The MITE triplate experiment was conducted in the negative polarity mode. The input current and output current traces are shown with the loss current density data in Fig. 4. The load is the unpinched C-L diode with the calorimeter and magnetic spectrometer on the anode. In this mode, the line is terminated in its matched, self-limited impedance. The peak current transport efficiency is 70 percent and the total energy transport efficiency is 60 percent. However,

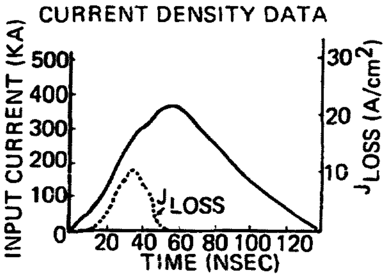

INPUT

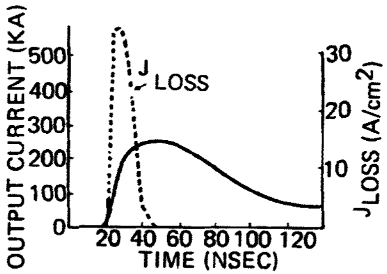

OUTPUT

Fig. 4. Transported total currents and the loss current densities measured at the input and output of the MITE triplate line are shown.

the loss current occurs only during the rising portion of the pulse at the beginning and end of the line, so a continuous, uniform loss can not be used to explain the inefficient transport.

In order to locate the loss, calorimeter data was taken at 0.4 meters, 1.4 meters, and 6 meters from the injection points by using different lengths of inner conductor line. The data is summarized in Fig. 5. X-ray pinhole photographs of the diode showed a well-defined loss at the injection region as shown in Fig. 5. Well-defined striations along the full width of the inner (negative) triplate line were observed with an axial extent of approximately a centimeter. They occurred at the following positions in centimeters from the beginning of the 1 cm spacing in the transmission line: 53 ± 1.5, 86 ± 2, 92 ± 1, 95 ± 1, cm, 99 ± 1, 102.5 ± 1, 107 ± 0.5, 111 ± 1, 116 ± 1, and 121 ± 1.

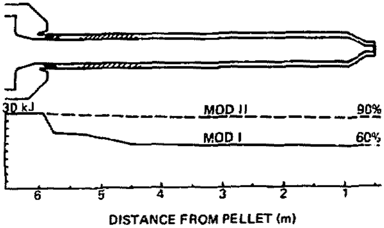

Fig. 5. Calorimeter measurements of energy transport are shown as a function of distance from the beginning of the line.

A photochromic film pack behind a 7 mg/cm^2 Al filter at one of these sites showed that the damage was caused by either >85 keV electrons or >1.5 MeV ions. There was no voltage reversal in these experiments because the load was well matched, and the insulator flashed soon after the main pulse was over.

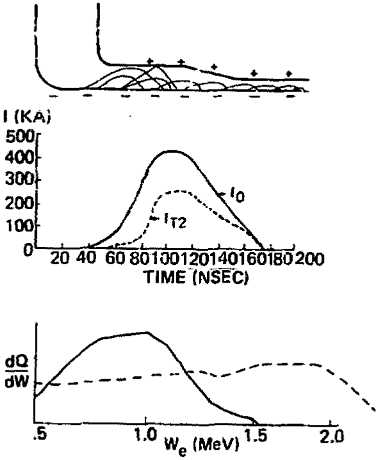

Fig. 6 Schematic diagram of the first injection geometry and the corresponding current transport and time integrated electron energy distribution.

The diode current, input current and output current are shown in Fig. 6. The data shows a loss in the diode injection as well as one in the main line. In Fig. 6, the time integrated electron energy distribution at the output is compared to the input spectrum calculated from the diode and voltage monitors on a later shot, number 110, which showed no losses. The comparison is thus one between the output and a good input. The voltage is reduced by a substantial fraction. The peak corrected voltage and the impedance at peak power were 1.95 ± 0.15 MV and 4.2 ± 0.2 Ω respectively for this series of shots.

The data is indicative of two losses. One in the diode before the I_{T1} monitor, and a second between 0.4 m and 1.4 m. The second loss is consistent with an instability that has a spatial growth length of 0.53 m in the lab frame and has average electric fields of at least 85 kV/cm or ~5 percent of the mean field in the line. The instability lost 11 ± 1 kJ or ~30 percent energy loss and caused a substantial (~25 percent) degradation in the peak voltage. Some of these characteristics suggest a dichotron[1] instability. However, the theory for this particular case has not been investigated, so the nature of the instability has not yet been determined. The localization of the loss near the input suggests that the instability and its losses may be caused by the perturbation of the electron flow in the injection region. The geometry of the injection region is also shown in Fig. 6.

To test this hypothesis, the injection geometry was altered to that shown in Fig. 7. Essentially, the 1 cm spacing was continued all the way to the beginning of the line. The current and electron energy data are also shown in Fig. 7. The current transport through the line indicates the instability was controlled by reducing the perturbation in the line geometry. However, the current lost before the input current monitor has increased. The energy transport was 18 ± 1.1 kJ or 56 percent of the total energy passing through the vacuum insulator and 73 percent of the energy injected into the line. The peak voltage at the output was 76 percent of the peak corrected volts and the input impedance was 3.7 Ω. The outer conductor was damaged at the middle of the line in the first 15 cm. The loss was confirmed by pinhole photography of the injection region and occurred at the position shown in Fig. 7.

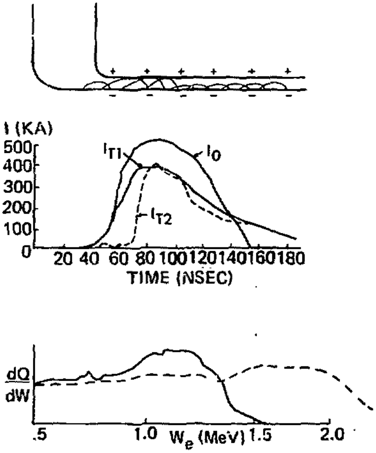

Fig. 7. The results of the tests with the second injection geometry are summarized.

The magnetic field distribution in the line at the injection region was measured with a movable $\dot{B}$ probe at low voltage levels and is shown in Fig. 8. The field distribution 30 cm further downstream is shown for comparison. The loss occurred where the magnetic field was 20 percent below that in the main line. This magnetic field is insufficient to trap the electrons. Since the top and bottom of the triplate are closer to the vacuum insulator, the effective inductance for current flowing to the top and bottom is less than that for current flowing to the middle. The current bunching at the top and bottom then causes the reduced magnetic field in the middle.

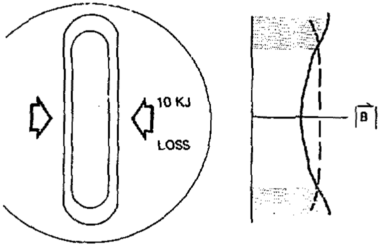

Fig. 8. The distribution of magnetic field between the transmission line gap at the injection region (solid line) and 30 cm into the line (dotted line) are shown opposite the line profile.

This azimuthal asymmetry of the magnetic field was then corrected by using a flux shaper to equalize the inductance for every current path. A uniform B field distribution to within 4.0 percent at low voltage was obtained. The geometry and the transport data are shown in Fig. 9. The diode losses were decreased, and the energy transport was improved to 85 ± 3 percent. The voltage transport was also improved. However, the flux shaper decreased the feed region gap from 5.4 cm to 1.27 cm at its closest separation. The feed consequently emitted electrons and the electron flow had a perturbation as shown in Fig. 9. The striations were again present but were 15 cm further upstream. Since the perturbation had been moved 15 cm, the first striation was again 53 cm downstream from the perturbation even though the energy transport was much better. The line impedance at injection was 4.6 ± 0.4 Ω which was consistent with very little losses in parallel with the line at injection.

Another approach to the injection problem is shown in Fig. 10. The electric field was relieved at the injector where the magnetic field is non-uniform. The transition section is extended from the original 4 cm to 15 cm. The transport was excellent, as shown in Fig. 10. The currents and the electron energy distributions at the input and the output agree. The energy transport efficiency is 90 ± 4 percent and the power transport efficiency is ~100 percent within experimental error of ~10 percent. Consequently, by shaping the magnetic field distribution at injection, one avoids the losses near the injector and by making the transition in electron flow very gentle the instability losses can be avoided.

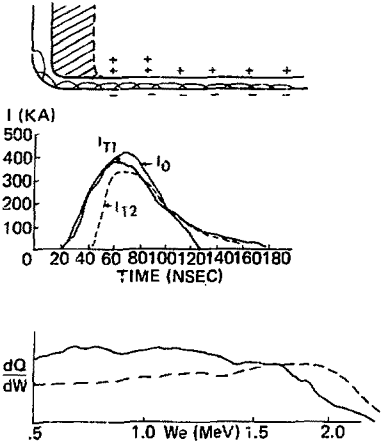

Fig. 9. Summary of data acquired with the third injection geometry which employed a flux shaper to improve the magnetic field uniformity at the injection point.

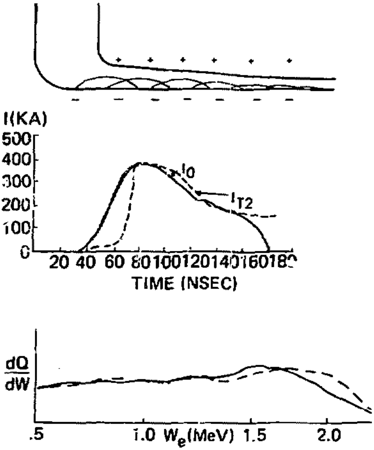

Fig. 10. Summary of data acquired with the fourth injection geometry.

It is possible that the losses observed in the negative polarity coax experiment at Physics International[2] (PI) before the input monitor were caused by removing parts of the input ground feed. The alteration was done to accommodate an input voltage monitor after the positive polarity experiments were completed. The alternation perturbed the symmetry of the current flow to the coax, reduced the B field on one side, and led to a loss. The instability loss may explain the observed polarity effect in the PI experiments. The difference between the PI positive and negative polarity is the severity of the perturbation in electron flow as shown in Fig. 11. If this hypothesis is true, the growth length of the instability must be ~300 cm at input parameters of 148 kA, 1.9 MV, and gap spacings of 1.95 cm. The reduction of growth length with increased power or decreased gap spacings suggests that this loss mechanism could be important in convoluting many magnetically insulated lines together.

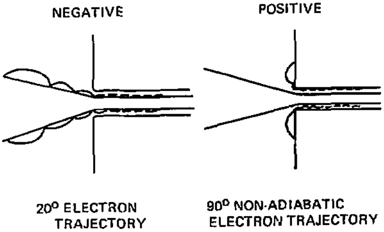

Fig. 11. The severity of the change in the electron flow as it enters the vacuum transmission lines is illustrated for positive and negative geometries.

Comparison with Theory

The measured vacuum impedance of the MITE triplate at low voltage was $Z_0 = 7.6\ \Omega$. The 1-D analytical theories of parapotential flow[3] and steady state flow[4,5] predict a functional relation $F(I_T, I_B, V_0) = 0$ among the total current I_T, the boundary current I_B (which equals the total current minus the electron current), and the voltage across the gap for a given line geometry. The theories give similar results for the non-saturated flow cases,[6] i.e., when the boundary current is sufficiently large to keep the electron flow well away from the wall. The results of experiments with short and long lines show that the flow is unsaturated for voltage V > 1 MV.[1,7,8] Since the parapotential formulation is easy to manipulate and the others give very similar results, we have chosen to compare the experiments to the parapotential theory.

The parapotential formulation can be reduced to

$$I_T = I_T(\gamma_o, \gamma_m) = \frac{0.51E6}{Z_o}\gamma_m$$

$$\left[\ln(\gamma_m^2 - 1)^{1/2}) + \frac{\gamma_o - \gamma_m}{(\gamma_m^2 - 1)^{1/2}}\right]$$

$$\gamma_m = I_T/I_B$$

$$\gamma_o = \frac{V_o}{.511E6} + 1$$

for a line with a vacuum impedance Z_o and V_o volts applied across it. The waveforms for I_T and I_B at the input and at the output are shown in Fig. 12. The measurements were made with self-integrating Rogowskii coils with the output waveforms time shifted - 17 ns to compensate for the light transit time between the two monitor locations. The erosion and sharpening of the pulse front are evident and predicted by a semiemperical circuit code[9] and a full two-dimensional, time dependent, PIC, electromagnetic code.[10] The input boundary current follows the total current until the electron emission becomes important at E ≃ 450 kV/cm and 10 ns after the pulse begins. The boundary current then oscillates for approximately 13 ns and settles down at (55 ± 4) percent of the total current. The amplitude of the boundary current excursion is reduced by ~50 percent by coating the inner line with graphite. There is no similar excursion on the output currents, because the voltage percursor moving down the line ahead of the main pulse must turn on electron emission from the cathode. The velocity

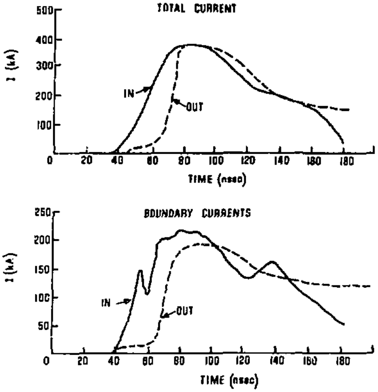

Fig. 12. Total and boundary currents are given at the input (solid lines) and output (dashed lines) of the magnetically insulated line.

of the pulse at 67 percent of V_{max} was $(.71 \pm .05)c$. The line impedance, I_T, I_B, and front velocity are in excellent agreement with the code[10] results.

The actual and computed total input currents are shown in Fig. 13. The points A and B refer to the beginning of significant electron emission and the stabilization of the boundary current, respectively. Before the flow settles down, the agreement is poor. After it settles down, the agreement is excellent.

Since a voltage monitor that can operate at 2 to 6 MV/cm stresses with electron flow in the gap has not been developed, we can not run a similar comparison at the output. However, the analysis can be inverted to give V as

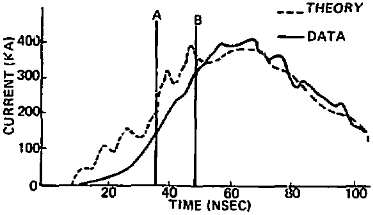

Fig. 13. The measured input current (solid line) is compared with the unsaturated parapotential theory $I_p(\gamma_m, \gamma_o)$ at the line input.

$$V_{out} = 0.511E6\,(\gamma_{out} - 1)$$

$$\gamma_{out} = \gamma_m + \frac{I_T Z_o}{0.511E6}\left(1 - \frac{1}{\gamma_m^2}\right) - (\gamma_m^2 - 1)^{\frac{1}{2}} \ln(\gamma_m + (\gamma_m^2 - 1)^{\frac{1}{2}}),$$

and the results are shown in Fig. 14. The agreement with the input voltage is appropriate for ~100 ± 10 percent transport. The impedance $Z = V/I_T$ and power $P = I_T V$ are in excellent agreement with the input impedance and power. The time integrated power agrees with the output energy to within 10 percent. The pinched beam had an impedance Z_{load} greater than the matched load impedance Z_m. The current not absorbed in the load was dissipated to the sides of the feed. Consequently, the line ran at its self-limited value Z_m, as indicated by this analysis. This analysis is also appropriate for a short circuit but we have not demonstrated that it is adequate to describe the intermediate loads Z_L with $0 < Z_L < Z_{matched}$.

Conical Transition to the A-K Feed

The transition from the triplate cross section to a coaxial feed to the A-K gap is a short tapered line like those shown schematically in Fig. 15. Since the higher angled tapers give a shorter

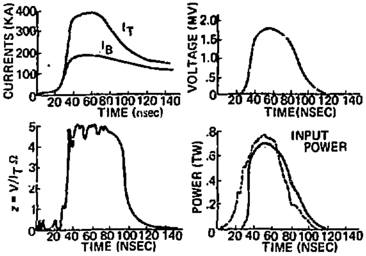

Fig. 14. Output waveforms based on I_T and I_B and the parapotential theory.

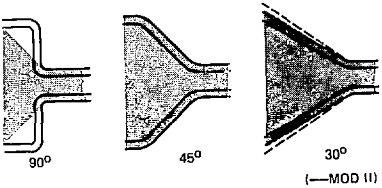

Fig. 15. Schematic diagrams of various tapered feeds that were investigated.

transition region, they present less inductance to the power flow. However, if the taper is too abrupt, current flows near the center of the line into the coaxial feed. The B field at the edges is consequently relieved and magnetic insulation is lost. The values of $|E|$ and $|B|$ were measured with $\dot{D}$ and $\dot{B}$ probes when low voltage pulses were applied to these tapered lines. Shaded regions in Fig. 15 correspond to areas in which the ratio of $|E|/|B|$ in the gap between the lines was less than or equal to $|E|/|B|$ in the triplate line. As a result of these tests, only the 45° and 30° tapers were built. The 30° tapers was installed and some damage was found on the top and bottom of the outer conductor at the beginning of the transition. The gap between conductors was enlarged to from 1 cm to 2 cm at these points, as shown in Fig. 15 as Mod II. No additional damage was observed after the modification.

High Stress A-K Feed Experiments

A liner was placed in the A-K feed to reduce the gap between the inner and outer conductor to 0.36 cm. This lowered the vacuum impedance of the line to $Z_o = 7.6\ \Omega$, which is the same as that of the triplate line. The cathode should, therefore, be stressed to a vacuum field of 6 MV/cm at 2 MV. The boundary currents in the A-K feed and in the triplate line at the taper were equal, which indicated the high stress coax functioned very well in the self-limited mode. Approximately half the current was in electron flow, which was consistent with the unsaturated flow models. The anode electric field was calculated to be ~11 MV/cm and the average power density in the feed was 130 GW/cm^2.

After 20 to 30 ns, the A-K gap shorted. Aluminum debris was consistently sprayed into the A-K feed on the south side. However, there was no electron damage in the feed and the x-ray pinhole photographs of the feed did not show any significant emission. The early shorting of the gap was tentatively attributed to the following:

a. The prepulse of 6 kV causes early shorting when the electric field during the prepulse exceeded 20 kV/cm. The E fields in the A-K feed and A-K gap were 17 kV/cm and 20 kV/cm, respectively. Additional increases in the power density achievable requires the suppression of prepulse.

b. The anode damage indicated that the beam was never well pinched. This could have been caused by plasma formation during the prepulse or by failure of the A-K structure to trap and focus the electrons flowing out of the coaxial feed.

c. The center conductor was later found to move horizontally (0.179 ± 0.03 cm) to the south and vertically 0.010 cm upward when the line is evacuated. This was not a problem with a one centimeter line spacing but certainly could have been a problem in the high stress experiment. The movement explains the predominance of debris on the south side of the coax. The retractable support will be installed to keep the line centered for high stress experiments.

Pinched Beam Studies

Various cathodes have been used to pinch the beam and many have been successful. Approximately 15 mm diameter holes through 12.7 mm thick aluminum anodes have been reliably produced from 5.4 cm and 3.8 cm diameter cathodes. These studies are just beginning so it is premature to quote peak power densities or pinch efficiencies. The research on pinching is directed towards producing (a) the minimum diameter cathode that operates at ~4.5 Ω for the full power pulse, and (b) the maximum power density in the pinch with the minimum diameter cathode.

EBFA

Pulse Forming Lines and Switches

Flat plat pulse forming lines were constructed from the MITE Blumlein transmission lines and tested to 2.4 MV. Figure 16 is a diagram of the lines. The two parallel 2.2 Ω pulse forming lines have a capacity of 16 nF and store 46 kJ at 2.4 MV. Two sets of five prepulse suppression switches transfer the stored energy to the vacuum interface along the transition section. These self breakdown water switches allow two or more pulse forming lines to be easily paralleled by mixing the electromagnetic waves from each pulse forming line. Tests, where one set of switches was removed, showed that equal waves on each side of the transition section were produced from only one of the pulse forming lines. The reduced capacitve coupling across these switches gives a measured prepulse of only 7 kV, .3 percent of the pulse forming line charge voltage. To further reduce the prepulse level, a set of prepulse suppression switches located at position A (Fig. 16) will be incorporated in the EBFA design and will be installed and tested on MITE.

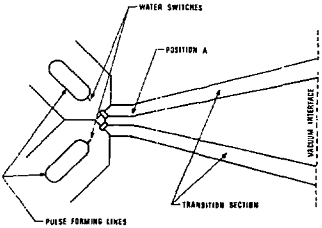

Fig. 16. EBFA pulse forming section.

Figure 17a shows a 2.3 MV charging waveform on the pulse forming lines. The transfer time from the intermediate store to the lines is 270 ns. Figure 17b is the voltage waveform at the input to the transition section. The apparent voltage increase of the 45 ns FWHM pulse is due to the proximity of the voltage monitor to the switches and the nonplaner wave that exists in this region.

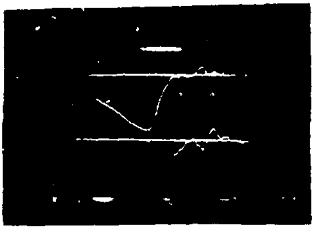

Fig. 17. a. Pulse forming line charging voltage .74 MV/div, 50 ns/div.
b. Pulse forming line output voltage .63 MV/div, 50 ns/div.

Trigatron Switches

Locating the intermediate storage capacitor in the water section of EBFA required locating the gas insulated trigatron switch in the same water section. The new switch location provides a lower inductance. The result is a faster line one charge time or alternatively the capability of producing a longer pulse into the diode thereby providing greater EBFA flexibility. In general, the reliability of gas switches in water is less than in oil due to trapped air bubbles along the insulator. Streamers can close late in time and have enough energy to fracture the pressure housing. The problem is alleviated by alternating insulator sections with metal grading rings and making the switch insulator stack longer. The EBFA switch is the same as used in Proto II but with the insulator length increased from 12 to 17 inches. Connections to the switch will be such that the switch may be removed without draining the water tank. By doing this the lengthy process of removing bubbles from the underside of all switches after maintenance of one is eliminated and provision is made for preventive maintenance during an experimental program to obtain accelerator module synchronization.

Marx Generator Test Results

The EBFA Marx generator which resulted from a mechanically redesigned Proto II Marx has been tested. The redesign was done to lower the EBFA procurement costs. The resultant Marx was installed and tested in the Hydra tank to provide an upgraded Marx for Hydra. The tests showed that the redesigned Marx performed similar to the Proto II Marxes and will be acceptable for EBFA I. In addition to this verification, two new Marx erection phenomena were identified and traced to their causes. A memo is being written to explain the phenomena in more detail and will be published later.

One explained phenomena was causing the high frequency prepulse signature of Hydra. The prepulse was lowered from 15 kV to about 8 kV on Hydra during the study. The other phenomena is causing up to 0.15 energy transfer loss by an interaction between the Marx, stray capacities, and the Hydra line. A modification consisting of triggering the Marx in the center will provide less prepulse and better efficiency. The modification could be incorporated on EBFA II.

Intermediate Storage Capacitor

Since the reliability of solid dielectric capacitors were found too low for use in EBFA, a water insulated 19.5 nF intermediate storage capacitor has been designed. The EBFA design will be an open unit in the water section of the tank and use the same deionized water as the pulse forming lines as opposed to separate capacitors in the oil section of Proto II. A benefit of locating the capacitor in the water section is that the oil/water feed thru barrier also serves as the capacitor insulator feedthrough and thus reduces the number of insulators. In addition the problem of gas generation and leakage is reduced. The 45 inch diameter inner capacitor electrode is cantilevered from the insulator and the 60 inch diameter outer electrode is mounted to the water tank wall which provides a low inductance feed from the oil section to the water capacitor.

A unit cell approach based on equipotentials generated by the JASON code was used to calculate a total storage capacity for the assembled water capacitor of 21.4 nF which includes the fringing fields. Figure 18 is a plot of the electric field strength parallel to the insulator surface along the water side of the barrier. Peak fields are within 10 percent of those on the Proto II capacitors. Mean field strengths on the inner and outer electrode surfaces are 183 kV/cm and 137 kV/cm respectively for a 3 MV charge on the capacitor. These field strengths are 7 and 27 percent reduced from those on the Proto II water capacitors.

Gas Pressure Transducer Readouts

A remote gas pressure measuring system was designed, built and tested on Proto II and MITE. The system employs a commercially available pressure transducer, a small amount of circuitry and a digital voltmeter readout. The system is calibrated to read pressure directly in psig. The testing on Proto II and MITE has shown the system to be insensitive to the EMR produced by those machines. The design has been turned over to the Control/Monitor System engineers to be incorporated in the EBFA control system.

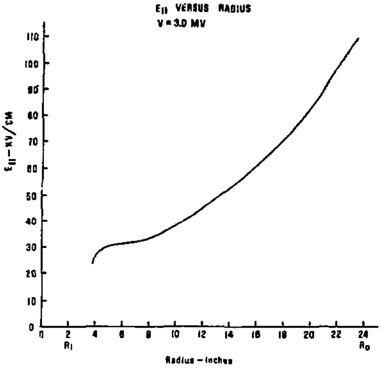

Fig. 18. Electric field strength on water/oil interface vs. radius.

Proto II – Reverse Polarity and Prepulse Level

A requirement for lower prepulse and a negative high voltage output for the multiple electron beam experiment resulted in a study to determine the reverse polarity operation of Proto II and the effectiveness of the prepulse reducing ground planes described in the last progress report. The results show that a decrease of prepulse from 40 kV to less than 10 kV should be obtained on Proto II.

A single Proto II line was isolated in the Proto II water tank and a series of experiments were performed with and without the ground planes in position for various spacings of switch one and switch two. A small pulser unit provided input pulses and the feedthrough voltage (prepulse) was measured. Static system capacities were thus determined at low voltages. A set of prototype ground planes were fabricated; the Marx generator polarity was reversed; the water capacitors were reversed and a series of tests at full negative polarity voltage were performed to check plate spacings, breakdown levels and water switching gaps. The ground planes also act as line crowbar switches and isolate the load from the water capacitors. They breakdown at longer time scales but will also break during the main voltage pulse if the voltage is too high. The ground plane spacing is thus a compromise between crowbar effectiveness and the range of operating voltages anticipated. The spacing chosen will allow operation at the previous output levels.

The prepulse comes from at least two parts. *First, is the capacitive coupling* between lines. This coupling is greatly decreased by the ground shield installation. The second contribution comes from the dc/dt term as the switching arc streamers close the gap rather late in the switching process. The shields are less effective for the dc/dt term. The shields than change the prepulse amplitude along with the duration. Preliminary results indicate that 1/3 of the voltage comes from the dc/dt term with the remainder from the capacitive coupling. In summation, the prepulse level on Proto II should be less than 10 kJ after the shields are installed.

2-Ω Calibration Pulser

A method to decrease the time for monitor calibration on EBFA and Proto II has been proposed. Monitors will be standardized, than calibrated on a separate pulser, and then placed in the accelerator. To accomplish the calibration a 2 Ω pulser has been built that generates a 4 kV, 40 ns pulse across 2 Ω loads with less than 1 ns risetime capable of calibrating the monitors. A 2 Ω Mylar stripline is pulse charged in 150 ns to 8 kV and then switched through a 10 mil spark gap insulated with FC 77 Freon liquid and Kapton onto sixteen, 31 Ω detonator type cables which distribute the pulse to the machine and monitors being calibrated. The Freon-Kapton gap closes with 10 or more channels which results in a subnanosecond pulse risetime. Ways of using this and similar pulsers and calibration fixtures which duplicate local field configurations at various monitor locations in the EBFA are being investigated as a means of reducing the time needed for monitor calibration and could eliminate most in-situ calibration procedures.

Magnetic Flashover Inhibition Using an Externally Applied Magnetic Field

The goal of these experiments is to determine the effects of magnetic fields on the process of vacuum insulator surface flashover. Past experiments have indicated that surface flashover phenomena is caused by a secondary electron avalanche for electric field insulator angles from -60 to +30 degrees. Theoretical studies indicate that a magnetic field could arrest this avalanche process and hopefully prevent vacuum surface flashover.[11,12]

The experiment consists of a two ohm coaxial pulse forming line that applies a radial electric field to a plexiglass diaphram insulator coated with DC704 pump oil. A parallel capacitor bank is then used to generate a theta magnetic field on the diaphram. The magnitude and polarity of these fields can now be varied independently. The experimental arrangement and diagnostics have been described in detail in earilier reports.[13,14]

Tests are completed on the 15 degree insulator for both positive and negative polarity electric fields. When the magnetic field was in the direction drift cause electron into the insulator surface, breakdown occurred immediately. For the data included, the magnetic field caused electron ExB drift away from the insulator surface. Figure 19 is a plot of the insulator disk equipotentials for one megavolt applied potential, Fig. 20 plots the value of E_{11} and the angle between the electric field and the insulator surface. The value of E_{11} to the insulator surface is the improtant parameter in the theory of magnetic flashover inhibition (MFI). The experimental data is analyzed by plotting the time to breakdown vs. E_{11}/cB (in MKS units). The anode electric and magnetic fields were used for the plot shown in Fig. 21a. This data suggests that the critical value of E_{11}/cB is a function of voltage polarity. Figure 21b is a replot of 21a but uses the cathode electric and magnetic fields. With this data interpretation, there is no polarity effect and the magnetic field effect takes place at a value of $E_{11}/cB = .07$.

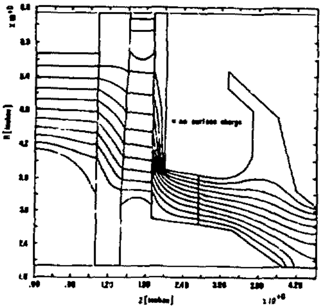

Fig. 19. Equipotential plots in MFI diode.

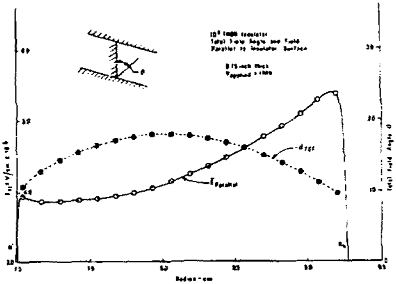

Fig. 20. E parallel and angle of total electric field alone insulator surface.

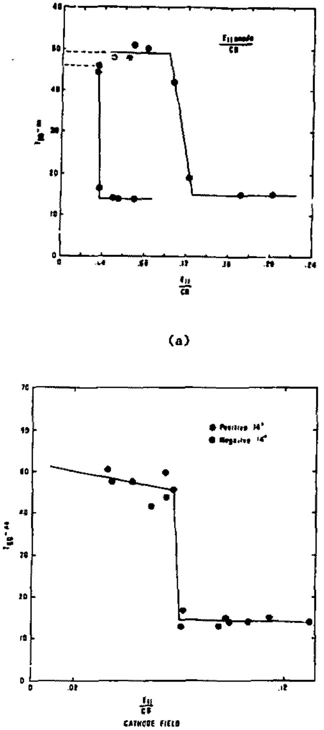

(a)

(b)

Fig. 21. a. Time to breakdown vs. E_{11}/cB using unknown values for the electric and anode field.
b. Time to breakdwon vs. E_{11}/cB using unknown values for the electric and cathode field.

Magnetic inhibition theory of vacuum surface flashover shows that $E_{11}/cB = 1.233\ E_1/E_0$. E_1 (in eV) is the energy on the secondary electron emission curves at which the yield first exceeds one and E_0 (in eV) is the mean energy of the emitted secondary electrons. Measurements of E_1 for DC704 and DC705 pump oil were made but the E_0 measurement is difficult and has not been made.[15] E_0 probably ranges between .5 and 2 electron volts and E_1 between 10 and 50 electron volts. Figure 22 is a plot of E_{11}/cB vs. E_1 for various values of E_0. The shaded area between the curves is the range of uncertainty for the values of E_0 and E_1. One must be at a value of E_{11}/cB at some point within this range to utilize magnetic inhibition. The horizonal line is the value of E_{11}/cB at which the experiment shows the onset of magnetic insulation.

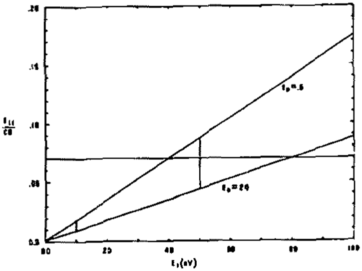

Fig. 22. Plot of E_{11}/cB as a function of material properties for S.E.E. required for magnetic fusion insulation.

These experiments show that the maximum electric field on a vacuum insulator surface can be increased by a properly oriented magnetic field for electric field to insulator angles between −45 to +20 degrees. The data shows that the cathode values for the electric and magnetic fields are the important parameters. The cathode field dependence is consistent with stopping the electron avalanche at the source of electron supply to prevent plasma formation on the insulator surface. These results are consistent with the theory of secondary electron avalanche being the controlling factor. Experiments at a +45 degree angle between the electric field and the insulator indicates no improvement with magnetic field.[13] These facts and other experiments indicate that the breakdown process for these cases is ion related.[16]

These experiments have successfully defined the criterion for designing self magnetically inhibited flashover insulators and have provided insight into vacuum insulator breakdown process physics.

References

1. R. H. Levy, Phys. Fluids, 8, 1288 (1965).
2. M. S. DiCapua, P. D'A. Champney, D. Pellinen, I. D. Smith and D. H. McDaniel, 2nd Int'l. Topical Conf. on High Power Electron and Ion Beam Res. and Tech., Ithaca, NY, 781 (1977).
3. J. M. Creedon, J. Appl. Phys., 46, No. 7, 2946 (1975).
4. A. Ron, A. A. Mondelli and N. Rostoker, IEEE Trans. Plasma Sci., PS-1, 85 (1973).
5. R. V. Lovelace and E. Ott,, Phys. Fluids, 17, 1263 (1974).
6. J. Creedon, J. Appl. Phys., 48, 1070 (1977).
7. S. Shope, J. W. Poukey, K. D. Bergeron, D. H. McDaniel, A. J. Toepfer and J. P. VanDevender, J. Appl. Phys., to be published.
8. D. H. McDaniel, J. W. Poukey, K. D. Bergeron, J. P. VanDevender and D. L. Johnson, 2nd Int'l. Topical Conf. on High Power Electron and Ion Beam Res. and Tech., Ithaca, NY, 819 (1977).
9. K. D. Bergeron, J. Appl. Phys., 48, 3065 (1977).
10. J. W. Poukey and K. D. Bergeron, Appl. Phys. Lett., 32, 8 (1978).
11. K. D. Bergeron and D. H. McDaniel, Appl. Phys. Lett., 29, 534 (1976).
12. K. D. Bergeron, J. Appl. Phys., 48, 3073 (1977).
13. Electron Beam Fusion Progress Rpt., October 1976-March 1977, p. 39.
14. Electron Beam Fusion Progress Rpt., April 1977-September 1977, p. 35.
15. K. Goto and K. Ishikeua, Jap. J. Appl. Phys., Vol. 7, No. 3, 227 (1963).
16. R. R. Anderson, Sandia Labs Rpt., SAND75-0667.

EBFA PROJECT

OVERVIEW

An engineering project office was established during the fall of 1976 to manage and coordinate all of the activities of the Electron Beam Fusion Project. The goal of the project is to develop the Electron Beam Fusion Accelerator (EBFA) and its supporting systems, and integrate these systems into the new Electron Beam Fusion Facility (EBFF). Supporting systems for EBFA include a control/monitor system, a data acquisition/automatic data processing system, the liquid transfer systems, the insulating gas transfer systems, etc. Engineers and technicians were assigned to the project office to carry out the engineering design, initiate procurement, monitor the fabrication, perform the assembly and to assist the pulsed power research group in the activation of the EBFA. The EBFA Project team is structured as shown in Fig. 1. The project team consists of separate working groups consist of 1) accelerator electrical systems, 2) accelerator mechanical systems, 3) data handling systems, and 4) the control/monitor system. A small team of engineers headed by a project engineer is responsible for each of these basic areas of the project.

PROJECT MILESTONE SUMMARY

A summary of the major milestones achieved by the EBFA Project during the reporting period are as follows:

1. The construction of the facility is approximately 70% complete with the erection of both the laboratory and office buildings.

2. The EBFA tank structure contract was awarded to Gaddis Machine Service of Albuquerque and approximately 50% of the pre-fabrication is complete. Assembly of EBFA will start by August 1978 at the facility site.

3. A prototype EBFA Marx generator was assembled to verify the mechanical fit of all redesigned parts, the utility of the new handling equipment, and the transportation philosophy. This Marx generator was also tested electrically to verify its design parameters. All Marx generator hardware has been procured.

4. The power flow concept of using Magnetically Insulated-Vacuum Transmission Lines to transmit power from a low electrical stress area of EBFA into the central high electrical stress area to circumvent the insulator flashover problem has been demonstrated on the MITE accelerator.

5. Radiation shielding calculations were conducted to establish the necessary shielding requirements to provide a safe operating environment for EBFA personnel.

6. The EBFA-II conceptual design study was performed, documented and transmitted to the Office of Laser Fusion. It was requested that Plant Engineering and Design funds be provided during FY79 and FY80 for Title I and Title II design of the EBFF-Phase II. These funds will also be used to complete approximately 35 to 50% of the engineering design of the EBFA-II before the Congressional budget hearings in the Spring of 1980. The proposed FY81 line item project would have a total estimated cost of $27.5M.

EBFF

OVERVIEW

During the reporting period, significant progress has been made on the construction of the new Fusion Research Facility (EBFF) by the general contractor R. E. McKee. The present status of construction can be seen in the aerial photograph of the new facilities shown in Fig. 2. The estimated percentage of completion has gone from 30% on October 1, 1977 to 72% on April 1, 1978, based on a revised schedule. The construction schedule was revised to accommodate a 41-day extension to the completion date granted by DOE/ALO because of changes requested by Sandia. However, the contractor still recognizes August 11, 1978 as the High Bay Laboratory beneficial occupancy date for the initial assembly of the EBFA tank structure.

It can be seen in Fig. 2 that both the office and laboratory buildings are constructed entirely of precast concrete tee sections. Shortages of high quality cement in the Albuquerque area during the summer of 1977 delayed the initial pouring and eventually the erection of

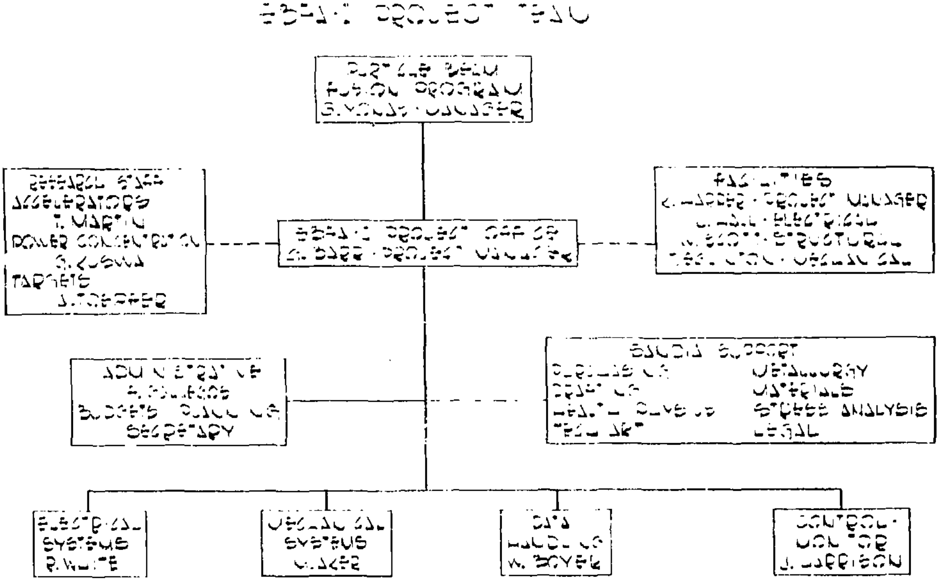

Fig. 1. EBFA-I Project Team

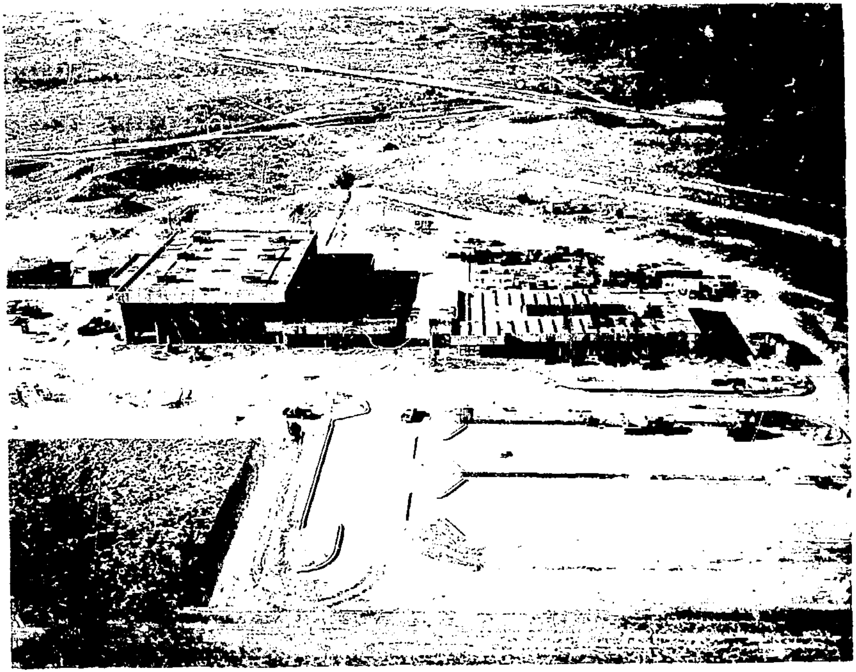

Fig. 2. Electron Beam Fusion Facility—aerial view.

these concrete tee sections several months. This in turn delayed the time period for the installation of the finished waterproof roof on the laboratory until January. Adverse weather conditions further delayed the roofing operation until March. At that time the roofing contractor was able to proceed with finishing the roofs on the Low Bay and the High Bay.

EBFA/EBFF Radiation Calculations

A radiation safety/hazards study was conducted during January/February 1978. The radiation protection required for personnel in an ICF accelerator test facility such as EBFF can be divided into two fundamentally different parts: 1) the prompt environment, and extremely intense localized, but short lived, burst of radiation; and 2) the delayed environment, a relatively low level, but distributed and possible long lived radiation source. For EBFA-I, these environments may be characterized as follows:

Prompt Bremsstrahlung - X-rays generated by the slowing down of charged particles. Bremsstrahlung will be emitted by every accelerator pulse involving the generation and deposition of electrons. The actual source characteristics will be determined by the energy of the electrons, the beam current, and the target material. To be conservative, the calculations were based on the assumption of 1 MJ of 2.5 MeV electron deposited on a gold target two times a day. For an unshielded source, the whole-body tissue dose to personnel present in the control room will be approximately 100 mrem/shot or about 50 rem per year. Thus, it is apparent that x-ray shielding will be necessary on EBFA-I. A removable segmented shielding wall has been designed into the accelerator near the central pellet chamber. The shield will be 4-inch thick steel mounted on the work platform supports. This shield wall will reduce the exposure in the control room to less than 1.0 rem/year.

Prompt Neutrons - Neutrons emitted from D-D or D-T fusion reactions. It was assumed for the calculations that EBFA-I would be capable of producing 10^{13} D-T neutrons per shot with one shot per day. This source contributed less than 50 mrem/year to the radiation dose in the control room, even without considering any shielding, and thus may be neglected.

Delayed Gamma Radiation - Gamma rays emitted from radioactive species produced by neutron reactions in the structure and materials around the source point. Delayed radiation will be present in the EBFA only following shots which produce a significant number of neutrons, i.e., 10^{17} to 10^{19}. When these high level shots occur, structures near the source point will be activated by the neutrons to the extent determined by the total source strength and energy spectrum of the neutrons, and by the chemical composition of the materials concerned. The resulting radiation field will vary spatially and will decrease in intensity with time. For a long series of neutron shots spaced more or less uniformly in time, a long-term but relatively low-level background radiation may build up. However, with the low level of neutrons expected with EBFA-I, i.e., 10^{13}, no delayed radiation source is expected and no shielding is anticipated at this time.

EBFA Supporting Systems

To support the operation of the EBFA presently being designed, several specialized systems must be designed and incorporated into the facility. These systems include:

1. Transformer Oil Transfer and Storage System

The transformer oil transfer and storage system was designed by the A-E, W. C. Kruger and Associates, and included in the initial construction contract for the facility and site improvements.

The initial criteria provided to the A-E for this system requested a 500,000 gallon storage capability to support the possibility of a completely oil-insulated accelerator, a maximum transfer time of one hour, and the capability to filter the oil and maintain its temperature at the inside ambient air temperature of the high bay. The present system consists of two 250,000 gallon above ground storage tanks placed in a concrete recovery basin. The oil is pumped between the storage tanks and the accelerator via 20" diameter lines by two 150 HP electrically driven pumps at approximately 10,000 gpm. The total quantity of transformer oil needed by EBFA-I in the present "April 78 Baseline" configuration is approximately 300,000 gallons with a less than 40-minute fill time. The future requirement for oil storage capability to support the upgraded EBFA-II will be approximately 430,000 gallons. The oil storage tank farm, including piping and valves up to the building, was completed and turned over to Sandia in December 1977 for oil storage. The first shipment of the required 300,000 gallons was received and stored at the facility site during January. The remaining portions of the system, i.e., the interior piping, the filters, the oil heater, the two main pumps, and the two smaller recirculate pumps have been installed. Power will not be available until July 1978 to perform the necessary systems tests.

2. Deionized Water System

The deionized water system will be designed by the A-E's mechanical subcontractor, Allison Engineering. Requirements for one hour or less transfer time of 200,000 gallons of water between the EBFA tank and storage have been established. In addition, the water will be continually circulated through the resin beds to maintain the desired quality at approximately 200 gpm. The engineered design should provide a certain amount of flexibility for the basic deionized water system with the provision for adding filtration, various water treatments and additional storage when the need has been identified.

3. Insulating Gas Systems

The Marx generator gap switches, the main energy transfer triggered gas switch, and several components on the trigger pulse generation system require sulpher hexafluoride (SF_6) or a mixture of high purity nitrogen and oxygen known as artificial air as an insulating medium. Accelerator wide systems for distribution of gases have been specified for the EBFF. Possible health hazards and an anticipated annual cost of over \$100,000 for SF_6 in a use and waste system led to a search for a recirculation and repurification system. Projected annual cost for artificial air of less than \$2,000 and no known health hazards make a use and waste system economically feasible for that gas. A commercially available SF_6 reclaiming system similar to those in wide use by the electric utility industry was found to provide the required flow (27 SCFM), pressure (up to 300 psig), and economy to provide EBFA with a continuous supply of clean SF_6.

The SF_6 reclaiming unit consists of a vacuum pump, compressor, 10 micron particle filter, soda lime and activated alumina chemical filter, refrigerated cooling system, heating coils and storage tank. It also includes appropriate valves and controls to route the SF_6 through the plumbing circuit to filter, clean, liquify, store and then regasify and deliver the clean SF_6 back to the EBFA.

A unit was purchased for the existing TA-V accelerator complex where operating experience will be obtained with a system identical to that planned for EBFA. This system will be operational about June 1, 1978, and final installation specifications for the EBFA are planned to be written and released by September 1978.

4. EBFA Data Acquisition System

The EBFA data acquisition system will initially have 44 Tektronix 7912 AD fully programmable transient digitizers. These digitizers will be used for recording signals that require high time (.2 ns per sample) and amplitude (8 bit) resolution.

The 7912 AD's will initially be used to fine tune and characterize the accelerator performance. They will then be dedicated to supporting experimental diagnostics. It will be necessary to monitor accelerator power levels and waveform timing at several stages along each of the 36 modules on every shot. Recording requirements for acquiring these signals are 1 - 5 ns per sample time resolution, 4 - 6 bit amplitude resolution, and 200-word record length. Several hundred channels will be required. Existing off-the-shelf digitizers are prohibitively expensive for the large number of channels. We have examined the possibility of developing special multichannel, low-resolution recorders to monitor accelerator performance. A

Request for Information for such a device was sent out to various electronic equipment manufacturers in January 1978. The replies were encouraging. The specifications have been rewritten and a RFQ will be released in June 1978. We are hoping to get 40 channels per mainframe at a cost of $1 - 2K per channel. We should have one or two operational recorders by June 1980.

The data acquisition system and the control/monitor system will have individual minicomputers. The two computers will be tied together by a serial communications link. Both computers will be purchased on the same contract via a competitive procurement, The final specifications have been approved by DOE. The contract should be placed late summer 1978. Both computers should be installed in the screen rooms by the end of February 1979. A block diagram of the proposed control/monitor and data acquisition systems is shown in Fig. 3.

The final drawings and specifications for the screen room to house the EBFA control/monitor system, data acquisition system and laser interferometer have been completed by Plant Engineering. The screen room enclosure is 15' x 105' and will be divided into three separately shielded rooms, one for each system. The control room will occupy the first 25 feet, the data acquisition system the next 65 feet and the last 15 feet is reserved for laser interferometer system. The shielding effectiveness will be tested by a second contractor independent of the manufacturer.

5. Control/Monitor System

The design definition for the EBFA control/monitor system has been completed. The system will be a distributed microprocessor system with a mini-computer for overall system control and monitor. A screen room will be used to protect the sensitive electronic components from EMP. Filters and transient suppressors will be used to prevent EMP from entering the screen room on cables. Fiber optics will be used for EMP protection of some subsystems.

An EMP measurement program using the MITE accelerator as the source has been completed and documentation is in progress.

Preliminary software studies have been carried out to determine minicomputer requirements. The minicomputer is in the procurement cycle.

A microprocessor card "family" has been selected and a breadboard system of four microprocessors is being constructed to check out the mini-computer interface. One of the four microprocessors will be built into an SF_6 control system and tested on an existing accelerator to check out the EMP protection plan. Software studies are in process to select a microprocessor software development system.

Preliminary design of the control/monitor cable way system is being done. Cable ways and junction boxes for the control/monitor system will be installed as part of the facility occupancy contract.

EBFA-I

"April 78 Baseline" Design

The "July 77 Baseline" design configuration for EBFA-I has experienced several modifications during the reporting period. The present EBFA-I configuration is shown in Fig. 4. This "April 78 Baseline" design for consists of 36 individual particle beam acclerators arranged in a radial geometry around a central experimental chamber, all within a concentric set of tank structures. Simultaneous operation of the 36 accelerators is accomplished by means of two firing systems - the Marx generator firing system and the gas switch trigger system. For discussion purposes, one can divide the accelerator into four sections: (1) the energy storage section, (2) the pulse forming section, (3) the power flow section, and (4) the front-end experimental section.

The energy storage section consists of 36, 116KJ Marx generator modules with an output voltage of approximately 3.2 magavolts, power supplies to charge the capacitors in the Marx generator, and the Marx generator firing system. These components are submerged in approximately 300,000 gallons of transformer oil for electrical insulation. The charging of the Marx generator capacitors requires approximately 90 seconds. The firing system consists of a pulser trigger unit firing 9 identical main pulser units which in turn each fires 4 Marx Generators. Remotely

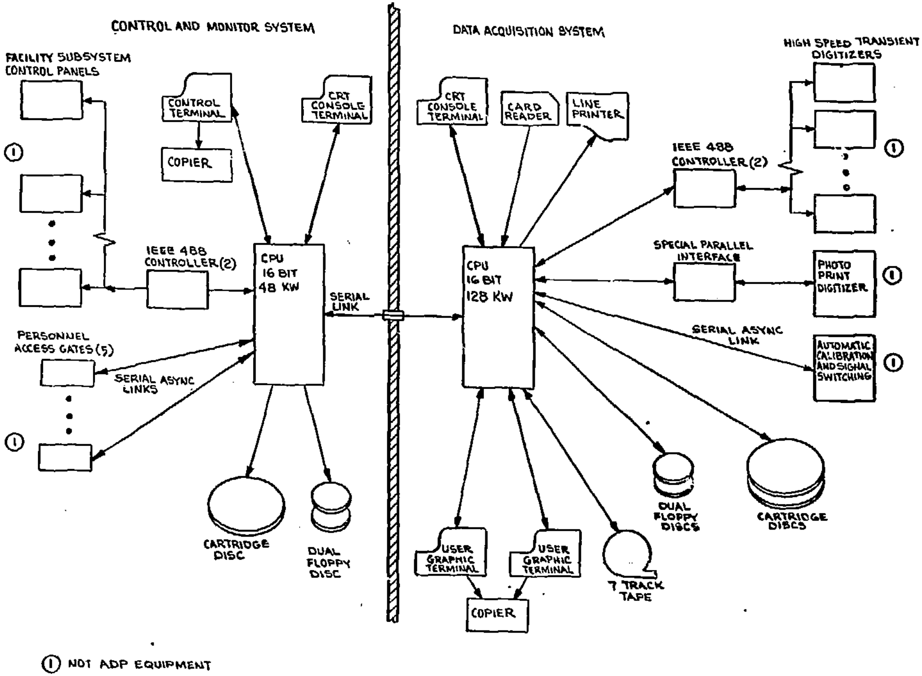

Fig. 3. Control/monitor and data acquisition systems diagram.

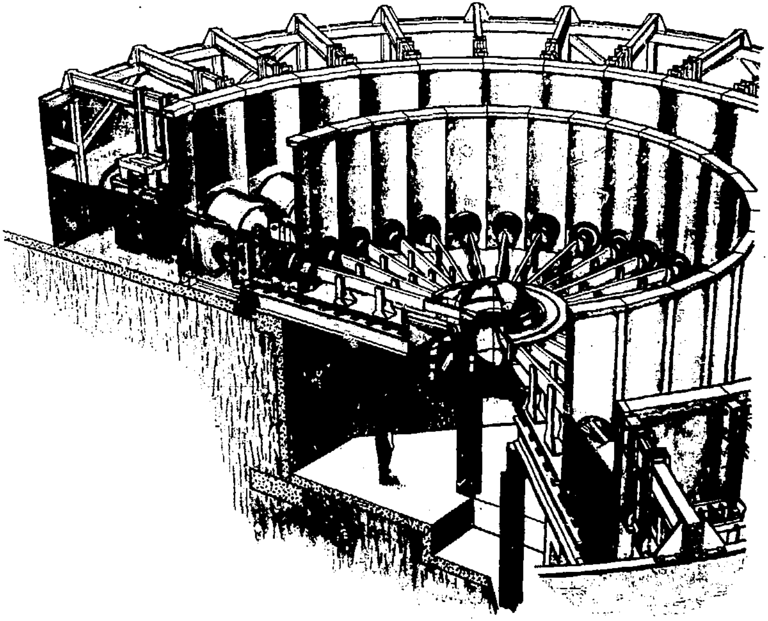

Fig. 4. Electron Beam Fusion Accelerator (EBFA) I.

operated transfer switches have been incorporated into the firing system to provide protection to the experimental set-up in the event of a premature discharge of either the Marx firing system or the Marx generator. In the safe position, all of the transfer switches are connected to resistive loads capable of dissipating the energy of the driving unit. These transfer switches also allow either the Marx firing system or the combined Marx firing system/Marx generator to be charged up and fired for a pretest check-out without injecting a pulse into the pulse forming section. The normal operating mode for the energy storage section would be to charge up the Marx firing system components and the Marx generator capacitors before moving the transfer switches from the safe position to the arm position. At t=o, the fire signal leaves the control room and fires the pulser trigger unit, which sends out nine simultaneous pulses to the main pulser units, each sending out four simultaneous pulses to the Marx generators. Each of these pulses fires the first row of spark gaps to rearrange the circuitry of the Marx generator from parallel to series to provide a voltage multiplying effect to occur during the discharge of the capacitors. The energy flows out of the Marx generator to a feed-through located in a High Voltage Barrier which separates the transformer oil insulated energy storage section from the water insulated pulse forming section.

The pulse forming section consists of a water insulated intermediate storage capacitor, a triggered gas switch, two parallel flat plate pulse forming lines each with self-breakdown switches, and a transformer line adapting the pulse forming lines to the vacuum interface. A self-breakdown prepulse suppression switch is located in the transformer section. These components are submerged in deionized water with a resistivity greater than 1.0 MΩ-cm for electrical insultation. The normal mode of operation of this section starts when the energy flows out of the Marx generator and resonantly charges the intermediate storage capacitor to near 3.0 megavolts in approximately 750 ns. At this time the gas switches are command triggered, and the energy is transferred to the pulse forming lines in approximately 200 ns. The self-breakdown water switches between the pulse forming line and the transformer section break down in a multichannel discharge further compressing the energy pulse to approximately 40 or 50 ns. After passing through the pre-pulse suppression switch, the energy pulse passes through a transformer section to the vacuum interface. This transformer section is designed to match the impedance of the load and provide a physical transition from the parallel plate geometry of the pulse forming lines to the cylindrical configuration of the vacuum interface insulator.

The power flow section consists of the vacuum interface and the Magnetically Insulated-Vacuum Transmission Line (MI-VTL). The MI-VTL concept for power flow was successfully demonstrated during this reporting period and is reported in detail in the pulsed power section of this report. The MI-VTL consists of two concentric racetrack-shaped hollow conductors approximately 17 feet long separated on each side by a 1.0 centimeter gap and approximately 2.5 centimeters gap at the top and bottom. The center conductor is cantilevered off the back plate of the vacuum interface. Approximately 50% of the energy flowing out of the pulse forming section into the vacuum interface is converted into electrons at this location. Great care is taken to inject these electrons properly into the MI-VTL so that the proper magnetic field is established. The electrons will then be trapped halfway between the center negatively charged conductor and the outside vacuum envelope which is at ground potential. The remaining 50% of the energy is transported along the MI-VTL with the trapped electrons in the form of an electromagnetic wave.

The front end experimental section consists of an experimental chamber capable of either being evacuated or pressurized. The MI-VTLs enter the chamber in a horizontal plane around the equator. Inside the chamber each center conductor necks down through a transition section to a cylindrical geometry approximately 2" in diameter. The Multiple Electron Beam (MEB) approach of generation, focusing, and transport of the electron beam is still the most promising pellet irradiation concept. The MEB concept involves using the center conductor of the MI-VTL pulse charged negative w.r.t. ground. The energy delivered to the end of the MI-VTL is converted into 36 individual electron beams between the cylindrical cathodes and the anodes which are formed by closing the outside vacuum envelope of the MI-VTL over the end of the center conductors. The tightly pinched electron beams then penetrate the thin anode foil located approximately 18 inches from the center of the pellet chamber. Each beam of electrons then follows a low density preionized channel in a background gas to the pellet. The low density channel is established by discharging a capacitor along a wire between the anode foil and the pellet just prior to the arrival of the electromagnetic wave at the cathode.

Several different pellet irradiation concepts are presently under investigation. A review of the concepts is scheduled for July 1978 to determine the most probable first experimental configuration to be installed on EBFA-I. However, the initial operational status of EBFA-I will be experiment independent, i.e., the transition sections and the anode/cathode hardware for the end of the MI-VTL will be provided for the initial check-out and verification of the various parameters of the accelerator.

The overall engineering design of the pulse forming and power flow sections was reviewed and approved during February 1978. This engineering design is based on the experimental results obtained using the MITE accelerator. These results are reported in detail in the pulse power section of this report. The MITE accelerator was developed as a physics test bed and not as a prototype for EBFA. Therefore, in order to minimize the risk associated with the EBFA, it was decided to use the first set of fabricated hardware made from the EBFA engineering drawing to assemble a single line exact mock-up of EBFA from the Marx generator to the front-end for engineering evaluation and performance characterization. This accelerator, called HYDRAMITE, will also be used (1) to demonstrate the mechanical aspects of assembly and operation, (2) to develop and verify the various accelerator diagnostics for EBFA, and (3) to verify the "Baseline" beam transport and focusing concept using the exact EBFA electrical characteristics. After the EBFA hardware design has been verified, authorization will be given to obtain the total quantity of hardware necessary to assemble EBFA. The EBFA schedule calls for assembling HYDRAMITE during November/December 1978, performing the initial pulse power and power flow tests during the January/February 1979 time frame. Authorization to fabricate the EBFA hardware during January/February 1979 with assembly of this hardware into the EBFA tank structure starting in June/July 1979. The initial pulsed power tests for EBFA are presently scheduled for October 1979.

The EBFF/EBFA project milestone chart has been revised to account for the assembly and engineering evaluation of the first set of EBFA hardware into the demonstration experiment HYDRAMITE. This revised milestone chart showing the schedule and status of each major system of the project is shown in Fig. 5. The engineering status of each of these major components or subsystems of the accelerator will be discussed in the following paragraphs of this section.

EBFA Tank Structure

The EBFA structure serves the dual function of providing (1) a frame for all of the other accelerator components and (2) several vessels to contain the transformer oil and deionized water used for insulation and dielectric purposes. Dictated by the basic concept of radially inward flow of energy in the EBFA, the tank structure has taken the form of progressively smaller concentric circular tanks sharing common walls. The structure is 100 feet in diameter and is 16 feet high. It holds 300,000 gallons of transformer oil and 150,000 gallons of deionized water in the EBFA-I version. About 600,000 lbs. of steel will be required in fabrication. A design philosophy was followed which will allow a wide range of changes to the accelerator components over the life of EBFA without major modifications to the tank structure.

The design definition package has been approved. Purchase activities were initiated which led to award of a fabrication contract on January 20, 1978. Planned activities for the next six months are prefabrication of the structure at the contractor's plant and start of on-site assembly work on or before August 11, 1978.

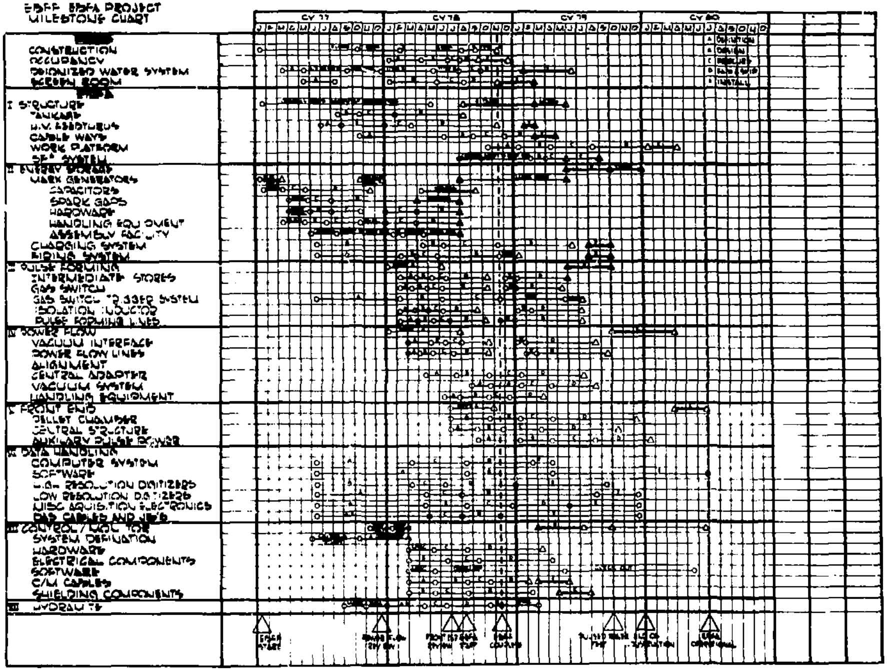

Fig. 5. EBFF/EBFA PROJECT MILESTONE CHART.

Marx Generator

A redesign of a large portion of the Marx generator hardware was undertaken in a successful effort to package the generator as an easily transportable plug-in module and to cut total Marx generator cost. Present Marx cost estimates of $0.24 per joule seem justified. A prototype of the EBFA Marx was assembled and tested for mechanical handling and electrical characteristics. The successful electrical tests performed in the Hydra accelerator demonstrated no conflict between the mechanical redesign and the high voltage characteristics of the generator. Plans for the Marx assembly line, storage area and transportation to the EBFA facility were developed. Events of the immediate future include purchase and delivery of all Marx components and start of assembly.

Charging System

The system will charge 1152 capacitors (420 microfarads) in the Marx generators using a dual polarity 100 kV system. Charging time will be from 60 to 90 seconds. The system will be a 220 kilovolt ± dual polarity grounded midpoint supply with a maximum charging current capability of one ampere. The specification will be written so that two high voltage output units will be furnished with each one contributing half of the total charging current. This will permit using either one of the high voltage units to independently charge the system in a somewhat longer time.

Marx Generator Trigger System

Criteria for the Marx generator trigger system have been determined, detailed specificiations have been written, and procurement activities initiated. The trigger system will have nine high voltage pulsers each to trigger four Marx generators, a pulser trigger unit to initiate the firing of the nine pulsers, and a control system capable of remote control and firing of the system. Consideration of expanding the system to trigger 72 Marx generators in EBFA II was given.

Transfer Switches

For system high voltage protection in case of prefires, outputs from the Marx generator trigger system and the Marx generators will be connected to resistive loads during the charging of these components. Hydraulically actuated transfer switches will connect the outputs to their appropriate high voltage terminals only seconds before shot time. Pressure transducers will be used to sense switch position to provide information to the control/monitor system. Preliminary layouts of the switches were shown to be feasible and work is proceeding to design and order the switches.

Intermediate Stores

Preliminary layouts and sketches of the water insulated intermediate storage capacitors were completed and approved. The capacitor geometry will be cylindrical, similar to the proven design used on Proto II, but will employ the feedthrough on the High Voltage Barrier separating the transformer oil from the deionized water as a mechanical support for the inner capacitor electrode instead of using a separate insulator. Detailed design and the initiation of purchase activities are scheduled to occur before September 1978.

Trigatron Switches

Locating the intermediate storage capacitor in the water section of EBFA required locating the gas insulated trigatron switch in that section also. The EBFA switch will be the same as is used in Proto II, but with the insulator length increased from 12 to 17 inches to provide an increased tracking length due to the water dielectric. Connections to the switch will be such that the switch may be removed without draining the water tank. By doing this, the lengthy process of removing bubbles from the underside of the switches after maintenance has been eliminated.

Pulse Forming and Pulse Transforming Lines

The pulse forming lines (PFL) are flat plate transmission lines which receive energy from the triggered switch, shape the energy pulse and suppress the prepulse. Results of lines operated on Proto II and MITE have lead to criteria layouts for the PFL for EBFA. Designs using aluminum plate, angle and channel shapes bent and welded by standard sheet metal shop techniques are under consideration. The pulse transforming lines (PTL) transform impedance and connect the output of the flat PFL to the circular vacuum interface. Along with many other EBFA components, the PFL and PTL may be completely assembled away from the accelerator and installed as a module. Both lines will be detailed and purchased within the next few months.

Power Flow

The power flow section of EBFA is composed of a vacuum interface and a vacuum power flow line. The vacuum interface penetrates a wall of the EBFA structure tank at the 40 foot diameter. The outer conductor of the power flow line is mechanically supported by the vacuum interface at its outer end and by a central structure at the other end about 6 feet from the center of the accelerator. The outer end of the inner conductor is cantilevered from the vacuum interface to the center of the accelerator where it is aligned with the outer conductor elastically. The power flow line conductors are fabricated from hollow aluminum extrusions. Each vacuum interface and power flow line set form an independent vacuum chamber which communicates with each other only through the ring-shaped manifold located under the tank floor. Detail design of both the vacuum interface and power flow line is expected to be completed by June 1, 1978.

Front End

The EBFA Front End is envisioned as accepting the inboard end of the power-flow lines in a manner which will allow a great deal of experimental flexibility. Clean breaks in the structure at diameters of about 36, 44 and 84 inches will allow various front end configurations to be used in the future. Features to permit 36 individual witness plates or 36 plasma channels to the pellet are to be designed.

EBFA-II

A conceptual design study defining our initial approach to EBFA-II was performed during the reporting period. With this conceptual design, the procedure to acquire funding for a FY81 construction line item project has been started. The procedure requires that Plant Engineering and Design (PE&D) funds be provided during FY79 and FY80 to do the Title I and Title II design of the new facilities. These funds would also be used to complete approximately 35 to 50% of the engineering design of the accelerator before the Congressional budget hearings in the spring of 1980. The first step in this procedure will be taken during April by completing the conceptual design proposal for EBFA-II and transmitting it to the Office of Laser Fusion with a request for the needed FY79 and FY80 PE&D funds. If the funds ($2.5 million) are provided, an architect/engineer firm will be contracted to do the Title I and Title II design during FY79. The Title I engineering design of the accelerator will be accomplished in parallel with the facility design by the EBFA-II Project Team.

The present plan is to upgrade EBFA-I using the existing tank structure, the existing liquid transfer system only increasing the storage capability where necessary, expanding the control/monitor system and the data acquisition/data processing system necessary to handle the increased capability of the upgraded accelerator. The construction of the new facilities requested to support and consolidate the Fusion Research effort will begin in October 1980 with an estimated completion date of July 1982.

The components necessary for the upgrade of EBFA will be procured during FY81 and assembled into modular units during FY82. EBFA-I will become operational in June 1980 and it is presently planned to operate for two full years with a shutdown for modifications scheduled for July 1982. The upgrade of the accelerator and all of the supporting systems is expected to require approximately 9 to 12 months. EBFA-II is expected to be operational by July 1983. A cross-section of EBFA is shown in Fig. 6 with the 30TW, 1MJ, EBFA-I on the left and the upgraded 60TW, 2MJ, EBFA-II on the right. The T.E.C. for the proposed FY81 line item is estimated at $27.5M.

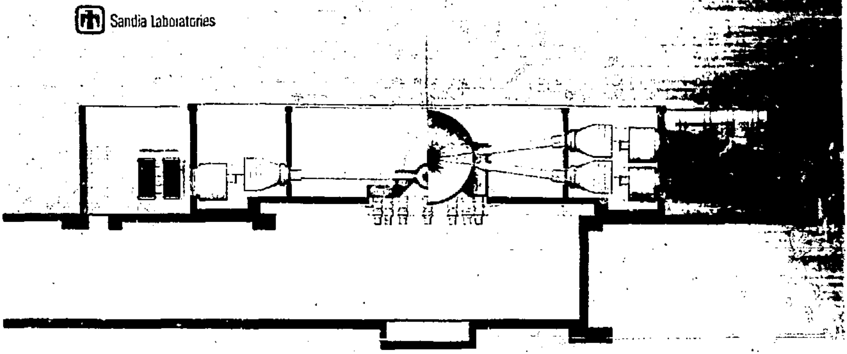

Fig. 6. EBFA cross-section.

THEORETICAL RESEARCH

OVERVIEW

Theoretical work on magnetically insulated targets has continued as a major effort. An important new phenomenon, called beam preconditioning, has been identified. Earlier magnetic target work concentrated on fuel preheating by the passage of a current directly through the fuel region. By contrast, beam preconditioning relies on the self-field of the beam to induce a local return current in the fuel region. This return current can provide all of the required heating and magnetic insulation for small targets, and can play an important role in boosting the temperature in larger targets preheated in the conventional way.

New high gain targets for electrons and ions based on the central igniter principle have also been studied. These targets use a cryogenic DT fuel layer which surrounds a low-density magnetic central igniter. The ion version produced a computed gain of 75 at 45 TW; earlier conventional (nonmagnetic) ion targets required about 60 TW for breakeven.

Near-term target design work for Proto II has been expanded to include 2-D calculations for studying the preheat phase. One-dimensional implosion computations based on the 2-D preheat results predict greater than 10^9 neutrons for a variety of assumptions about initial conditions. The 2-D preheat calculations were compared against results from the LLL ANIMAL code provided by I. Lindemuth. These comparisons confirmed the qualitative picture predicted earlier, namely that a low density, high temperature core is formed by the preheat process. Implosion calculations with ANIMAL also predicted neutron yields consistent with earlier estimates.

The most recent designs for electron beam fusion reactors employ many separate diodes located around the outside of a spherical target chamber. An electron beam is produced and focused in each diode and injected into a plasma channel of sufficient density and temperature to neutralize the self-fields of the beam. Magnetic fields are present in the channels to confine the electron flow and allow the beams to propagate to a common target. These fields are produced by externally supplied currents driven by a capacitor bank. Experimental results have been obtained which show that beams of about 300 to 400 kA can be propagated distances of 0.5 to 1.0 m with up to 80 percent efficiency. The scaling of these results, which used the HYDRA accelerator, will soon be tested on the 8 TW Proto II accelerator. Theoretical work in this area has included diode code calculations to investigate beam focusing and injection into the channel and a study of return current effects. The reverse electric field which is induced by the beam can in some cases lead to a spreading of the beam, as well as the usual ohmic energy loss. Return current heating was found to be a way to increase the channel conductivity and reduce the losses.

Theoretical diode physics work related to fast opening plasma switches has concentrated on the formation and behavior of double sheaths. These sheaths are thought to play an important role in the time evolution of the switch current. Additional computational studies of magnetic insulation in coaxial lines have been performed to compare with the Physics International experiments. Measurements of the total current at three locations along the 10-m line agreed well with 2-D electromagnetic code simulations.

The enhanced deposition of electrons, whereby the self-fields of the beam are used to increase the specific deposition in thin targets, has been an attractive possibility for some time. A new tool has been constructed to study the problem of enhanced deposition in diodes by combining a collisional Monte Carlo model with the PIC diode code. This code provides the first self-consistent treatment which includes the diode fields, self-fields, and collisional effects. The initial application of the code to HYDRA (0.1-0.2 TW) diodes found that simple scattering effects could not account for the pinch broadening seen experimentally, but scattering from expanded blow off regions near the axis was a possible explanation.

Other diode code applications included studies of the HERMES-II and Proto I ion diode experiments. The latter work showed that a good virtual cathode formed and that electron leakage was minimal. Studies of beam divergence and ways for controlling it are beginning.

Beam Preconditioned Magnetic Targets

A new, simpler type of REB target, which incorporates magnetic thermoinsulation and preheated fuel as the result of passage of a high current density REB through the target is under investigation. This approach, which is referred to as "beam preconditioning," is a variation of previously described "discharge preconditioning"[1] which can be provided by either machine prepulse current or by a separate power supply. Beam preconditioning following discharge preconditioning can significantly enhance or boost the fuel temperature and $\Omega\tau$ over that of either mechanism separately. We refer to this combined effect as "beam boosting." For the cases described here, the beam causes preheat from ohmic heating due to an induced conduction current in the fuel and the magnetic field results from an imbalance between beam and conduction current, which is due in part to resistive decay of the conduction current. The approaches discussed here are conceptually different than that previously reported by Meeker, et al.[2] in the method of preheat and field production. The following will describe the concept as well as results from a series of preconditioning calculations which look encouraging for high current density REB accelerators.

Beam preconditioning requires a target whose shell thickness is thin to electrons, which allows passage of the electrons through the fuel without substantial scattering in the shell, such as shown in Fig. 1. The diode configuration is similar to that used previously.[1,3] for single beam irradiation. In such cases the target is irradiated nearly uniformly with the beam behaving as a stagnated, hot electron gas with an axial current flow given by electron drift motion. During the early portion of the main beam pulse, it is assumed that the fuel is ionized to some degree either by direct electron deposition, shock heating or by breakdown from large diode electric fields. As a consequence, the fuel is a conductor and provides some degree of current neutralization by establishing an induced conduction current from the beam.[4] The induced conduction current then ohmically heats the fuel which increases the conductivity which in turn increases the induced current. The plasma conduction current in the fuel can be described approximately by

$$L \frac{dI_{net}}{dt} = -I_p R , \qquad (1)$$

where L = inductance/length, I_p = plasma current, I_b = beam current, $I_{net} = I_p + I_b$, and R = resistance/length. The plasma current rather than the net current decays resistively which gives rise to net current and magnetic field in the fuel. The process is complicated by the dependence of the plasma resistance on temperature or the amount of heating which further depends upon the induced current.

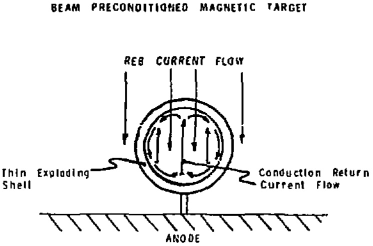

Fig. 1. Beam preconditioning configuration.

Several calculations were done using a zero-D model with average fuel parameters for a cylindrical fuel volume of specified radius r_t. The model includes two temperatures, Saha ionization, electron-ion equilibration, ohmic heating with $\Omega\tau$ corrections, electron thermal conduction with $\Omega\tau$ corrections, ion thermal conduction, and free-free and free-bound radiation loss. The time evolution of T_e, T_i, $\Omega\tau$, and other quantities are then calculated for a given beam current, fuel density, fuel composition, and r_t. The plasma current is computed from Eq. 1 with L based on a uniform current density assumption.

The parameters for the sample DT fuel calculations shown here are the beam current $I_b = I_0\, t/t_R$, the rise time t_R = 20 ns. For beam preconditioning only, we assume an initial temperature T_0 = 0.5 eV, and for beam boosting calculations T_0 is chosen larger ($T_0 \lesssim 16$ eV). We chose r_t = 0.1 cm.

Plotted in Fig. 2 are T_e and T_i (at t = 20 ns, prior to implosion) vs. the density ρ for several I_o values. T_o = 0.5 eV, $10^{-6} \leq \rho_o \leq 10^{-3}$, and $J_o = I/\pi r_t^2$ (amps/cm²). Note that beam preconditioning is more effective at lower densities where ohmic heating is more effective, although electron-ion equilibration becomes a problem for very low densities because of the fast heating rate. The heating process is in some sense a bootstrapping process in that as the fuel becomes hot, more return current is induced which leads to further heating. We see beam preconditioning begins to become effective for beam current densities J ~ 3 MA/cm² and produces very large preheat for J ≥ 10 MA/cm². Not shown are the corresponding values of $\Omega\tau$ which are ≥ 1 for the large temperature T ≳ 10 eV, $T_e \approx T_i$ portion of each curve.

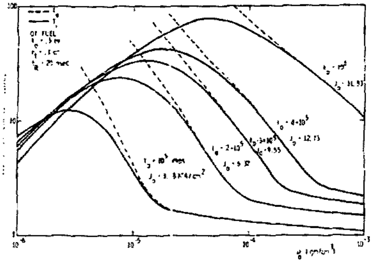

Fig. 2. Fuel temperature at 20 ns vs. fuel density for several beam current densities.

For present accelerators, it may be difficult to obtain the high current density needed for beam preconditioning alone and thus beam boosting may be required. To investigate this we consider a fixed $I_o \cong 10^5$ amps, r_t = 0.1 cm, and calculate fuel temperature at $t = t_R$ = 20 ns for various ρ_o. To model prior discharge preconditioning, *we simply start the* problem with an initial temperature 0.5 eV ≤ T_o ≤ 16 eV as shown in Fig. 3. Shown are T_i at t = 20 ns. T_e departs from T_i for $\rho_o \lesssim 10^{-5}$. Note in all cases considerable increase over T_o is obtained and considerable increase over the T_o = 0.5 case (beam preconditioning only) is seen for $T_o \gtrsim 2$ eV. Thus some slight preheat due to a low level discharge improves the performance considerably. Reducing the discharge current may permit smaller electrodes and improved implosion symmetry. We also calculate $\Omega\tau \geq 1$ for the cases which resulted in high temperature.

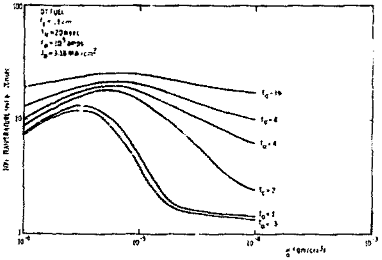

Fig. 3. Fuel ion temperatures at 20 ns vs. fuel density for several initial temperature values with beam current density fixed.

Next we calculate neutron yields for several conditions given in Fig. 3 using a hydracode. These are tabulated in Table I. The inner target radius is 0.15 cm and shell thickness is 0.0288 gm/cm² of plastic. The deposition in the target was chosen consistent with magnetic enhanced deposition due to self beam fields for various amounts of incident beam current which is limited to that available on the Hydra and Proto I accelerators. The fuel density is 10^{-5} gm/cm³ for all cases.

Scaling of Targets Employing Magnetic Thermoinsulation for Proto II

Recent experiments[5] have tested the concept of a particle beam fusion target which utilizes the passage of an electrical current *through the fuel to* both preheat the fuel and to establish a magnetic field in the fuel, before implosion of the target. The success of the experiments in producing ~ 10^6 thermonuclear neutrons emphasizes the need to determine the scaling of the concept for higher power, near-future accelerators to breakeven power levels, and finally to high gain designs

TABLE I

	T_o(eV)	T_e(eV)	T_i(eV)	P_m(TW/g)	Neutrons (10^6)
1	0.5	4.05	3.69	16	1.97
2	0.5	4.05	3.69	32	10.80
3	2.0	18.70	14.60	16	9.76
4	2.0	18.70	14.60	32	46.20
5	8.0	27.40	20.50	16	16.30
6	8.0	27.40	20.50	32	71.40

which may be suitable for reactor use.

The Proto II accelerator opens the possibility of driving electron beam targets at ≥ 1 TW absorbed power, assuming that suitable pinching of the beam can be obtained. Extending the exploding shell "ϕ" target design to that higher power level implies a larger target radius to efficiently utilize the available energy.[6] Matching to expected Proto II parameters (≥ 1 TW absorbed, 50 ns, ~ 1 MV) leads to a target of ~ 7 cm diameter, having the same shell thickness as the previous target (ρr = 0.03 g/cm^2).

We have assumed an initial fill density for this target of 5×10^{-4} g/cm^3 of DT gas. Using the 2-D MHD Eulerian hydrocode BEMAG, and postulating a 1/4 sine wave current pulse, 20 kA in amplitude and 2 μsec in duration for the preconditioning pulse, we obtain the preconditions shown in Fig. 4. Current flows from top to bottom in this figure, for which density contours and Br contours are plotted. The Br lines correspond to envelopes of fixed enclosed current. Temperatures in the lowest density region, $\rho < 10^{-5}$ g/cm^3, are calculated to be 15 to 30 eV, while the temperature in the higher density region, $\rho > 5 \times 10^{-4}$ g/cm^3, is less than 0.5 eV. The pressure across the target is uniform to within a factor of three.

This calculation is made assuming that the target contains a known total current, but the current path, resistive heating, and hydrodynamics are treated self-consistently. The gas is assumed initially electrically conducting, that is, the details of the breakdown process have not been considered.

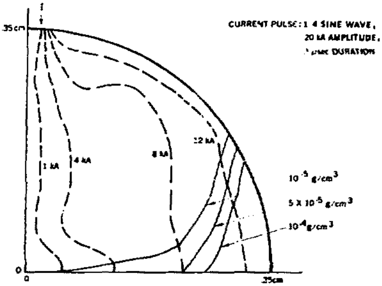

Fig. 4. Preconditions established in 1 TW target as calculated using BEMAG.

Using a 1-D hydrocode we have modeled the implosion, with the initial volumes of low and high density fuel chosen to be consistent with the fuel conditions determined using BEMAG. We find that the yield exceeds 10^9 neutrons for a variety of assumptions about the initial conditions. For the 1 TW target, we find a maximum temperature of 600 eV, a maximum density in the low density region of 0.035 g/cm^3, and a yield of 2×10^9 neutrons.

In Fig. 5, we have plotted the curve of yield vs. power for the target. The yield curve corresponds approximately to a cubic function

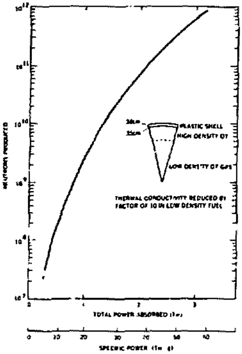

Fig. 5. Scaling of the 1 TW electron beam target with absorbed power.

of the absorbed power. It is noteworthy that the lower end of the curve, which corresponds to 5 TW/g or approximately present specific power levels produces $\gtrsim 10^7$ neutrons for this larger target. If a pinch of the Proto II beam can be formed at dimensions comparable to the target, at the much greater current of that machine, considerably higher specific power may be expected.

Utilizing the preimplosion conditions predicted by the BEMAG code, we have begun to study the 2-D aspects of the implosion using a Lagrangian code. Although the modeling of the full implosion has not yet been accomplished, two significant results have been obtained which tend to confirm our predictions using 1-D modeling. The code first of all confirms that the magnetic field is retained in the preheated fuel and is compressed during the implosion to produce the large $\omega\tau$ condition required for successful utilization of the magnetic thermoinsulation concept. Finally, the nonuniform initial distribution of fuel density leads to a radial deformation of the exploding shell late in time (see Figs. 6 and 7), but for the conditions tested (~ factor of 20 variations in fuel density) the pusher appears to remain intact until after temperature and pressure conditions are obtained which are similar to the maxima obtained in 1-D calculations.

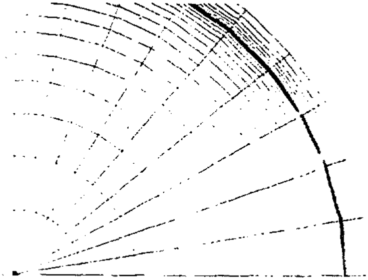

Fig. 6. Initial mesh used for investigation of 1 TW target.

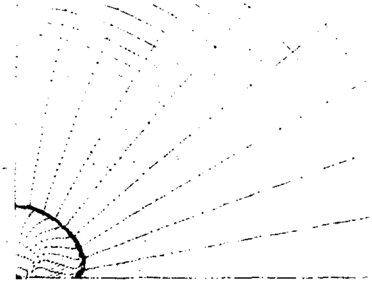

Fig. 7. Mesh of 1 TW target at 50 ns. Note pusher asymmetry, which leads to eventual breakup of pusher.

Breakeven and High Gain Magnetic Targets

The targets discussed thus far have been of the exploding shell type. In order to scale to breakeven or net energy gain, it is necessary to employ thick-walled, ablatively driven shells. Shown in Fig. 8 are ablatively driven e-beam and ion beam targets which utilize strong magnetic fields to inhibit thermal conduction losses, and for which the breakeven

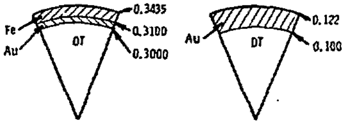

	ELECTRON BEAM TARGET	ION BEAM TARGET
P	5×10^{13} watts	10^{13} watts
V	1 MeV	10 MeV
I	50 MA	1 MA
τ	60 nsec	23 nsec
t_i	80 nsec	23 nsec
ρ_f	.0005 gm/cm^3	.001 gm/cm^3
T_0	30 eV	50 eV
G	1.26	1.06

Fig. 8. Electron and ion beam breakeven targets.

power is lower by a factor of 6-7 than similar targets without magnetic fields. Scaling to breakeven requires a magnetic field sufficient not only to reduce the thermal condictivity, but also to retain the α-particle fusion energy in the reacting fuel as well. This leads to the requirement BR >> 0.5 T-m at full compression.

Scaling of the targets beyound breakeven with increased power is not rapid, as can be seen from Fig. 9 for ion targets. The competing needs of low density for reduced radiative losses and high density (actually high $<\rho R>$) for large burnup fraction are responsible for this relatively poor scaling beyond breakeven. Even with this slow scaling, targets containing magnetic fields show gains of about three at powers lower than the breakeven power for more conventional targets.

To obtain higher yields it is necessary to utilize more fuel in the target, either by increasing the target size while retaining the low density, low energy-loss feature of these targets, or by adding a high density layer of fuel around the magnetically thermoinsulated region. This latter approach is illustrated in the ion target of Meeker, discussed by Bangerter and Meeker,[7] a version of which is shown in Fig. 10. Shown in the same figure is an electron-beam driven target employing the same concept, which is derived from the earlier electron driven breakeven target by adding a thin layer of solid density DT between the gold pusher and the low density, preheated and magnetically thermoinsulated fuel, and by relaxing the magnetic field requirement so that particles escape the reacting central region to ignite the surrounding high density region. The power required to drive each of these targets is significantly reduced by using the technique of voltage shaping, which is discussed in the next section.

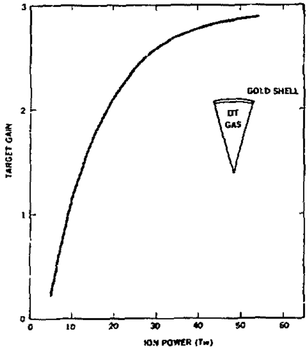

Fig. 9. Scaling of breakeven ion target with power.

Central Igniter Magnetic Targets with Voltage Shaping

Ultimately, targets with net energy gain considerably greater than one, but with relatively modest input energy and power requirements, will be needed for commercial inertial confinement fusion reactors. Ablatively-driven electron-beam and ion-beam fusion targets which contain preheated low-density fuel and a strong magnetic field to trap alpha particles and

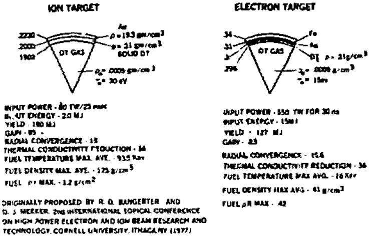

Fig. 10. High yield electron and ion targets.

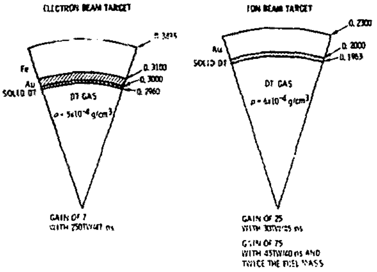

Fig. 11. Magnetic charged-particle-beam targets with propagating burn and voltage shaping.

inhibit thermal conduction losses are predicted[6] to achieve breakeven at powers 6-7 times lower than similar targets without magnetic thermal insulation, however, the power reduction possible is limited because as an ablative implosion proceeds, the ρr of the shell increases and energy is deposited further out in the ablator and is therefore used less efficiently late in time. Furthermore, scaling to a gain greater than 3 is difficult for these magnetic targets because of the competing needs of low density for reduced radiative losses and high ρr for good burn-up efficiency.[6,8]

We have investigated a class of high gain fusion targets which employ direct beam deposition (Fig. 11). The targets have a solid DT fuel layer outside a low-density magnetic central igniter.[9,10] Propagating burn results because alpha particle energy from the magnetic core is deposited in the outer solid-density fuel layer. We find that the thickness of the solid fuel layer is crucial to target behavior. If the layer is too thick, the low-density central-igniter region reaches maximum temperature before the solid fuel is sufficiently compressed to trap alpha particles and reach ignition temperatures. If the layer is too thin, its ρr will not be sufficient to trap alphas even if the maximum ρr occurs at the time of maximum temperature in the low-density fuel region.

Magnetic central igniters have the disadvantage that burn efficiency and target ρr are decreased.[9] We have employed voltage shaping[11] to offset this disadvantage and to reduce the power level necessary for high gain in such targets. Increasing the beam voltage during the pulse causes energy to penetrate deeper into the shell, producing a higher fuel ρr and a greater burn-up fraction as a result of the faster inward acceleration.

For electron beams, the effectiveness of voltage shaping is sensitive to the time history of the beam pulse with respect to the dynamics of the metal shell. Target performance is less sensitive to the voltage pulse shape for ion beams because of the absence of bremsstrahlung; however, voltage shaping with ions requires tighter focusing at higher voltages, since the peak of the deposition is at a smaller radius.

For ion beams, the variation in ion velocity with voltage ($v_i \propto \sqrt{V}$) can be used, as suggested by Winterberg,[12] to obtain a voltage pulse--much like the voltage pulse in Fig. 12--which is compressed spatially and temporally compared to the voltage pulse at the diode. In our calculations we assume that the power remains constant as voltage increases in order to obtain the minimum deposited power to produce large gain. Constant-power voltage shaping with ions should be applicable to heavy-ion fusion accelerators[13] or multistage magnetically insulated pulsed ion accelerators[14] because with such schemes, voltage and current can be varied somewhat independently. Under the constant power assumption, voltage shaping applied to magnetic targets reduces the power level required for the same gain by about 1/2 for both electrons and ions.

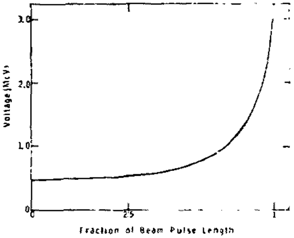

Fig. 12. Increase in voltage with time for a typical voltage-shaped target.

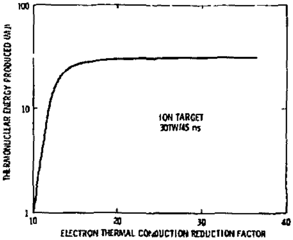

Fig. 13. Variation in thermonuclear yield with thermal conduction reduction factor for a magnetic ion target.

If a magnetic target only contains a low-density fuel region, the magnetic field must be strong enough to retain alpha particles in this region; if the target contains a solid DT shell as well, the field need only reduce thermal conductivity in the low-density fuel. We have assumed that thermal conduction is not reduced in the cryogenic layer. We have also assumed that the thermal conductivity is reduced by a factor of 36, to the ion conduction level for DT. Several calculations with smaller reduction factors indicate that the thermonuclear yield does not decrease greatly until the electron thermal conductivity reduction factor is less than about 13 (cf. Fig. 13). Furthermore, if we postulate that the magnetic field penetrates into ~ 2 percent of the mass of the solid fuel region so that the conductivity is reduced there as well, the gain at a given power level for the electron beam targets increases by a factor of about 3; one would then obtain a gain of about 20 for 250 TW of electron-beam power.

Figure 14, which shows thermonuclear energy production as a function of deposited beam power, displays the improved performance that can be obtained from central-igniter magnetic targets for both ions and electrons. A conventional electron-driven ablative target requires ~ 1000 TW to get a gain of about 8.5. A magnetic target with voltage shaping requires 280 TW to achieve this gain, i.e., roughly a factor of 3.5 lower power, and if the magnetic field penetrates into the cryogenic layer only a short distance, this gain will increase considerably. A low-power conventional ion-beam target requires about 60 TW of power for breakeven.[15] The low-power magnetic alternative

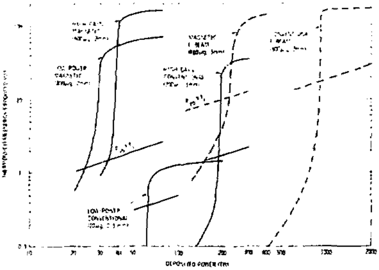

Fig. 14. Comparison of thermonuclear energy produced vs. input power for conventional ablative targets and magnetic targets with propagating burn and voltage shaping. The straight lines indicate the total beam energy deposited if beam power is turned off at the time of maximum compression t_1. Results for ion targets are indicated by solid curves; results for electron targets by dashed curves. The particular designs selected had the highest gain for the lowest power level. The ion targets have gold shells; the electron targets, iron-gold shells.

requires only 30 TW to produce a gain of 25. The high-gain magnetic ion target requires 45 TW to get a gain of 75, whereas a conventional high-gain target for ions requires 250 TW just to produce a gain of 18.[16,17]

The improvement in power is even better than indicated by Fig. 14 since the magnetic targets produce more favorable results at larger target size than do the conventional targets, implying longer pulse lengths (~ 50 ns) and reduced focusing requirements. A comparison of the magnetic ion target with a conventional target of the same size (fuel radius $r_{DT} = 2$ mm) shows that a gain of 25 would require 450 TW,[16] whereas the magnetic target produces a gain of 25 at 30 TW.

Even without voltage shaping, the power levels required for high gain are at least a factor of two lower in the case of electron beams and at least a factor of three lower in the case of ion beams. Furthermore, the overall radial convergence ratio of the fuel (18-22) is comparable to that obtained with conventional electron- and ion-beam targets and only a modest preheat temperature of 15 eV is needed. The convergence ratio in the low-density fuel region by the time ignition commences in the solid fuel region is slightly higher; however, since the region adjacent to the central DT is also DT, mixing of the inner and outer fuel might actually improve target performance by involving more fuel at an early time.

Two-Dimensional Calculations of Magnetic Thermoinsulated Targets

Previous two-dimensional calculations[18] using the BEMAG code of magnetic target preconditioning indicate development of a wall confined discharge with low density, high temperature fuel occupying most of the target volume prior to implosion. This behavior has been confirmed using the 2-D ANIMAL code written by Dr. I. R. Lindemuth of LLL. The ANIMAL code includes ionization, resistive diffusion, thermal conduction with full $\omega\tau$ dependence, radiation, magnetic fields due to both plasma and beam currents, and spherical geometry. The ANIMAL calculation is then continued through the implosion phase with self-consistent variation in fuel density, temperature and magnetic field. Neutron yields of $\sim 10^6$ are predicted for a convergence ratio of 20:1 which is consistent with experimental observation.[1]

Shown in Fig. 15 is an ANIMAL solution of fuel temperature and density vs. radius on the equatorial plane. The conditions are: initial uniform DT fuel $\rho_0 = 2 \times 10^{-5}$ gm/cm^3, initial uniform fuel temperature $T_0 = 1$ eV, target radius = 0.15 cm, electrode radius = 0.05 cm, and discharge current I(amps) = 1.2×10^4 (t/1 μsec). The plots are given at t = 1 μsec just prior to implosion. The BEMAG code predicts qualitatively similar results with peak temperature of 24 eV and density in the hot region of 1.3×10^{-5} gm/cm^3. BEMAG predicts the hot region to be located on axis between the target center and the electrode while ANIMAL predicts the hot region in the target center. These differences are thought to be due to differences in zoning and to differences in the spherical fuel boundary which is smooth for the ANIMAL model but approximated by an irregular boundary for the BEMAG model. There are also differences in the radiative cooling model in that ANIMAL includes line radiation, bound-bound, and free-bound loss, while BEMAG does not include line radiation loss.

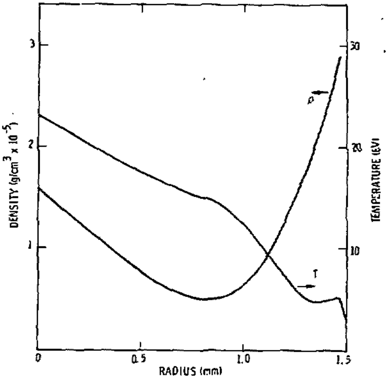

Fig. 15. Density and temperature profiles at t = 1 μsec from the ANIMAL calculation.

Further calculations of preconditioning using BEMAG indicate lower density, higher temperature fuel conditions can be achieved with smaller electrodes and by starting with an ionized plasma column along the fuel axis. The ionized plasma column is observed in "bench" preconditioning experiments.[19]

Predicted Temperature at Inner Surface of Shock-Focusing Hemispheres

Time-resolved temperature measurements of the inner surface of two thick-walled (shock-focusing) hemispheres during the implosion have been obtained.[20] The shell of each target was a composite, consisting of a thick outerlayer of gold or nickel and a thin inner layer of tungsten (cf. Fig. 16). The experimentally measured temperature was significantly lower for the Au-W hemisphere compared to the Ni-W hemisphere (2 to 4 eV vs. 5 to 10 eV).

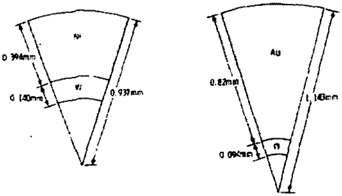

Fig. 16. Target dimensions in the temperature measurement experiments.

One-dimensional, spherical implosion calculations were performed for the actual experimental conditions (1 MeV, 80 ns, 8 kJ). Predicted implosion times are in agreement with the experimental times of 100 to 150 ns for Au-W and 70 to 80 ns for Ni-W. Good agreement with the experimental Ni-W temperature was obtained (10 to 15 eV), but the code results predicted 15 to 20 eV for the Au-W hemisphere (cf. Fig. 17). Heating of the inner surface of the Ni-W hemisphere by beam deposition should be greater because of the thinner shell. The discrepancy between the measured and predicted temperatures may be indicative of the sensitivity of shock-focusing targets to uniformity of loading, since less smoothing of the implosion should occur for the thicker-shell Au-W configuration.

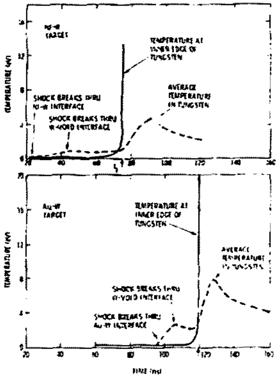

Fig. 17. Temperature at inner edge of tungste and average temperature of tungsten vs. time from code calculations of the two targets.

STANDOFF AND REACTOR RESEARCH

Diode Focusing and Channel Injection

Results from the Hydra series of beam propagation experiments indicated that considerable care in alignment was required to insure efficient injection of the focused beam into the channel. The problem was studied computationally using a version of the particle-in-cell diode code modified to include a short section of the channel.

A 3" OD, 1" ID tapered cathode K emits electrons which pinch and enter the channel C through a 1-cm diameter hole in the anode A, as shown in Fig. 18. The beam is then transported in the channel to a target. Using the nonuniform mesh diode code, various parameters were tried; for the case in Fig. 18, V = 1 MV,

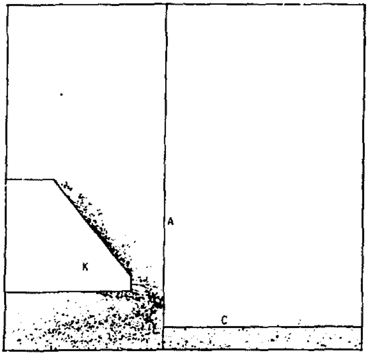

Fig. 18. Simulation electrons in the Hydra-channel experiment. About 200 kA propagates down the channel C.

$I_e = 320$ kA, $I_i = 80$ kA, and 60% of I_e (~ 200 kA) propagated down the channel to the end of the computation region. The rest of the electrons were lost on the anode at radii greater than the hole radius. The beam current in the plasma channel C was assumed to be completely neutralized, so that the only B_θ in the channel is from the channel current itself (here taken as 50 kA and uniformly distributed in the channel cross section). These results indicate that those electrons which enter the channel are not lost in the injection process.

A separate analytic calculation of the maximum radius attainable by a beam electron injected transverse to the channel gives

$$r_{max} = r_o \exp(2\pi m\gamma V_o/e\mu_o I)$$

where r_o is the channel radius, γ = relativistic factor, V_o electron velocity, and I = channel current. For the Hydra experiment, this gives $r_{max} = 8$ mm (for $r_o = 5$ mm). This result also indicates that electrons entering the channel are confined by its magnetic field.

Return Current Effects

Plasma channels used in beam propagation experiments are typically initiated by exploding long, thin wires in air at 1 atm.[21,22] Although the current initially is carried by the wire, an air discharge occurs rapidly; the wire appears to have little effect after the discharge forms. As the current increases (to about 50 kA in a few microseconds), the center of the discharge is ohmically heated. This causes an outflow of plasma and the eventual formation of an outward going shock wave in the air. It leaves behind a region of low density ($\rho/\rho_o \simeq 0.3$), high temperature ($T = 1.5$ to 2.0 eV) plasma which contains the magnetic field required to confine the beam. It is also essential that the radius of this region be small when the beam is injected. Otherwise, the beam tends to expand to whatever radius encloses the Alfvén current. Equal beam and channel radii are desirable.

As the beam is injected into the channel, the inductive electric field near the beam head generates a return current $j_p = \sigma E$. For a uniform conductivity channel of radius r_c, with a coaxial return at a radius r_W, the net current is given by

$$\frac{I_{NET}}{I_B} = \frac{\tau_D}{t}\left[e^{-t/\tau_D} + t/\tau_D - 1\right] ,$$

$$0 \leq t \leq \tau_R , \qquad (2)$$

$$\frac{I_{NET}}{I_B} = 1 + \frac{\tau_D}{\tau_R}\, e^{-t/\tau_D}\left[1 - e^{\tau_R/\tau_D}\right] ,$$

$$t \geq \tau_R , \qquad (3)$$

where the beam current was assumed to rise linearly to a value I_B in a time τ_R and remain constant for $t > \tau_R$. The diffusion time τ_D is given by $\tau_D = 4\pi \times 10^{-9}\sigma/\beta^2$ where β is determined by

$$J_0(\beta r_c) = \beta r_c J_1(\beta r_c) \ell n(r_W/r_c) .$$

For channels of interest, $\tau_D >> \tau_R$. In this limit Eqs. (2) and (3) can be written

$$\frac{I_{NET}}{I_B} \simeq t/2\tau_D \ , \quad 0 \leq t \leq \tau_R \ , \qquad (4)$$

$$\frac{I_{NET}}{I_B} \simeq \frac{2t - \tau_R}{2\tau_D} \ , \quad t \geq \tau_R \ . \qquad (5)$$

As an example of typical values, air at 2 eV and $\rho/\rho_0 = 0.3$ has a conductivity of about 250 mho/cm. For $r_c = 0.3$ cm, $r_W = 15$ cm, and $\tau_R = 20$ ns, we find that $\beta = 2.33\ cm^{-1}$ and $\tau_D = 580$ ns, so that at $t = 60$ ns, $I_{NET}/I_B = 0.086$. This result shows that the degree of current neutralization is very high.

As the electron beam propagates in the channel, it loses a fraction of its energy to the background plasma. Collisional losses are usually inconsequential, but losses due to ohmic dissipation of the return current, j_p^2/σ, can be of significance. The electric field, j_p/σ, which drives the return current opposes the electron flow, thereby converting beam energy to internal energy of the plasma. We estimate the magnitude of the effect by first setting $j_p \simeq j_B$, justified on the basis of the current neutralization calculation. For $r_B = 0.3$ cm and $I_B = 500$ kA, $j_B = 1.8 \times 10^6\ A/cm^2$ and $E_p = j_p/\sigma = 7.2$ kV/cm. The upcoming Proto II experiments will use 50 cm long channels, so that the electrons could lose 360 keV of energy, which is a significant fraction of their initial 1.0 to 2.0 MeV.

Fortunately, there is a time-dependent effect which improves the propagation conditions. As the return current heats the channel ohmically, the temperature and the conductivity increase, thereby reducing the losses. To determine the value of the conductivity increase, it is necessary to include ionization, radiation diffusion, channel expansion, and the temperature dependence of the conductivity. We have thus studied the problem using the 1-D MHD code CHART-B employed in earlier studies of the channel formation in air. The hydrocode was first used to establish appropriate channel conditions prior to beam injection by using a capacitor bank drive. When the channel radius reached a value of $r_c = 0.24$ cm, an ohmic heating term j_B^2/σ was added whose time history was consistent with a total current which increased linearly to a value of $I_B = 500$ kA in a rise time $\tau_R = 20$ ns, remained constant for 20 ns, and then dropped linearly to zero in 20 ns. The high degree of current neutralization again justified the use of $i_p \simeq j_B$ for the ohmic heating contribution.

Results of the calculation are shown in Fig. 19. The left half of the figure shows the input current history and the channel temperature and density profiles at the time of beam injection. The right half of the figure shows the results for the electric field j_p/σ as a function of time and the channel profiles at $t = 40$ ns. The average electric field during the flat portion of the current pulse was 5 kV/cm, so that a 2 MeV beam would lose about 12.5% of its energy in 50 cm. This was found to be consistent with $\int\int j_p^2/\sigma\ dV\ dt$, as it should be. The channel temperature increased from 1.7 eV to 6.4 eV, which led to a conductivity increase of a factor of three.

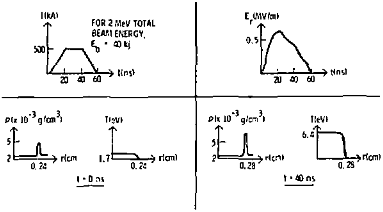

Fig. 19. Results from return current heating calculation. The upper left-hand portion shows the input current waveform; the lower left-hand portion shows the channel density and temperature profiles at t = 0. The upper right-hand portion shows the computed electric field vs. time; the lower right-hand portion shows the channel properties at t = 40 ns.

Another positive result shown in Fig. 19 is the channel radius at t = 40 ns, which is only 17 percent greater than the initial value. This modest increase is a result of the inertial confinement properties of the air. As the electrons are bent by the magnetic field in the channel, they impart radial momentum to the plasma. A simple estimate based on a lumped mass constant acceleration model gives a channel radius increase of

$$\frac{\Delta r_c}{r_c} = 3.3 \times 10^{-4} \frac{V_B I_B t^2}{\rho \pi r_c^4} . \qquad (6)$$

For V_B = 2 MeV, I_B = 500 kA, t = 50 ns, ρ = 2.5 x 10^{-4} gm/cm^3, and r_c = 0.3 cm, one finds that $\Delta r_c/r_c$ = 0.13. The dependence on the channel radius r_c is very strong and smaller channels would suffer greater expansion.

A final return current effect on the beam is a spreading and particle loss caused by the combined electric and magnetic fields. For very small electric fields, the electron trajectories are of the well-known betatron sinusoidal variety. At larger field values the radius of the electron orbits increased as a function of propagation length, since the electric field tends to convert parallel energy into transverse. This expansion can lead to a significant reduction in beam current density. Electrons at the beam edge, which initially have considerable transverse energy, can in some cases lose all of their parallel energy and be lost from the channel.

Return current effects in plasma channels have been studied and several phenomena have been isolated. The temperature increase caused by ohmic dissipation has an important effect in reducing the reverse electric field with little penalty in channel radius. This electric field not only dissipates the beam energy but also causes spreading and some particle loss. These results suggest that other media, such as hydrogen, be studied which are more compatible with return current heating.

Beam Combination for Proto II

Beam overlap calculations have been carried out for the twelve channel experiment planned for Proto II. A wagonwheel configuration[21] with two axial return currents is planned. The computations were based on a single-particle model[23] in which the trajectories of sample particles are computed in the combined magnetic field of the channels and the current returns. Parameters used in the calculation were a channel current of 60 kA, a return current channel radius of 1 cm, $V_\perp/V_\parallel$ = 0.07, and an electron energy of 2 MeV.

Results for R_{min}, the radius of closest approach to the return current axis, are shown in Fig. 20; the left portion shows data for r_c = 0.5 cm while the right portion is for r_c = 0.3 cm. Electrons were injected at various radii and angles with respect to the return current axis, as shown schematically in the upper part of the figures. Also indicated is the overlap radius R_o = $r_c/\sin(\pi/N)$ for each case. The results are consistent with the $R_{min} \simeq R_o/4$ scaling reported earlier.[23] Twelve channels is near-optimal for the planar wagonwheel configuration, since $R_m \simeq r_c$.

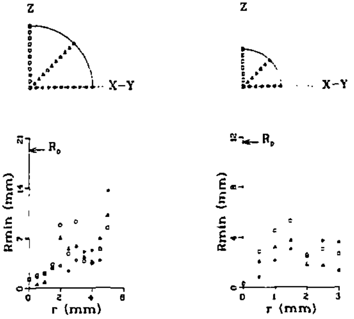

Fig. 20. Radius of closest approach to return current axis for twelve channel overlap calculation. Left-hand figure is for r_c = 0.5 cm, right-hand figure is for r_c = 0.3 cm.

Improved Radiation Transport Treatment for REB Channels

The hydrodynamic evolution of discharge-driven air plasma channels for REB propagation has been computed[21] using the CHART-P 1-D Lagrangian MHD code. This treatment used a single temperature diffusion approximation for the radiation thermal transport. Such a treatment would not be expected to work well in a plasma dominated by transport in spectral lines, to which the plasma is optically thin. Comparisons between experimental results and code calculations suggested[21] that the simple single temperature diffusion model was somewhat overestimating the energy loss.

A multigroup radiation transport scheme has been developed for use in CHART-B. The approach is based on a simple diffusion model. The required opacity data has been obtained from Science Applications, Inc. (SAI). The algorithm has been tested against the solution of the exact transport equation, published by Heaselet and Warming,[24] and also by Kesten,[25] for the case of a cylinder of uniform properties. The flux-limiting approach of Alme and Wilson[26] was tested in conjunction with this algorithm. As the tabulated results below show, in the steady-state test problem this approach introduced considerable error. Therefore, a simpler approach to flux limiting was used in which an iteration was performed if the flux exceeded the free-streaming limit.

Optical Pathlength (radial)	Surface Fluxes		
	Exact	Transport Code	Alme/Wilson Method
0.1	0.556	0.56	0.51
1.0	2.560	2.67	1.68
10.0	3.140	3.19	2.03

The transport package, as implemented, performs much better for moderate to large optical depths.

Preliminary results have been obtained on the channel formation problem using the SAI data in a five band model. The results are in reasonable agreement with the results previously obtained employing a phenomenological mean free path in a simple one-temperature model.

Hoop Stress in Electron-Beam Hybrid Reactor Chamber Walls

The hoop stress in the reactor chamber wall due to the reflected shock has been estimated using the analytic point source solution for a spherical blast wave[27] in air. A hypothetical pellet implosion of 3 MJ in, 75 MJ out was used in the study. Only the energy in x-rays and ions contributes to the growth of the blast wave. Of the 72 MJ released as a result of the DT reactions, 28.5% (20.5 MJ) is in the form of x-rays and ions, as determined from a neutron output spectrum[28] obtained from a Monte Carlo code, assuming a DT fuel density and gold shell density corresponding to ρr's typical of an electron-beam fusion target ($\rho r \sim 1$ g/cm^2 for DT, $\rho r \sim 8$ g/cm^2 for Au) and assuming that the neutrons were produced uniformly in the DT.

The accompanying figures show the peak value of the reflected overpressure as a function of the ambient air pressure P_o in the chamber for two values of E_o, the total energy in ions and x-rays. $E_o = 23.5$ MJ (Fig. 21) corresponds to the 3 MJ in, 75 MJ out pellet; $E_o = 40$ MJ (Fig. 22) corresponds roughly to a high-gain ion-beam target[6] calculated by A. V. Farnsworth with 1.25 MJ in, ~ 150 MJ out. For non-normal incidence to the wall, reflected overpressure would be less. The figures show results for ideal blast conditions for which the Rankine-Hugoniot equations apply. For non-ideal situations (e.g., thermal radiation from the implosion impinging on the wall, or particulate matter carried along by the blast wave), the peak value of the reflected overpressure does not exceed the incident overpressure by more than a factor of two; however, the decay of the overpressure is slower and the dynamic part of the overpressure is larger and can cause more damage compared to the ideal case.

The hoop stress in the chamber wall is given by

$$\sigma_H = (P_r + P_o - P_b)\frac{R_c}{2t} ,$$

where P_r is the reflected overpressure, P_o is the ambient air pressure, P_b is the air pressure outside the chamber wall, R_c is the chamber radius, and t is the wall thickness. We assume $P_b = 1$ atm. For the 3 MJ in, 75 MJ out pellet and $P_o = 1$ atm, the reflected overpressure for a 4 meter-radius chamber is about 3.25 atm. If this blast force is taken by a 1 mm steel wall, the hoop stress would be 96 ksi. The allowable wall stress for stainless steel is less than 15 ksi,[29] and the steel wall must be this thin for thermal stresses (which are linear with t) to be tolerable.[30] A carbon-composite liner about 0.5 cm thick therefore appears necessary to

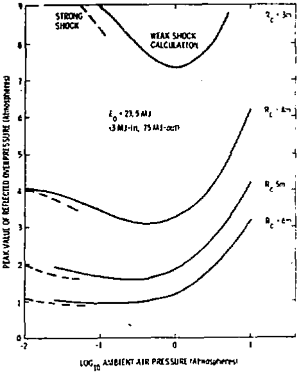

Fig. 21. Peak value of the reflected overpressure as a function of chamber radius and ambient air pressure in the chamber for an implosion with 23.5 MJ in x-rays and ions. Ideal *blast wave conditions are assumed.*

keep the wall stress within tolerable limits. The hoop stress in a liner of this thickness would be about 20 ksi for the 3.25 atm reflected overpressure. A carbon-composite has good fatigue properties and its tensile strength is 100-200 ksi, so 20 ksi should be reasonable.

Figure 23 shows the variation in hoop stress with chamber radius and fill pressure for the hypothetical pellet if a 0.5 cm liner is used. A 4-meter radius chamber should be adequate. For the 1.25 MJ in, 150 MJ out pellet, the reflected overpressures of Fig. 22 and the thermal stress limits require a chamber radius of at least 5 meters.

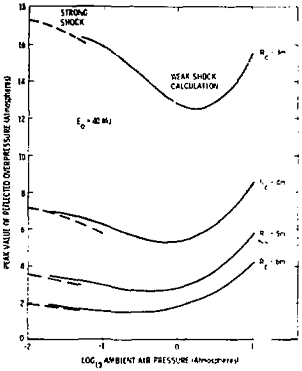

Fig. 22. Peak value of the reflected overpressure as a function of chamber radius and ambient air pressure in the chamber if 40 MJ are in x-rays and ions. Ideal blast wave condi*tions are assumed.*

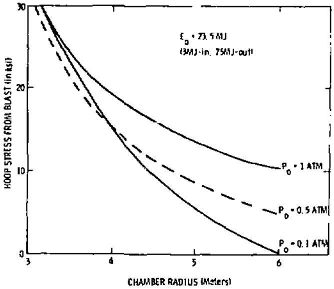

Fig. 23. Hoop stress in a 0.5 cm-thick liner as a function of chamber radius and fill pressure, assuming ideal blast wave conditions.

Estimate of Equilibrium Gas Temperature with Repetitive Operation

Estimates have been made of the equilibrium gas temperature in the chamber of the e-beam hybrid reactor, in order to determine how often the gas in the chamber needs to be replaced. The gas must be replaced at a rate such that the characteristics of the gas are acceptable for channel initiation and beam propagation. It was hoped that, because of rapid radiation to the chamber wall, the rate of gas removal would be determined by the amount of debris tolerable rather than by the gas temperature.

The heat transport from the chamber gas--air was assumed--to the first wall of the reactor has been obtained for a rep rate of 10 Hz. In each hypothetical shot 3 MJ is deposited in the gold shell of a DT-filled target and 72 MJ is produced; this corresponds to a total of about 23.5 MJ in x-rays and debris.[31] A 0.1 cm stainless-steel first wall with a 0.5 cm graphite liner at 4-meters radius was chosen to minimize dynamic and thermal stresses due to the blast force.[31]

All materials were assumed to be at 750 K at *the start of the calculation, since for* efficient extraction of heat energy from the system, the steel layer--which has a circulating lithium cooling channel outside of it--should have a temperature of 700 to 800 K. The CHART-D[32] radiation-hydrodynamics code, with the hydrodynamics turned off, was employed. The conductivities of 304 stainless and ATJ graphite (parallel to the grain) were used to model the reactor wall.

Except for the opacity, the properties of the air in the reactor chamber were modelled using the Lockheed[33] tables. At low temperatures on CHART-D the Lockheed tables give mean free paths which are too large; we have therefore used the Russian tables of Avilova, et al.,[34] which have been incorporated into a version of CHART-D.[35] At temperatures below about 4000 K, the contribution due to the thermal condictivity of air[36] has been included.

Because CHART-D is a one-temperature code, some difficulties can result. Comparison calculations with a three-temperature code indicate that temperature equilibrium occurs within 0.001-0.01 ms after a shot for chamber fill pressures of 20 torr to 1 atm. The CHART-D calculations with no hydrodynamics *represent a lower bound on the rate of radiation* to the first wall; the position of the radiation front in air is 10 to 40 percent lower after one shot than obtained in the three-temperature hydracode calculations, which included hydrodynamics and used a less accurate equation of state for air at applicable temperatures.

In general, the conclusion from the codes is that air at a pressure of 50 torr or less at 750 K is necessary in order for any transport to occur to the wall in 100 ms. Transport to the wall is quite sensitive to the air temperature, so a smaller gas mass decreases the radiation time to the wall. (However, pressures below about 100 torr are undesirable because of the more rapid expansion of the plasma channels.) At 20 torr after 5 shots, the air temperature in the CHART-D calculation has reached an equilibrium value of 6180 K and the mean degree of ionization is about 0.0001. At 50 torr, 10 shots are required to reach the equilibrium temperature of the air, 7080 K, and the mean degree of ionization is 0.0005. At 100 torr, the equilibrium temperature of 7660 K is reached in 23 shots and the mean degree of ionization is about 0.0015.

According to P. Miller,[38] the temperature and degree of ionization at 50 to 100 torr could *probably be considered marginal. If the air* must be completely un-ionized for channel formation, it becomes necessary to replace the gas after every shot. D. Cook[39] has investigated the pumping power required to do this and he concludes that such replacement *may be possible.*

DIODE PHYSICS AND POWER FLOW THEORY

Theory of Double Sheaths in Plasmas

The formation and behavior of double sheaths (non-neutral layers) in electrically-stressed plasmas is of practical importance for a number of reasons. These structures may be important in the process of electron emission from cathode plasmas of REB diodes, for example. They also presumably play a role in the behavior of plasma-filled diodes. In addition, it is believed that the fast opening plasma switch (FOSIL) experiments depend for their action on the dynamics of double sheaths in the plasma. A number of theoretical investigations have been undertaken to better understand this phenomenon.

1. Force Balance and Double Sheath Motion. Previously,[40] it had been shown that if a specific model of the plasma/sheath/beam system was chosen, then the total force operating on a space charge limited sheath was zero. This result has now been shown to be valid for a much broader class of models. The two assumptions required are (a) the plasma is collisionless, and (b) the sheath is "rigid," which is to say that the only degree of freedom we allow the non-neutral region is to be translated as a whole in the direction of the electric field. The justification of these assumptions is discussed in Ref. 41. The essential result is that the force accelerating the sheath is

$$F = \frac{\varepsilon_0}{2} \left[E^2(\ell) - E^2(0)\right] \qquad (7)$$

where $E(\ell)$ is the electric field at the anode sheath boundary and $E(0)$ is the field at the cathode sheath boundary. The conclusion is that if these assumptions apply to real experimental conditions, then in the cases where the sheath is stationary, processes occur which generate a restoring force, through Eq. (7), on sheath displacements. Conversely, in the cases where sheath motion is observed (e.g., high voltage discharges as in Ref. 42) it is not correct to look for mechanisms (e.g., plasma heating) which create a pressure difference, but we should rather investigate processes (beam slowing, finite resistivity) which result in electric field differences on the two sides of the plasma.

2. Sheath Initiation. The formation and growth of a double sheath and the concurrent rapid impedance rise are being studied in the FOSIL[43] series of experiments for the possibility of the development of a high current, fast-opening switch, which would be of great importance for inductive energy storage applications. One persistent problem in the experiments is that there is a transition period to the fast switching mode during which the impedance rises too slowly. This effect has tentatively been identified with a plasma state (observed in computer simulations[44] in which a number of small sheath-like structures are coalescing into a single well-defined sheath. It is hoped that it might be possible to eliminate or suppress this phase by introducing a mechanism to ensure that all of the sheath nucleation takes place in the same plane. Passive mechanisms (preparing the plasma in some way before the voltage pulse for example with a grid-generated initial sheath) are not promising because for useful switching the current before the switch opening must exceed the critical current for sheath maintenance[41] by a factor of at least 5 or 6. Therefore, what is needed is a triggered mode in which a planar disturbance in the plasma temperature or density is created on a short time scale after the current has risen. Several ideas have been considered, including heating or ionizing by means of a collimated high energy electron or ion beam. These suggestions appear feasible in principle, but rather difficult experimentally. The use of lasers for the same purpose has been rejected because for the plasma densities now being considered, the appropriate wavelength is in the millimeter or longer range, and generation and collimation of such a beam is not presently possible. One idea being studied (in conjunction with J. P. VanDevender) is to use a pulsed magnetic field to propagate a density disturbance into the plasma. The crucial (as yet unanswered) question is whether, because of the transverse electric field, the disturbance can propagate at a velocity significantly higher than the ion acoustic speed, and thus facilitate fast switching.

3. Theoretical Model of Plasma Switch. A simple model of the opening double sheath (similar to that considered in Ref. 45) is being studied computationally which includes the inductive nature of the voltage drop when the fast opening switch is connected with an inductive energy store. Figure 24 shows the time dependence of the voltage current and power for a case with parameters chosen to be of interest for an EBFA-I-like accelerator. Probably more important (and reliable) than the quantitative predictions are the scaling laws which have been obtained from this model. It has been found that V/kT and I/I_o as functions of $\omega_{p}t$ are insensitive to transformations which keep

$$L\,An^{3/2} = C_1$$

$$I_o/An = C_2$$

$$A^{3/2}n = C_3$$

where C_1, C_2, and C_3 are constants, L is the inductance in series with the switch, A is electrode area, I_o is the initial current at switching, and n is the plasma density.

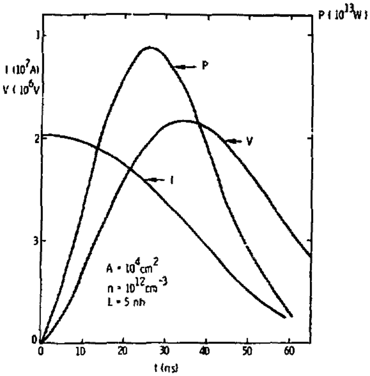

Fig. 24. Power, voltage, and current vs. time from the plasma switch/inductive storage simulation. Parameters are chosen to give output parameters similar to EBFA-I.

Another important result of the simulation is that the transition phase ("Phase 2") discussed in subsection 2 above, in which the voltage rises much more slowly than in the switching phase, cannot be explained by simple sheath opening, whereas the fast switching phase is in good agreement with the simulations if a plasma density of about 10^{11} cm^{-3} is chosen. This is within the rather broad experimentally measured range of plasma density. More experiments in the FOSIL series are being planned which will provide the opportunity to test the model more vigorously.

2-D Electromagnetic Particle Code Results for Coax Propagation

The time-dependent particle code described in Refs. 46 and 47 has been used in support of a number of experimental investigations. One important application was to compare with the results of experiments at Physics International on long coaxial magnetically insulated vacuum transmission lines. The experiments were directed by M. Di Capua, under contract with Sandia. This was an unusually good opportunity to compare experiment with simulation because (a) the geometry is coaxial, as assumed in the code, and (b) there are current monitors on both the inner and outer electrodes at three intermediate positions along the 10 m line, as well as at the input and output. This gives greater confidence that the measurements at intermediate positions are characteristic of the line itself rather than of the input or output transition regions. The input to the code was the measured input voltage waveform. Thus all the current waveforms were available for comparison of theory with experiment, although in practice we can only follow the pulse up to the time at which the first reflection from the load occurs.

It was found that the total current measurements I_T were in very good agreement with the simulation results for I_T at each of the three intermediate monitors (see Fig. 25). The error bars on the simulation results represent the standard deviation of a number of time steps (typically 20 to 30) between the plotted points. The peak voltage at the first monitor was somewhat higher (15%) than predicted, but the arrival time and other features agreed well. For the other two monitors, the agreement in I_T was extremely good for all times. On the other hand, the boundary current monitors (I_B) consistently measured less current (20%) flowing within the cathode radius than predicted by the code. It is speculated that at least two mechanisms exist which would cause these monitors (Rogowski coils) to read low. The overall conclusion is that these experiments indicate that the new code is an accurate predictive tool which warrants further development and use.

Another application was to run the coax code for pulse propagation into a dead short for times longer than the transit time, and to study the reflected wave. The following parameters were used: $r_a = 8$ cm, $r_c = 7$ cm, 4 ns rise to V = 2.4 MV, L = 3 m. In a test case without electrons, the expected doubling of the current was found:

$$\frac{I_{pT}}{I_{rT}} = 2.0 \pm 0.06$$

where I_{pT} is the peak current at the short and I_{rT} is the running current in the line before the first reflected wave. When electrons were added, the code gave

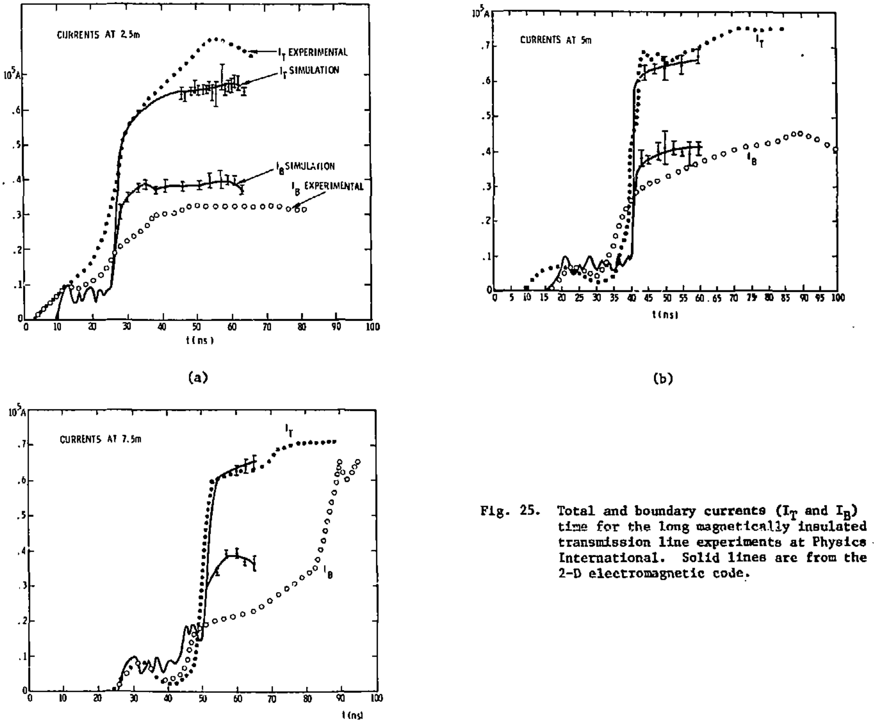

(a)

(b)

(c)

Fig. 25. Total and boundary currents (I_T and I_B) time for the long magnetically insulated transmission line experiments at Physics International. Solid lines are from the 2-D electromagnetic code.

$$\frac{I_{pT}}{I_{rT}} = 1.69 \pm 0.15$$

This is in agreement with a formula proposed by VanDevender[48] based on a simple model and considerations of energy balance: $I_{pT}/I_{rT} = 2(Z/Z_0)^{1/2}$, which gives 1.6.

A simple circuit model was incorporated into the code to take into account the resistance R and inductance L between the generator and the coax line. Code runs were made for MITE type parameters with and without this circuit equation. With the circuit included, the voltage and currents of course are smaller, and the pulse front moves slower. The Z/Z value was nearly the same (0.7) in both cases, and the usual picture[46] of current leakage only at the pulse front still holds. This addition to the code is more of a convenience than a fundamental research tool; it merely makes it unnecessary to know the voltage vs. time at the input end of the coax (provided the generator output is known).

Another application pursued with the electromagnetic code was the "reversed polarity" question. In all previous runs, the inner cylinder has been the cathode, with electrons flowing radially outward. One of these previous cases was repeated, but with the outer cylinder as the cathode. The motivation for this study was the experimental observation that the power transport efficiency is less when the outer cylinder is the cathode. However, the code result shows no basic difference in the pulse propagation picture[46] for this case than when the polarity is reversed. We conclude that either something is missing from our model, or that the experiments had different pulse injection conditions in the two cases.

DIODE CODE DEVELOPMENT AND APPLICATION

Diode Code Development

The Sandia diode simulation code has been used to investigate electron and ion behavior in a wide range of applications.[49-51] In the past, minor changes to the diode configuration (such as changing the anode-cathode gap or cathode radius) have been simulated with very little coding required by the user. As the diodes under consideration become more complex, however, more detailed rewriting of the code becomes necessary for each new configuration to be considered.[52] (Examples of the more complex diodes being considered are presented later in the sections discussing the Proto I ion diode and the C-diode.) In an attempt to reduce this required rewriting an effort has begun to make the diode simulation code more easily adaptable to major changes in diode configuration.

The most time-consuming change to the diode code in the past has been the addition of new surfaces. The Child's law emission routine[51] which has been used almost exclusively, requires the definition of several quantities (such as return current, average magnetic field, charge density) for each emitting surface. As each new surface is added, these quantities must be redefined. The problem of making a Child's law emission routine which would be valid for a general surface is formidable. An emission routine which uses Gauss' law,[53,54] on the other hand, requires much less information (namely, the total charge in the cells off the emitting surface, and the electric field one zone off the surface) and is readily adaptable to a general surface. A general emission routine has been written which uses Gauss' law and has been tested and found to agree with previous results obtained with the Child's law method and with analytic results.[52] The subroutine is exceedingly simple to use since it requires as input only the surface location and extent, whether ions or electrons are to be emitted, and the charge and electric field information one zone off the surface.

Particle testing is another section of the diode code which can change appreciably when the diode surfaces are changed. After a particle has been advanced one time step, a test must be performed to indicate whether that particle has crossed an absorbing surface (in which case it must be removed from the system), reflected from the symmetry axis, or remain in the diode to be advanced again during the next time step. As new surfaces are added, new tests must also be added resulting in more code revision. A subroutine has been written which takes the general surface information and performs the required particle tests.

Other improvements have been added to the code which make it more radily adaptable to varying surface descriptions. Further changes are now under way which will hopefully result in a diode code which can treat a wide range of diode configurations with minimal user revision.

Combined Diode - Monte Carlo Code for Enhanced Deposition

In order to investigate the effects on diode behavior of electron scattering and deposition in the anode material, a collisional Monte Carlo model has been added to the PIC diode code. The Monte Carlo model has been described in detail elsewhere.[55] Electron energy loss is accounted for in the continuous-slowing-down approximate ion and multiple elastic scattering is described using the theory of Goudsmit and Saunderson.[56] The combined code allows the computation of current flow and electron deposition in diodes, accounting self-consistently for electron-material interactions. A variety of materials[57] of arbitrary density can be selected and magnetic field effects within materials can be studied.

As a first application of this code, a Hydra type diode (cathode outer radius = 3.8 cm, cathode inner radius = 1.6 cm, v = 800 kV, I = 300 kA) was simulated with various anode materials. The cases considered were a perfectly absorbing anode, and solid density anodes of carbon, copper, and gold. In all cases the diode geometry and voltage were held fixed. The results indicated variations in pinch parameters depending upon the respective material, however, in all cases the FWHM of the pinch was calculated to be less than 2 mm. This pinch size is considerably smaller than the typical 3 to 5 mm FWHM which is observed experimentally. The conclusion is that backscatter alone is not sufficient to substantially broaden the pinch. Next a 1.5 mm thick, r-independent, low-density blow-off was added as the front layer of a copper anode, the remainder of which was solid density. The cathode to blow-off gap was the same as the previous cathode to anode gap to hold the diode current fixed. The pinch FWHM was seen to increase over the solid density anode cases but was still less than the experimentally observed pinch.

Finally, an r-independent anode blow-off was assumed with a 2 mm axial by 2 mm radial region added to the previous case on axis. An electron particle map for this case is shown in Fig. 26. This was to approximate the additional blow-off resulting from deposition in the pinch region. In this case, the observed pinch FWHM was found to be in reasonable agreement with experiment, as was the deposition in the outermost blow-off of ~ 2 TW/gm. The pinch broadening results from side scattering and/or reduced pinching forces in the low density material. We speculate that this large blow-off extent might result from a tight pinch at early time or as A. J. Toepfer suggests from enhanced deposition in the outer portion of the blow-off. There is some prior holographic data to support this hypothesis. Theoretical and experimental investigation into this effect is continuing.

Fig. 26. Electron particle map from combined diode-Monte Carlo code for r-independent blow-off region.

Ion Diode Simulations

This work was motivated by Sandia's program to produce high current geometrically focused ion beams from magnetically insulated diodes.[58] Parameter studies using the diode code were done appropriate to two machines, HERMES II and Proto I. Emphasis of the calculations was on electron loss, ion production, and ion beam transverse velocity spread.

An ion particle map for HERMES-like parameters is shown in Fig. 27. The configuration is not exactly like the HERMES experiment in that we have used vanishing normal derivative boundary conditions on the left and right side of the mesh. The field coils (not shown) are located at R = 15.25 cm, Z = ± 7.60 cm and create a magnetic field as shown in Fig. 28. The ion current of 60 kA agrees well with the Child's Law value. The potential on the anode A was 5 MV, but the potential along the top right side of Fig. 27 was held at 1.1 MV to take account of the fact that the outer radius in the experiment was 76 cm. Electrons remained near the cathode K; there was no appreciable electron current in the simulation. The insulation is due mainly to the B_z ($\approx$ 14 kG in gap) rather than the smaller B_θ. This was checked by running the same case but with a smaller area for ion emission. This result of no electron loss is contrary to the experimental finding of an anomalous 140 kA electron leakage. This discrepancy might be due to plasma motion or breakdown in the system, but is more likely caused by the fact that our simulation does not take into account the open-ended HERMES geometry, since we have assumed symmetry across the left boundary and have not calculated the behavior in the region near the end of the cathode, where the applied $\vec{B}$ becomes parallel to $\vec{E}$. (See Fig. 27a of Ref. 58.) The calculation is more relevant to a dual current feed diode (Fig. 27c of Ref. 58) and the optimistic result of the simulations suggests the value of trying such a configuration in practice.

The Proto I ion diode simulations were done for the configuration shown in Fig. 29. The $\vec{B}$ field contours produced by the pulsed coil are included in this figure. The system is symmetric about the z = 0 plane. The simulation geometry is different from that of the experiment in that the blade cathodes are actually at an angle with respect to the r direction and the anode surface is concave to increase focusing of the ion beam.

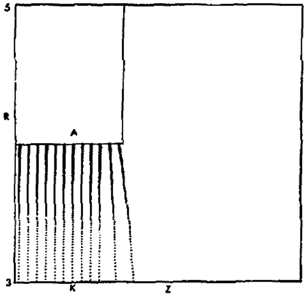

Fig. 27. Ions in HERMES diode run. V = 5 MV, radial gap 1" (r-scale in inches).

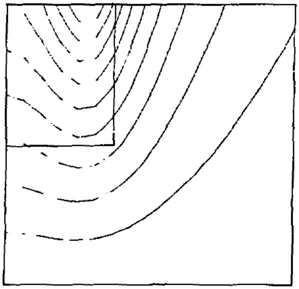

Fig. 28. Applied $\vec{B}$ in HERMES run of Fig. 27.

The first series of simulations was done to investigate the effects of space charge on the ion beam in the region between the virtual cathode (found along the field line which passes through the blade tip) and the drift region. These simulations were all done with a coil current of 360 kA and a diode voltage of 2 MV. In all cases, the applied magnetic field prevented any electron current leakage to the anode. It became evident after several simulations that, when averaged over several time steps, the electrons emitted from the blade cathode shank did a very good job of neutralizing the ion space charge in this region. At any particular time, however, large voltage peaks in this region comparable to the diode voltage occurred because of numerical difficulties associated with the small number of simulations particles

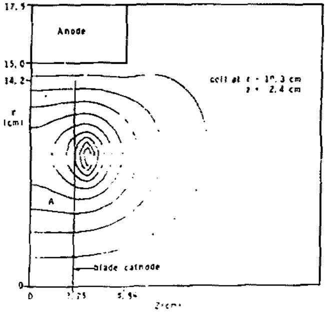

Fig. 29. Proto I ion diode configuration.

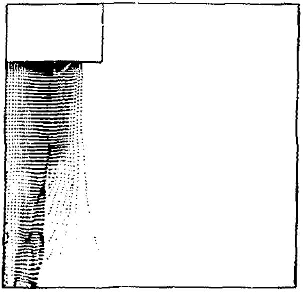

Fig. 30. Ion simulation particle map for Proto I ion diode.

available. Using as justification the fact that the neutralization was very good on average, complete space charge neutralization was assumed in this region for all subsequent runs.

The results for the case of 360 kA coil current were a total ion current of 100 kA per side of which 70 percent arrived at the drift region. The remaining 30 kA ion current was collected by the blade cathode. Figure 30 is an ion particle map of this case. It is interesting to note that even with complete space charge neutralization in region A, the ion beam develops some divergence because of bending in the B field produced by the ion return current. Figure 31 is an electron particle map of this same case. The strong virtual cathode seen in this figure produces a fairly well collimated ion beam. There is some experimental evidence that this strong virtual cathode predicted by the simulation does indeed exist.

A lower value of coil current (more in line with experimental values) was next simulated. With a coil current of 160 kA, the ion current becomes 140 kA per side of which again 70 percent reaches the drift region. Because of the lower value of insulating magnetic field there is some electron current loss for this configuration (approximately 10 kA per side). The lower magnetic field allows the virtual cathode to move closer to the anode and the result is the higher ion current.

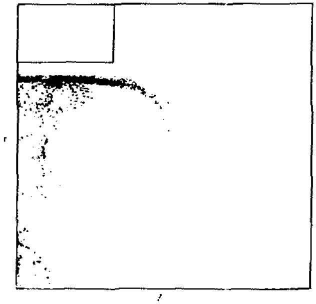

Fig. 31. Electron simulation particle map for Proto I ion diode.

The simulation which have been done to date are encouraging in that they confirm the existence of a virtual cathode, there is very little electron current leakage and substantial ion currents are predicted. The ion beam divergence caused by bending in the magnetic field produced by the return current is worrisome and possible methods for reducing this divergence are being considered.

C-Diode Studies

Computer simulations have been done for the C-diode concept recently studied experimentally by J. Cheng. In this diode configuration a target is placed on axis inside the cathode inner radius. An electron current flows radially from the cathode inner shank to the target. The purpose of a simulation of this diode arrangement is to investigate the current flow pattern and to estimate the percentage of the total electron current which is collected by the target.

An electron particle map for the C-diode configuration used on Proto I is shown in Fig. 32. In this figure, R_O = 1.32 cm, R_i = 6 mm, R_T = 2.25 mm, d = 2.9 mm, and t = 4.3 mm. The diode voltage is 1.3 MV and the resulting total current is 200 kA. The result of this simulation is that 65 percent of the total electron current is collected by the target. This result is in good agreement with the experimentally observed current split between target and anode. The electron current which impinges on the anode (A) is distributed such that 50 percent is collected within a radius of 3.75 mm about the axis.

In the simulation described above, ions are emitted from all target surfaces, the stalk on axis, and the anode face out to R_o. In order to investigate the extent to which ion flow is important in the C-diode, the same simulation was repeated but with no ions in the diode. The simulation yields the result that less than 20 percent of the electron current hits the target when ions are not present. The ions thus play an important role in the operation of the C-diode. Their effect is twofold. The ion density near the cathode increases the electron emission and hence current and the distributed ion current produces a B field more favorable to beam pinching into the target region. This distributed ion current has been shown to be an important factor in pinching electron beams in diodes before,[51] and this is yet another demonstration of this effect.

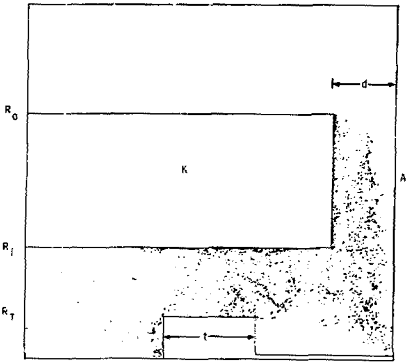

Fig. 32. Electron particle map of Proto I C-diode simulation.

PARTICLE BEAM SOURCE DEVELOPMENT AND THEORY

Collective Acceleration Book

An in-depth study of the status of collective ion acceleration with linear electron beams was made, in preparation of a book on this research area. Topics examined included:

1. Collective acceleration mechanisms including net space charge mechanisms, inductive mechanisms, inverse coherent drag mechanisms, linear waves and instabilities, nonlinear waves and solitons, stochastic acceleration and impact acceleration.

2. Naturally-occurring collective ion acceleration processes, including intense electron beam injection into neutral gas, collective acceleration in modified geometries (dielectric tubes, cusp B_z, wall discontinuities, vacuum injection), and collective acceleration in IREB diodes. An exhaustive investigation of the IREB/gas case was performed, including analysis of experiments from seven laboratories, thirteen theories, and four simulation studies. Special emphasis was placed on the effects of B_z, beam impedance, power balance, γ, ν/γ, and multiple pulses. With extensive comparisons, it was shown that the original Olson theory[59,60] is able to account for the data, much of which was acquired subsequent to the formulation of this theory.

3. A catalogue summary of 36 collective ion accelerator concepts was prepared that includes net space charge accelerators, envelope motion accelerators, drag accelerators, linear wave accelerators, nonlinear wave accelerators, and accelerators that use collective fields only for focusing.

4. Scalable collective accelerators (IFA, ARA, CGA) were examined in depth. Theory status of feasibility experiments, and scaling laws were investigated. New scaling results were obtained concerning peak ion energies, peak ion powers, efficiencies, control accuracy criteria, and relativistic expressions for the acceleration lengths and times.

The results of these studies will appear in the first book to be written on collective ion acceleration, which includes "Collective Ion Acceleration with Linear Electron Beams" by C. L. Olson and "Collective Ion Acceleration with Electron Rings" by U. Schumacher (Max Planck Institut for Plasma Physik, Garching). This book is to be published by Springer-Verlag as a volume in the series Tracts in Modern Physics (edited by G. Hohler).

IFA Feasibility Experiments

An experimental program is in progress to demonstrate feasibility of the Ionization Front Accelerator (IFA).[61,62] In the IFA, a controlled, moving, ionization front is created by lasers using two-step photoionization of a special working gas (Cs). The IREB head follows this front synchronously, creating there a moving potential well which is to be used for trapping and accelerating ions. It has already been demonstrated that Cs is a feasible working gas, that the required transparent/conducting drift tube exists, and that an accurately-programmed laser sweep can be made (see previous semiannual reports). A scintillator/streak camera diagnostic has also been developed that accurately shows beam front motion with subnanosecond resolution.

The first system shots were characterized by excessive jitter, so special studies were made to minimize the delay and jitter of the various system components (lasers, fast shutter, IREB, streak camera). Screen boxes were constructed for the Pockel cell drivers, which did eliminate gross pretriggering problems for the lasers. The ruby oscillator rail in the dye laser was rebuilt to minimize the cavity buildup time. Considerable experimentation was done on various HV pulse circuits to perfect the Pockel cell drivers. From these studies, a working knowledge has been gained of many of the subtle causes of jitter; we believe we are now able to minimize jitter to acceptably low levels.

A magnetic ion spectrometer with cellulose nitrate (CLN) detectors was added to the system. Detection of energetic protons on CLN was confirmed using a known proton source. Ion spectra may now be obtained on every shot.

The entire system with beam front and ion diagnostics is therefore now operational. A systematic study of the IFA and related collective ion acceleration phenomena (IREB into vacuum, IREB into air, IREB into Cs) has thus been initiated.

This program is jointly sponsored by DOE (NP) and AFOSR.

Neutralization of Ion Beams in Magnetic Fields

A crucial problem in pulsed linear ion accelerators such as PULSELAC is the time-dependent space-charge neutralization of the ion beam by electrons from the walls.[63] Using particle simulation (one space dimension, three velocity components) and analytic estimates, we have studied this problem for the situation where a magnetic field is applied at an arbitrary angle as in Fig. 33. Here an ion beam moves in the z direction; for densities of interest it would blow up in a very short distance except for the electrons which are pulsed into the ion cloud by the space charge potential. If these electrons were constrained to follow B lines which are exactly transverse to the walls ($\alpha = 0$) or if there were no $\vec{B}$ at all, the neutralization process can be shown to be less than complete, even in the final steady state.[64] The time development of the maximum potential for this case is shown by curve (a) of Fig. 34. However, $\vec{B}$ lines which are not normal to the walls ($\alpha \neq 0$) allows the electrons to gain a velocity component parallel to the walls, and this leads to much better neutralization. The potential for such a case ($B = 2$ kG, $\alpha = 14°$) is shown by curve (b) of Fig. 34. Here, a $\phi(0)$ which remained at zero would correspond to perfect neutralization. An analytic estimate gives as an upper limit

$$\phi(0) \sim d^2\, n_{i_o}^{.67}/\Delta t_r^{.67}$$

where 2d is the drift tube width, n_{i_o} is the maximum ion density, and Δt_r is the beam risetime. The code results agree with this scaling.

In general, the conclusion from this work is that for typical ion beam parameters with $\alpha \neq 0$, and in regions where electrons cannot travel longitudinally with the ions, neutralization can occur on nanosecond time scales and the analytic formula above provides an upper limit to the space charge potential. This is encouraging for linear accelerator applications ($n_{i_o} = 10^{11}$ cm^{-3}, $\Delta t_r = 10$ ns), and indicates that neutralization should be effective during the entire time of passage of the ion beam.

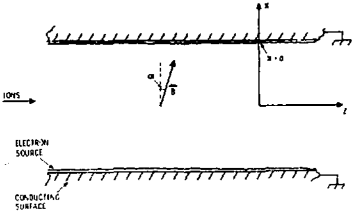

Fig. 33. Schematic of ion beam transverse neutralization problem.

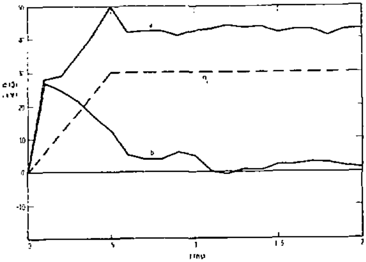

Fig. 34. Potential $\phi(x = 0)$ at center of drift section vs. time for cases (a) $B = 0$ (or $\alpha = 0$), (b) $B = 2.06$ kG at $\alpha = 14°$. Only average curves are shown; the actual curves would have small oscillations superimposed (amplitude of a few kV, period $2\pi/\omega_p \approx 0.1$ ns). The ion density is indicated by the dashed line.

REFERENCES:

1. J. Chang, M. M. Widner, A. V. Farnsworth, Jr., R. J. Leeper, T. S. Prevender, L. Baker, and J. N. Olsen, Proc. of 2nd International Topical Conf. on High Power Electron and Ion Beam Res. and Tech., Cornell University, Ithaca, NY, V. 1, p. 195 (1977).
2. D. J. Meeker, J. H. Nuckolls, and R. O. Bangerter, Bull. Am. Phys. Soc. 20, 1352 (1975).
3. J. Chang, M. M. Widner, G. W. Kuswa, and G. Yonas, Phys. Rev. Lett. 34, 1266 (1975).
4. For example, see P. A. Miller, Phys. Rev. Lett. 39, 92 (1977).
5. J. Chang, M. M. Widner, A. V. Farnsworth, Jr., R. J. Leeper, L. Baker, and J. N. Olsen, Proc. of 2nd International Topical Conf. on High Power Electron and Ion Beam Res. and Tech., Cornell University, Ithaca, NY, October 1977.
6. A. V. Farnsworth, Jr., M. M. Widner, J. Chang, R. J. Leeper, L. Baker, and J. N. Olsen, Topical Meeting on Inertial Confinement Fusion, San Diego, CA, February 1978.
7. R. O. Bangerter and D. J. Meeker, Proc. of 2nd International Topical Conf. on High Power Electron and Ion Beam Res. and Tech., Cornell University, Ithaca, NY, October 1977.
8. Private communication, M. M. Widner and A. J. Toepfer, February 1975; M. M. Widner and A. V. Farnsworth, Jr., December 1975; A. V. Farnsworth, Jr. and M. M. Widner, March 1976; A. V. Farnsworth, Jr., M. M. Widner, and J. Chang, November 1976.
9. J. H. Nuckolls, R. O. Bangerter, J. D. Lindl, W. C. Mead, European Conference on Laser Interaction with Matter, Oxford, September 1977.
10. R. O. Bangerter and D. J. Meeker, Proc. of 2nd International Topical Conf. on High Power Electron and Ion Beam Res. and Tech., Cornell University, Ithaca, NY, October 1977.
11. M. A. Sweeney and M. J. Clauser, Electron Beam Fusion Progress Report - April-September 1977, SAND78-0080, Sandia Laboratories, Albuquerque, NM (April 1978).
12. F. Winterberg, Nature 251, 44 (1974).
13. ERDA Summer Study of Heavy Ions for Inertial Fusion, ed. by R. O. Bangerter, W. B. Hermannsfeldt, D. L. Judd, and L. Smith, Lawrence Berkeley Laboratory Report No. LBL-5543 (1976).
14. S. Humphries, Jr., J. Appl. Phys. 49, 501 (1978).
15. M. J. Clauser, Phys. Rev. Lett. 35, 848 (1975).
16. M. J. Clauser, private communication.
17. M. J. Clauser, in ERDA Summer Study of Heavy Ions for Inertial Fusion, ed. by R. O. Bangerter, W. B. Hermannsfeldt, D. L. Judd, and L. Smith, Lawrence Berkeley Laboratory Report No. LBL-5543, p. 39 (1976).
18. L. Baker, J. R. Freeman, and M. M. Widner, Electron Beam Fusion Progress Report - April-September 1977, SAND78-0080, Sandia Laboratories, Albuquerque, NM (April 1978).
19. J. Olsen, et al., this semiannual.
20. L. P. Mix, F. C. Perry, A. J. Toepfer, and M. M. Widner, Bull. Am. Phys. Soc. 23, No. 1, 96 (1978).

21. P. Miller, L. Baker, J. R. Freeman, L. P. Mix, J. W. Poukey, and T. P. Wright, Proc. of 2nd International Topical Conf. on High Power Electron and Ion Beam Res. and Tech., Cornell University, Ithaca, NY, October 1977.

22. S. A. Goldstein, D. P. Bacon, D. Mosher, and G. Cooperstein, Proc. of 2nd International Topical Conf. on High Power Electron and Ion Beam Res. and Tech., Cornell University, Ithaca, NY, October 1977.

23. T. P. Wright, to be published in J. Appl. Phys., 1978.

24. M. A. Heaselet and R. A. Warming, J. Quant. Spec. Rad. Transfer 6, 751 (1966).

25. A. S. Kesten, J. Quant. Spect. Rad. Transfer 8, 419 (1968).

26. M. L. Alme and J. R. Wilson, App. J. 186, 1015 (1973).

27. M. A. Sweeney and M. M. Widner, Electron Beam Fusion Progress Report - April-September 1977, SAND78-0080, Sandia Laboratories, Albuquerque, NM (April 1978).

28. R. J. Leeper, private communication.

29. Bill Allen, Bechtel Corporation, private communication.

30. D. Cook, private communication.

31. M. A. Sweeney, this semiannual.

32. S. L. Thompson, Improvements in the CHART-D Energy Flow--Hydrodynamic Code V: 1972/1973 Modifications, SLA-73-0477, Sandia Laboratories, Albuquerque, NM (October 1973).

33. R. K. M. Landshoff and J. L. Magee, Thermal Radiation Phenomena, V. 1 (New York: Plenum Press, 1969).

34. J. V. Avilova, L. M. Bibeman, V. S. Vorob'eva, V. M. Zamalin, G. A. Gobzev, A. N. Lagar'kov, A. Kh. Muatschakanyah, and G. E. Norman, Optical Properties of Hot Air (Moscow: Nauka, 1970).

35. L. Baker, "The Radiative Opacity of Air: Comparison of Selected Russian and American Work," RS 5241/202, Sandia Laboratories, Albuquerque, NM, Internal Memorandum (September 1977).

36. Y. S. Touloukian, P. E. Liley, and S. C. Saxena, Thermophysical Properties of Matter (New York: Plenum Press, 1970), 3, 512.

37. Reference deleted.

38. P. Miller, private communication.

39. D. Cook, private communication.

40. K. D. Bergeron and T. P. Wright, Bull. Am. Phys. Soc. 22, 1062 (1977).

41. K. D. Bergeron and T. P. Wright, "Force Balance and Density Criteria for Double Sheaths in Plasma," submitted to Phys. Fluids.

42. E. I. Lutsenko, N. D. Sereda, and L. M. Kontsevoi, Sov. J. Plasma Phys. 2, 39 (1976).

43. J. P. VanDevender, *Electron Beam Fusion Progress Report - July-September 1976*, SAND76-0711, Sandia Laboratories, Albuquerque, NM (May 1977).

44. J. S. DeGroot, C. Barnes, A. E. Walstead, and O. Buneman, Phys. Rev. Lett. 38, 1283 (1977).

45. M. M. Widner and J. W. Poukey, Phys. Fluids, 19, 1838 (1976).

46. J. W. Poukey and K. D. Bergeron, Appl. Phys. Lett. 32, 8 (1978).

47. J. W. Poukey and K. D. Bergeron, *Electron Beam Fusion Progress Report - April-September 1977*, SAND78-0080, Sandia Laboratories, Albuquerque, NM (April 1978).

48. J. P. VanDevender, private communication.

49. J. W. Poukey, J. R. Freeman, and G. Yonas, J. Vac. Sci. Tech. 10, 954 (1973).

50. M. J. Clauser, L. P. Mix, J. W. Poukey, J. P. Quintenz, and A. J. Toepfer, Phys. Rev. Lett. 38, 398 (1977).

51. J. P. Quintenz and J. W. Poukey, J. Appl. Phys. 48, 2287 (1977).

52. J. W. Poukey, J. Vac. Sci, Tech. 12, 1214 (1975).

53. R. Lee and Shyke A. Goldstein, private communication.

54. J. P. Quintenz, to be published.

55. M. M. Widner, J. W. Poukey, and J. A. Halbleib, Sr., Phys. Rev. Lett. 38, 548 (1977).

56. S. Goudsmit and J. L. Saunderson, Phys. Rev. 57, 24 (1940).

57. The authors would like to thank J. A. Halbleib, Sr. for providing cross section tables for the model.

58. D. J. Johnson and G. W. Kuswa, RS 5241/1003, Sandia Laboratories, Albuquerque, NM Internal Memorandum (1978).

59. C. L. Olson, Phys. Fluids 18, 585 (1975).

60. C. L. Olson, Phys. Fluids 18, 598 (1975).

61. C. L. Olson, *Proc. IX International Conf. High Energy Accel. SLAC*, Stanford, CA (1974), p. 272.

62. C. L. Olson, International Topical Conf. on E-Beam Research and Technology, Albuquerque, NM, 2, 312 (1976).

63. S. Humphries, J. Appl. Phys. 49, 501 (1978).

64. E. Stuhlinger, *Ion Propulsion for Space Flight* (McGraw-Hill, New York, 1964).

PARTICLE BEAM SOURCE DEVELOPMENT

OVERVIEW

During the present reporting period we have been able to make significant headway in improving electron beam pinch intensity and efficiency, as well as in the production of intense ion beams. A new cathode design has resulted in attaining 14 - 17 x 10^6 amp/cm^2 on Proto I, and slight modifications to the accelerator, also described, are expected to further enhance this capability. This will permit us to more fully investigate enhanced coupling of intense beams with sources, and will allow us to explore pinches with EBFA-like module parameters much earlier than anticipated. In addition, we have been able to extend the energy deposition efficiency to a currently estimated > 60% onto 0.3 cm diameter spherical stalk mounted targets. This technique should allow us to extend our previous results on neutron production in magnetically insulated targets.

We also report several new schemes for high power current and voltage regulation which may be crucial in future machine designs and are already being used in our accelerator applications.

We have shown that ion beam diodes can be used in Proto I to produce proton beams with > 80% of the machine energy, and focused current density in excess of 30 kamp/cm^2 has been obtained in the initial experiments. Since magnetic field lines form the "virtual" accelerating surface in this diode, we believe that a technical basis can be established for repetition rated high efficiency ion diodes for future use in reactor applications.

A new laboratory area devoted to advanced concepts in application of pulse power to multistage accelerators for fusion has been set up. The first several stages of an experimental accelerator system, Pulselac, are in place and the first tests of the ion source have been made. In addition, computation has shown that space charge neutralization between acceleration stages can extend greatly the previous limits of current transport, and a system to supply neutralizing charge has been developed and tested.

REB CONCENTRATION STUDIES

Over the past several years, a large variety of pinched REB studies have been performed with the goal of obtaining reliable, stable pinches which efficiently convert electrical power to very high current density electron beams. The majority of the research in this area has involved the use of simple tapered hollow cathodes. Variations on this cathode theme have included use of axial protruberances, laser and gun-injected plasmas, axial wires, and moderate geometric modifications to cathode and anode surfaces. As a result of these studies, efficient electron pinches are routinely available at current densities from 1 to over 10 MA/cm^2 from accelerators in the 0.1 to 1 TW power range at impedances of a few ohms. The radial compression ratios of these pinches are typically 10 to 1, but all are from relatively small cathodes, since conventional large diameter cathodes have proved relatively unstable because of azimuthally nonuniform emission. For cases where strong axial bias currents are not used, pinch formation time is governed by the time required to form anode plasma. Anode plasma formation requires about 0.3 mCoul/cm^2 of beam deposition, which would consume a large fraction of the available beam energy for large diameter diodes. The use of bias currents with discrete cathode arrays (discussed shortly) may solve these problems.

Effective velocities for anode-cathode gap closure usually range from 3 to 5 cm/μs for high power diodes. Velocities well in excess of this value are seen when prepulse electric field levels are much over 2 kV/mm. This critical level is of course sensitive to details of cathode finish. As diode aspect ratio increases, impedance drops and current levels increase. In the past, electron beam generation efficiency in large low-impedance diodes has been limited because ion beam generation increases rapidly as total diode impedance drops to less than one ohm. The combination of effects cited has led to the ability to concentrate a few dozen kJ of electrons at a few ohms and at a few MA/cm^2. Although prospects for great improvement seemed limited, very promising results have been obtained during this reporting period using multiple cathode arrays in a single diode.

Multiple Cathode Arrays

During this reporting period several advances have been made toward making reliable pinches at low impedances. Previously, the best cathodes for Hydra (2Ω) pinches have been 76 mm O.D., 38 mm I.D. tapered hollow cathodes with 2.6 mm gaps. Proto I (7.2Ω) has pinched best with 25 mm O.D., 13 mm I.D. tapered hollow cathodes with 2 mm gaps. However, for Proto II (~0.5Ω) the gaps cannot be made small enough to obtain proper impedance over the duration of the pulse unless much larger diameters can be used. For this reason, biased cathode arrays have been developed on Hydra and Proto I for eventual use at low impedance.

The arrays generally consist of many (from 6 to a few dozen) discrete cathodes arranged in concentric circles about a central bias cathode. The discrete cathodes act somewhat like a large cathode. However, the partial electrical and magnetic decoupling of the cathodes from each other greatly improves azimuthal symmetry of emission. The bias cathode provides the magnetic field necessary for for pinching without incurring the ion losses present in a conventional ion-induced pinch. The details of operation of the bias field and the attainment of proper bias have been studied. It was found that a geometry which tends toward overbias will self regulate to a proper bias. The control loop is:

1. The bias current controls the outer flow (both in centering and in the radius at which the flow hits the anode);

2. The outer flow space charge controls bias cathode emission and therefore bias current.

This process maintains an accurate balance in the pinch throughout the power pulse once proper bias has been reach (see Fig. 1).

In operation, separate beams leave the discrete cathodes and each beam forms a prefocus after drifting a few centimeters. This drift distance can be calculated by considering a sheet beam of initial width equal to that of the cathode segment. The observed distance and the scaling with current is consistent with theory. These prefocused beams then are drawn towards the central bias cathode where they combine. These processes can be seen quite clearly in x-ray pinhole photographs. The tendency of the individual beams to repel each other near the central focus can also be observed.

Measurements of the current to 3 mm diameter stalk-mounted spherical targets show that more than 60% of the diode current gets to the target.

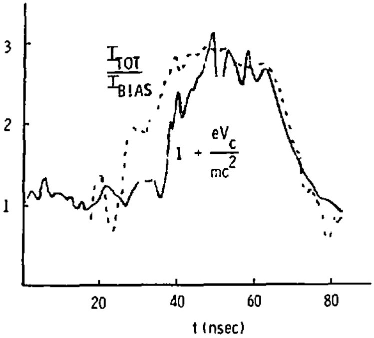

Fig. 1 Bias current plot for Proto I segmented cathode. "Proper" (parapotential) bias occurs when traces overlay.

This is a lower limit; the target current monitor flashes before peak current. This value appears to be about the same as obtained with smaller cathodes. Pinches on flat targets obtained with arrays do not appear to give as high a current density as pinches obtained with small cathodes due to more intense "wings" on the center pinch. These wings are presumably due to the low angles at which the outer current flows to the center. The arrays do show very constant impedance behavior for long times, even at low impedances.

Plans are nearing completion for extension of this technology to Proto II parameters. This will be tried soon after the additional prepulse isolation and polarity reversal are completed.

Multiple Electron Beam Development

The successful transport of a pinched REB through a plasma channel formed in the air has previously been reported.[1,2] This led to the multiple electron beam (MEB) concept which utilizes many independently generated pinched beams which are transported to and combined at a common target by use of plasma channels.[3] An experiment planned for EBFA I in 1980 using 36 beams is illustrated in Fig. 2. Here, 36 diodes are arranged around a common target and 36 current-carrying plasma channels generated by an external bank connect the diodes and the common target. Later this year, this MEB concept will be tested on Proto II with a 12 beam system. The 12 beams will be transported 46 cm over tungsten-wire-initiated air-plasma channels driven by two, 50 kJ, 100 kV low inductance capacitor banks which are being built by Maxwell Laboratories. The high voltage cabling and header system for this experiment has been designed and critical parts have been tested by use of a Nereus Marx generator.

The possibility of using a lower voltage bank and a step-up transformer for forming channels was also investigated. A series of mylar insulated transformers was built and tested with a 20 kV driver and outputs to 80 kV. Information was obtained on practical construction techniques, efficiencies, and use of non-constant impedance loads such as channels. Sceptre calculations were employed to model the circuit behavior. We concluded that transformers may indeed be cost-effective for the EBFA I system, but that time constraints prevented their use for the Proto II experiment.

For the MEB experiment we have decided to use the best available "conventional" pinches and determine the limits of energy transfer to targets obtainable using beam combination and enhanced deposition techniques. Recently, much effort has been expended to improve pinch reliability. In the upcoming Proto II tests of the MEB system, each successful accelerator shot will require 12 good pinches in 12 separate anode-cathode gaps, so reliability will be important. Recent work has led to mechanical and geometric improvements which should be adequate for the MEB program.

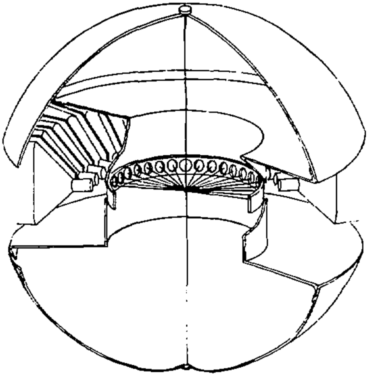

Fig. 2 Concept for multi-beam front end for EBFA.

"Rudakov-Type" Diode Research

Uncertainty in the area of diode physics surrounds the diodes used by the group at Kurchatov. They claim to obtain high current densities, low impedances, long impedance lifetimes, and extremely high specific energy deposition in thin foil targets by use of small diameter cathodes at relatively large anode-cathode gaps. A significant prepulse level is thought to be instrumental in the operation of the diode. Very recently the French group at Valduc has started studies including similar diode geometries.

The principle of operation of the anode cathode geometry used at Kurchatov in recent work is unknown. Rudakov's group obtains diode impedances of a few ohms accompanied by relatively slow gap closure while employing cathodes of roughly 1 cm diameter and anode-cathode gaps of several mm. This result is important because small cathodes generally produce small diameter pinches; if low impedance operation can be obtained, then very high current densities will result. When similar, high-aspect-ratio diodes have been tested elsewhere, higher impedance operation has been encountered. There has been speculation that the Soviet diode operation was dominated by a plasma filling generated by prepulse. This plasma filling might have different properties than the laser and gun-generated plasma studied in the past at Sandia. In a recent visit here, J. C. Martin (AWRE) suggested that a fast-rising prepulse voltage of several percent of the main pulse voltage might have beneficial results on diode operation. He outlined a possible theoretical explanation and also cited positive experimental results of prepulse effects on operation of a nonpinching radiographic accelerator diode.

To study this (hypothetical) beneficial-prepulse regime, an experiment was carried out with Hydra. An externally generated prepulse was applied to the anode-cathode gap and the effects on impedance history and pinch behavior were observed. The prepulse source had 25 ns risetime, 150 ns pulse length, 120 ohm output impedance, and peak voltage capability into an open circuit of over 200 kV. Under the conditions of the experiment, the peak prepulse voltages and currents achieved were generally up to 70 kV and near 1 kA. The prepulse was applied to the anode (mounted on a standoff insulator) from 50 to 300 ns prior to the main pulse. Cathodes used were of the Proto I variety, with 25 mm O.D., 13 mm I.D., and tapers of 20° to 30°. Gaps of from 2 to 4.5 mm were tested. Most of the shots had prepulse polarity the same as the main pulse. Results were as follows:

1. Application of voltage and the flow of current before the main pulse (the latter indicating surface turn-on and plasma generation) was universally and totally destructive to otherwise good pinching behavior. Anode damage became diffuse and irregular suggesting extreme beam instability, pinch wander, or no focusing at all.

2. Diode impedance was lowered but made very erratic by prepulse. Early time impedance behavior similar to gun plasma-filled diodes was observed (diode Z rising from a low value), the initial impedance being lower as the prepulse amplitude and time before the main pulse were increased. Precipitous gap closure often occurred.

3. Bullseye (grooved) cathodes had more rapid and probably more uniform turn-on during prepulse than did smooth cathodes, as expected.

4. Reverse polarity prepulse generally was not as harmful as normal polarity prepulse, but apparently only because a flat, smooth anode geometry presents fewer sites of field enhancement opposite the cathode to cause subsequent electron emission. Shots with reverse polarity voltage applied, but no current flowing, exhibited normal impedance behavior and reasonable pinching; shots with a bullseye pattern on the anode generated prepulse plasma and exhibited pinch destroying properties similar to the normal polarity cases.

For a wide range of prepulse timing and amplitude, no encouraging signs pointing to the existence of beneficial prepulse effects were seen in this experiment. The approach in our experiment has been to employ variable prepulse; this contrasts with the Soviet approach in which various cathode shapes were studied under fixed prepulse conditions. A possible extension of our work would be to vary cathode geometry over a wider range.

Pinching Experiments on Both Thick and Thin Flat Targets

In another test series, small cathodes were studied on Hydra without employing externally-generated prepulse. In this work, we found "optimum" performance with a 13 mm I.D., 25 mm O.D., 15° tapered hollow cathode operating with anode-cathode gaps in the range of 1.8 to 2.5 mm. This "optimum" performance was of course a compromise involving tradeoffs of pinch size, impedance, peak power, and pulse length. Most previous Hydra work has employed much larger cathodes and gaps to make more efficient use of the relatively long pulse available from Hydra. On solid carbon anodes, pinch sizes were roughly 2 mm diameter (pinhole photography) and peak current densities approaching 10 MA/cm^2 were inferred at total diode currents over 300 kA. Pinch broadening to 3 mm (with no sign of spatial instability) and impedance lowering by 25-50 percent occurred when vacuum-backed thin foil anodes were employed. Diode power levels to 0.4 TW, energies to 18 kJ, impedances from 4 to 10 ohms, and pulse widths near 50 ns were obtained.

The reduction in diode impedance for the thin foil cases is quite likely due to enhanced ion beam generation efficiency. The observed pinch spreading can reasonably be attributed to foil scattering and radial electric field effects. Because of this ion loss and the pinch spreading problem, we expect that electron current densities closer to 1 MA/cm^2 passed through the foils. This is consistent with the radiation temperature of 5 eV measured near 5000 Å for the case of 13 micron tantalum.

From this and other work, the following conclusions are drawn:

1. Pinch sizes and net energy transfer obtainable with small cathodes on Hydra are in the same regime as the Soviet and French work. Differences in treatment of cathode surfaces are understood simply in terms of the varying prepulse levels obtained on the various accelerators. Theoretical interpretations of physics of diode operation, of ion beam loss processes, and details of impedance trajectories are significantly different, however.

2. Based on our theory and experiment, the use of simple, large area vacuum-backed thin foil anodes seems to have limited potential for achieving efficient, "enhanced," high specific energy deposition with electrons. The design of targets surrounded by space-charge and current neutralizing plasmas and with externally supplied magnetic field should be emphasized. Available simulation and Monte Carlo codes should be used extensively.

3. The target geometries used by the Soviet group are significantly different than those tried here with high current density beams. This is a possible area for further research. The high temperatures inferred by them from indirect measurements remain a mystery. We are considering trial of their diagnostic techniques to see whether similar results are obtained, but we believe that diagnostics we are currently using offer a more reliable basis of quantitative data.

CONVOLUTED FEED FOR THE PROTO I ACCELERATOR AND OPTIMIZATION FOR SINGLE-SIDED OPERATION (PROTO I')

In double-sided operation, the Proto I diode employing small diameter 7 ohm cathodes has produced two simultaneous beams, each being 1.8 MV, 250 kA, 0.45 TW, 9 kJ, 24 ns FWHM duration. However, the use of these opposing beams to drive equatorially mounted, very thin, exploding pusher type pellets resulted in somewhat inefficient coupling of the beam energy into the target[4]. The reasons for inefficient irradiation can be ascribed to the absence of reflexing electron orbits (too low a ν/γ beam in the pinch) and to beam loss at a large radius after one or more passes through the thin target, a consequence of the opposing geometry of the beams. Recent work on single-beam irradiation of post mounted targets[5] has shown this to be a more favorable geometry for pellet irradiation. Plans for converting Proto I to single-sided operation (Proto I') therefore have been considered.

A two part approach will be taken for convoluting the power feed on Proto I to obtain a 1.8 MV, 500 kA, 1 TW, 18 kJ, 24 ns pulse for driving a single 3.6 ohm diode. The first part involves a modification to the peaking switches in the oil just outside the diode interface to reduce prepulse at a level acceptable for the smaller A-K gaps anticipated for 3.6 ohm operation (1 - 2.5 mm) and to provide for one method of "disconnecting" one of the diode feeds. The second involves rebuilding the inside of the diode to obtain a magnetically insulated vacuum convolute feeding either a single axial cathode or a multiple cathode array[6]. The optimum approach involves employing the reduced prepulse of the oil modification and the vacuum convolute, since the latter employs a lower inductance cathode geometry to keep L/R

= 27 nH/3.6 ohm down to 7.5 ns for fast cathode turn on. If the magnetically insulated vacuum feed proves to be too lossy, the convolute can be performed in the oil and one side of the existing Proto I diode will be removed.

Vacuum Convolute

Convolution within the diode (Fig. 3) is performed by passing six current feed rods through holes in the anode plane. These holes are of sufficient size to allow for magnetic insulation of the electron flow. Six standoff posts (#4 in Fig. 3) can be metal or dielectric material for use as flashover switches in the anode circuit. The spacing anode and cathode feed plates (#13, #14, #15, and #16, respectively) can be varied by different sets of rod spacers (#1 and #2).

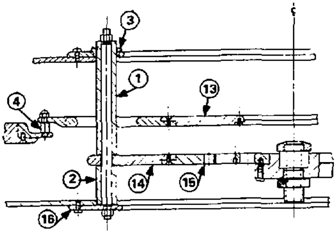

Fig. 3. Assembly drawing of vacuum convolute parts.

The electron sources to be used will be small (~3 cm O.D.) tapered cathodes with or without shank flashover switched, or a biased array of cathodes.

Diode turnaround should be relatively fast as the flashover feed (#3) will allow the diode to be disassembled in much the same way as it presently is done. No machining operations will be required on primary existing diode parts.

Oil Convolute

The area of the accelerator to be modified for the oil convolute is shown in Fig. 4.

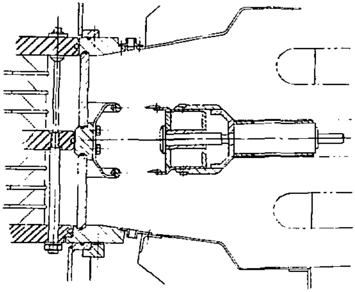

Fig. 4. Cross-sectional drawing of Proto I showing line feed just outside diode region.

The self-break blade switches on the center line of the Blumlein stack help impedance match the feed between the lines and the diode and have a mild prepulse suppression effect in that through capacitive division with the diode they apply only 0.7 of the line prepulse to the diode and result in ± 35 kV peak appearing across the A-K gap. The proposed modification (Fig. 5) has two important features. First, the two blade switches for a single line will be replaced by six ball type switches employing ground plane feed-through shields (developed by VanDevender[7]) for prepulse suppression. Switch capacity calculations indicate ≤ 0.175 of the line prepulse will be fed through, or about one quarter the previous value (± 9 kV). Second, by removing the top diode ground plane feed (part #3 in Fig. 5), the energy in the top Blumlein stack should be efficiently delivered in parallel with the bottom stack to only the bottom half of the diode. The only power loss will be through capacitive coupling through the oil to ground via the top diode ground contact; this path will act as a high impedance transmission line (> 40 ohms) and therefore will not be significantly lossy. If the top diode ground plane remains connected, both diodes can be fed as in the original configuration, also with reduced prepulse.

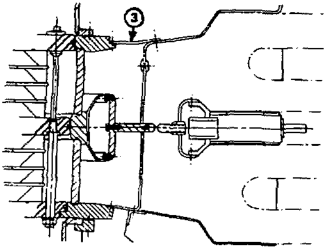

Fig. 5. Cross-sectional drawing showing proposed modification for prepulse reduction and convolution of the power flow in oil.

To optimize the Proto I diode for single-sided experiments, the problems of additional prepulse suppression to obtain fields $\leq$ 2 kV/mm in the gap and of obtaining a tight pinch from a 3.6 ohm diode must be addressed. A cathode design presently being investigated (shown in Fig. 6) appears to satisfy both problems. The center of the cathode mounting shank is made of Lexan and acts as a capacitive divider during prepulse, then flashes over the outer surface in a multichannel fashion at the start of the main pulse. Calculations indicate only 0.29 of the diode prepulse voltage (i.e., 2.6 kV with the new oil switches) should be applied across the gap. This level should be sufficiently low for gaps > 1.3 mm.

The cathode tip employs a geometry previously found to pinch fairly well on Proto I.[8] The 10° tapered surface appears to run stably at 4 ohms for ~25 ns as can be seen in the voltage and current plots in Fig. 7, taken from a typical shot with the machine feeding both diodes. From time-integrated x-ray pinhole photographs taken of flat, thick targets, the pinch profile (Fig. 8) was estimated to have an axial current density of 14-17 MA/cm^2 (at ~1.1 MV) with a full width half maximum diameter of 1.5 mm and 200 kA of diode current flowing within the FWHM. Extrapolation to a factor of 2 in current and diode

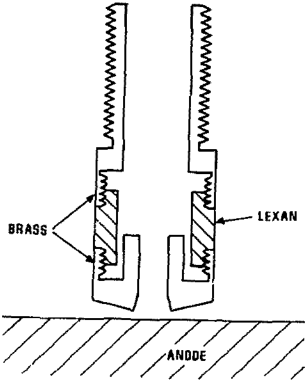

Fig. 6. Cathode geometry being tested for 3.5 ohm operation at 1 TW: 29 mm O.D., 12 mm I.D., 10 deg taper.

operation at 1.8 MV hopefully will be straightforward. Additional optimization of this cathode at the 1 TW level should help determine its possible use in Hydramite and EBFA-type diodes.

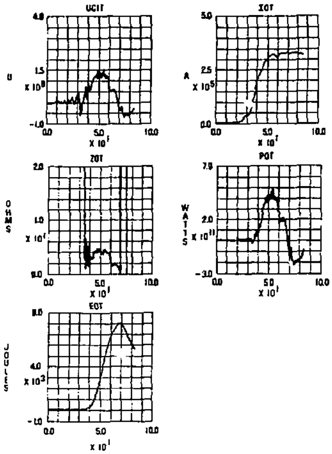

Fig. 7. Corrected voltage, current, impedance, power, and energy plots vs. time for the cathode in Fig. 5, before accelerator modification.

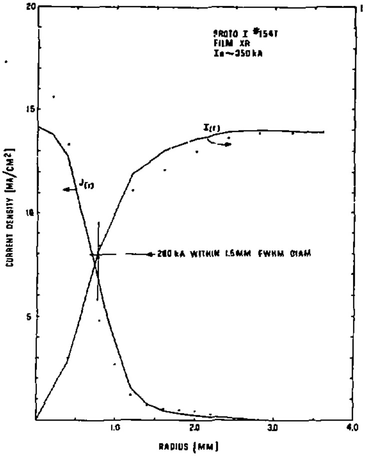

Fig. 8. Normalized scan of a time-integrated x-ray pinhole photograph showing current density J(r) and current I(r) as a function of radius.

NONLINEAR PULSE POWER CIRCUIT ELEMENTS

Introduction

It is possible to improve the focusing of very large energies onto small areas by controlling some of the parameters which normally vary during the pulse such as prepulse, voltage, and current. For example, by employing a fast opening switch based upon the concept of plasma erosion,[9] prepulse levels have been greatly reduced so that plasma formation and movement would not change the effective diode geometry before the power pulse. Under these conditions some of the most intense pinches known have been produced; this material was reported in the last semiannual report. We report here several other means under development for regulating large currents or voltages. Applications include regulation of potentials applied to successive stages of a multistage ion accelerator Pulselac (described elsewhere in this report), programming voltages for ion bunching, and in the future for inductive energy storage.

Current Regulator

The current regulator is based upon the plasma erosion concept.[9,10] A schematic is shown in Fig. 9. A plasma gun supplies a plasma of density n_o, velocity V_p, and radius R at the cathode region. It is characteristic of the plasma to attempt to keep the ratio of electron to ion current equal to the square root of the ion to electron mass ratio for currents low enough that self-magnetic fields can be neglected. In equilibrium the ion current is fixed by the plasma supply rate and the electron current is thus fixed to the value $I_o = R^2 n_o e v_p \sqrt{M}$. Since the sheath must respond to the load or source changes; there is a frequency response limit which sets requirements on the plasma guns. These conditions can be met for nanosecond response with available sources.

An additional complication is that of the self-magnetic fields. This has the effect of reducing the control current for currents appreciably higher than 8.5 kA per section. This can be seen in Fig. 10. The numbers on various curves correspond to the regulation current I_o in units of 8.5 kA for no magnetic effect. It is seen that there is still an appreciable flat region for high currents, but at values well below $I/I_o = 1$. As an example, for $I_o = 170$ kA ($I_o/I_a = 20$ in the figure) the device regulates at $I/I_o \sim 1/2$ or $I \sim 85$ kA. In addition, there is a negative impedance at low voltage. This might be useful for some cases. The negative impedance and other magnetic effects can always be avoided by running many parallel sections.

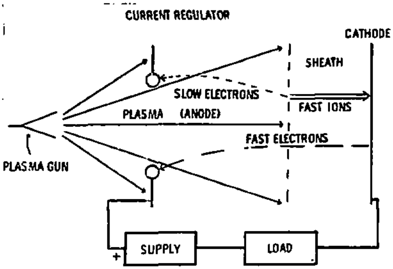

Fig. 9. Schematic of the current regulator. The device takes advantage of the tendency of the plasma to adjust the sheath size until the ratio of electron current to ion current is $\sqrt{M}$. The regulating current is $I_o = \pi R^2 n_o e v_p \sqrt{M}$.

The current regulating feature in plasma-filled diodes has been seen experimentally[10] and is being used in a related device, the plasma injected microsecond diode, covered elsewhere in this report.

Voltage Regulation

This device is based upon the same principle as magnetic insulation; however, the magnetic field is supplied from external coils, and the regulation voltage is determined by the equivalent gyroradius of electrons which are field emitted from a cathode and accelerated by the voltage across the gap. For the coaxial device shown in Fig. 11, the relation $\beta\gamma mc \lesssim eB(R_A - R_k)$ gives the regulation.

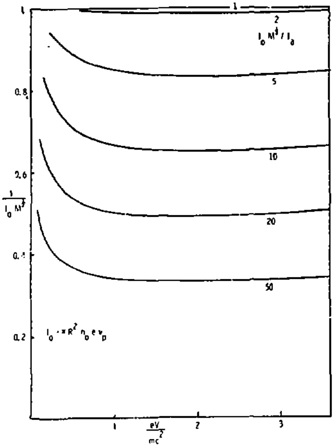

Fig. 10. The device characteristic for several values of I_o/I_a. By paralleling several elements (or equivalently by distributing return conductors throughout the device) the characteristic can correspond to $I_o/I_a \sim 1$ for arbitrary total current.

condition, where β and γ are for electron of energy eV, B is the magnetic field in the gap, and R_A, R_K are the anode and cathode radii. When the electron orbits are large enough (i.e., voltage sufficiently high) to cross the gap, current flows. At lower voltage an EXB drift in the azimuthal direction results in no net current. The characteristics load behavior for this device is shown in Fig. 12 for a typical circuit; in this case V would be regulated for load impedance > 20 Ω. An effect which can alter the device from the ideal can arise from self-current, induced-magnetic fields which cause drifts. The characteristic curves may also be modified for special applications by offsetting the electrodes so that the gap length is variable. The voltage regulator is currently being used to regulate the gap potential in Pulselac.

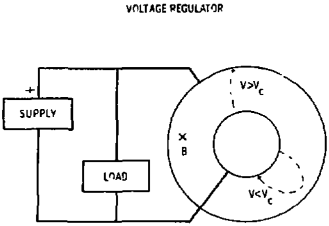

Fig. 11. Schematic of the voltage regulator The current is a circulating (azimuthal) flow for voltage at which electrons cannot cross the gap.

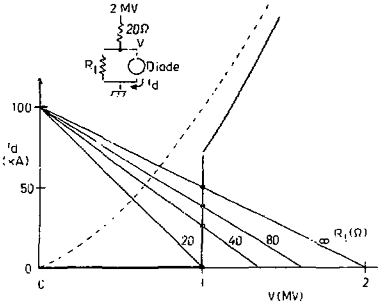

Fig. 12. Characteristic curve for a hypothetical example. The zero impedance segment at 1 MV could be made finite by offsetting the axes of the electrodes.

PROTO I SEMISPHERICAL MAGNETICALLY INSULATED ION DIODE

Introduction

The basic approach for generating and accelerating ions using pulse power is to suppress electron flow that normally occurs at the high required electric fields, and encourage the production of ions at the anode surface. The electron flow can be reduced or eliminated by providing magnetic fields transverse to the electron flow. Ions with much greater mass/charge ratios than electrons can easily cross field lines relatively undeflected. One approach to provide this field is by means of the intense current in the beam itself, as occurs in an intense pinch electron diode. Another approach utilizes magnetic fields supplied by external coils operated independently of the beam current. The former aproach is being explored at NRL, and the latter approach (first proven at low power levels at Cornell) has been selected as Sandia's main approach.

The past semiannual report described initial experiments with ion diodes at the high power and voltage of the Hermes accelerator. This first experiment was designed to produce a quasi-line focus uncorrected for broadening due to particles crossing net magnetic flux applied to stop electron flow. This experiment extended the range of voltages from the previously studied regime < 1 MV to the 5-10 MeV region. In addition, we learned how electron leakage can reduce the efficiency of the first configuration and conceived a solution to the problem in the form of a two-sided configuration that was expected to solve the leakage problem and test several other principles as well. The initial tests have been completed with this apparatus, yielding very positive results; i.e., electron leakage is a minor loss, and the focusing properties appear to be very favorable.

Work Accomplished

The diode and ion beam diagnostics used are shown schematically in Fig. 13. The magnetic field coils are energized with a 20 kV, 48 kJ capacitor bank designed and fabricated for the diode. The magnetic field reaches peak value in 70 µs (1.5 mm skin depth in aluminum); therefore, the applied field is contoured into a spherical shape in the anode-cathode gap by the spherical sector aluminum anode. Initial tests of the two magnetic field coils at bank voltages up to 17 kV demonstrated mechanical failure modes which were overcome using high strength epoxy resin coil castings.

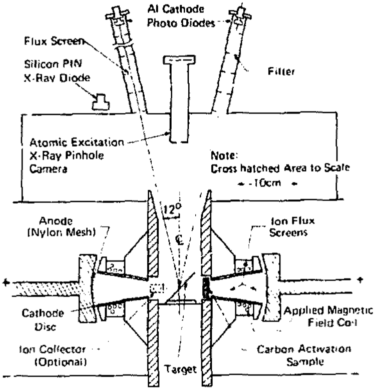

Fig. 13. Schematic of the apparatus.

Subsequently, the coils were observed to fail due to internal electrical breakdown when energized in conjunction with the Proto I generator. This problem was traced to inductive pickup of voltages in excess of 1 MV across the coils due to the mutual inductance of the coil leads and the ion diode and nonazimuthal flow of the Proto I current near the coils due to the complicated structure of the ion diode. These problems were overcome by rearranging the coil current leads and employing thin stainless steel rings to buffer out short pulse transient magnetic fields, while allowing nearly uninhibited passage of relatively slow magnetic fields. With these modifications the coils were operated successfully with Proto I at an applied bank voltage of up to 15 kV to give a magnetic field of 16.5 kG in the anode-cathode gap. Additional problems were plasma produced by small arcs between metal parts of the diode when the coils were energized and a Penning discharge across the field coil leads which effectively shorted the capacitor bank prior to peak magnetic field. These problems were overcome for the first run by using epoxy, fiberglass parts, and dielectric spray coatings to eliminate sources of arcs in the diode and complete electrical insulation of the coil leads. More permanent solutions will be incorporated in the future.

The ion diode utilizes a virtual cathode produced by electrons emitted from the cathode edge (see Fig. 13 which moves axially along magnetic field lines to establish a uniform equipotential surface near the anode. This equipotential surface applies a rapidly rising electric field to the nylon mesh mounted upon the aluminum anode. An anode plasma is then formed (thought to be due to surface flashover) which serves as a source of protons. These protons are accelerated across the anode-cathode gap and drift toward the diode center line. Since all magnetic field lines reconnect between anode surface and diode center line the ions are emitted from the anode with zero canonical angular momentum and thereby can be focused to the center line. When drifting through the magnetic field the ions are space charge neutralized by electrons emitted from the walls of the drift region and transported along magnetic field lines.

Typical electrical characteristics of the diode are shown in Fig. 14. These data were taken with a 9 mm, anode-cathode gap, anode mesh surface area of 414 cm^2, and 13.5 kG magnetic field of in the anode-cathode gap. Since no prepulse suppression was employed, a 240 MHz, 30 kV amplitude sinusoidal prepulse persisted for 800 ns prior to the main voltage pulse. After approximately 15 ns from the beginning of the main pulse the corrected voltage rises rapidly to 1.5 MV. The anode plasma formation is complete at approximately 24 ns and the current then rises with an L/R time defined by the 55 nH of each parallel side of the Proto I vacuum diode used. The diode current was measured with dB/dt loops at three radial positions starting near the cathode shown in Fig. 13. The current shown in Fig. 14 is an average of the three measurements on each side of the diode since no electron current outside of the anode-cathode was noted. At approximately 35 ns the impedance stabilizes at approximately 2.5 ohms. Also shown in Fig. 14 is a calculated impedance obtained by multiplying the Child-Langmuir space charge limited ion current of

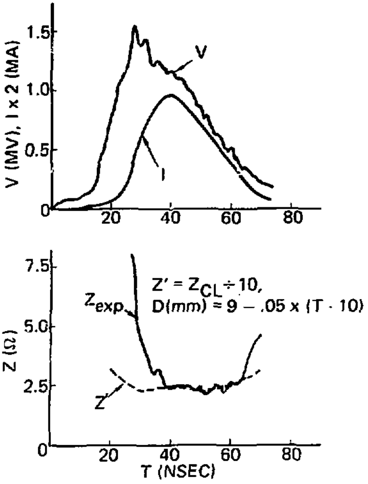

Fig. 14. Electrical characteristics of the diode.

$$I_{cl} = 55\ V^{3/2}\ A/D^2$$

by ten. Here V is the diode voltage in MV, A is the surface area of the anode, and D is the anode-cathode gap. For the calculation the diode gap D was assumed to decrease linearly at 5 cm/μs after current initiaton at 10 ns. This gap closure rate is the same as has been observed on the Proto I generator with pinched electron beam diodes. It is surmised that although the diode current includes a fraction due to electrons, which will be described below, the ion current exceeds the space charge limited value because the anode-cathode gap contains a concentration of magnetically trapped electrons which partially charge neutralize the ion beam. Indeed, it is the same space charge that serves as the virtual cathode surface mentioned earlier.

The electron current was determined by monitoring the thick target bremsstrahlung from the diode on a time-resolved, and time-integrated but spacially-resolved basis. These data were taken with reduced magnetic field and nylon mesh ion source, and also with high magnetic field and no mesh, using a silicon PIN diode which viewed the entire anode (see Fig. 13) and an x-ray pinhole camera. Both of these diagnostics were filtered by approximately 1 cm of aluminum. With no nylon mesh (nearly zero ion current) the total diode current was only 50 kA at a peak corrected voltage of 2 MV. These measurements were then used to scale the x-ray signal for experiments when ion beams were generated. The thick target electron beam bremsstrahlung was assumed to scale with V^2 based upon the x-ray tube relationship

$$\text{X-ray Yield} = 7 \times 10^{-4}\ Z\ V^2$$

because of the 90° observation angle. These measurements place an upper limit to the peak electron current of 100 to 125 kA for the ion beam experiments.

The total proton current was measured using the carbon activation technique[10] whereby the decay of N^{13} from the $C^{12}\ (p,\gamma)N^{13}$ and $C^{12}\ (d,n)N^{13}$ reactions are observed from the delayed position emission from N^{13}. A Fortran program was written for the ModComp II on-line computer system which calculates the total N^{13} activation yield from the current-voltage characteristics of a given diode experiment. The program assumes all the diode current is in the form of hydrogen with the deuterium contribution to the current taken to be 1.5×10^{-4} (natural abundance). Above 1.2 MV the deuterium cross section exceeds the proton cross section by 0.7×10^{4}; it therefore contributes equally to the activation. Activation measurements were made at 5 cm, as shown in Fig. 13, and 13.5 cm radii in the diode. At the 5 cm radius where the ion current density approaches 4 kA/cm^2 one or two 34% transmission stainless steel flux screens were used to attenuate the ion beam. These diagnostics indicated no carbon blow-off with one or two screens and a peak current density of approximately 3.5 kA/cm^2 at the 5 cm radius. At a radius of 13.5 cm the peak current density was observed to aproximately 1 kA/cm^2. These ion current measurements were in agreement with ion collector[11] signals observed at equal radii. The ion collector signals were also compared on a time resolved basis with the theoretical ion current allowing for ion time-of-flight. Such a comparison is shown in Fig. 15 for a collector at the 5 cm radius. The theoretical ion current was obtained by a computer program which time disperses the diode current at subnanosecond intervals for the ion velocity attributed to the associated instantaneous diode voltage. Exellent time-of-flight agreement was noted at the 5 and 13.5 cm radius. These diagnostics indicate a peak ion current of approximately 360 kA and 230 kA at the 13.5 and 5 cm radii, respectively. It should be noted that approximately 20% of the ion current would be lost between these radii upon the eight coil support ribs because of the "S" shaped orbits which protons undergo when passing through the applied magnetic field. The remaining 60 kA of lost current against the walls of the diode may be due to beam blowup due to nonperfect space charge neutralization.

An attempt also was made to measure the ion current with the D(D,n) He^3 reaction but the neutron output observed was typically 5 to 10 times lower than expected. This discrepancy is considered due to deuterium deficiency in the outer layer of the CD_2 coated nylon surface flashover ion source used. Similar deuterium coated anodes on a Febetron neutron source give only 10% of the expected neutron yield on the first shot

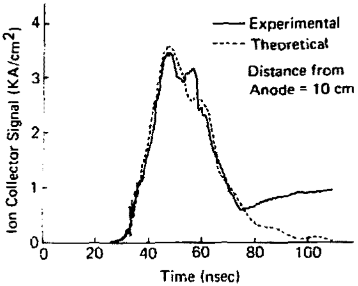

Fig. 15. Experimental and calculated ion collector signal.

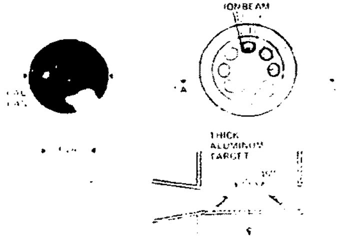

Fig. 16. X-ray pinhole photograph of the aluminum atomic excitation K-line radiation from a thick aluminum conical target.

because of absorbed hydrogenous material on the anode. This material is normally liberated after one of two neutron shots fired sequentially.

The focused ion beam profile was determined by analysis of aluminum K-line radiation produced by proton induced atomic excitation. The 1.49 keV K-line radiation was observed with an evacuated x-ray pinhole camera using Kodak no-screen film. Photographs obtained with thick conical and thin planar aluminum targets are shown in Fig. 16 and 17. The conical target data indicate the well-defined individual ion beams which arise from the eight sectors of the diode. Densitometer scans were made of the beam profile recorded in each photograph. When corrected for geometry the scans for the planar target shown in Fig. 17 indicate that 10% of the beam which entered the hub of the diode at the 5 cm radius would have struck an area of 0.25 cm^2 if the eight ion beams from the diode would have been superimposed. Based upon the same assumptions 50% of this ion current lies within a radius of 0.95 cm implying an ion beam divergence of 3°. The actual peak current density observed was estimated to be only 36 kA/cm^2, however, because of the target slant angle. This current density compared well with a value of 38 kA/cm^2 determined from the peak absolute optical density of the exposed film. This result was obtained using numerically calculated[12] x-ray production

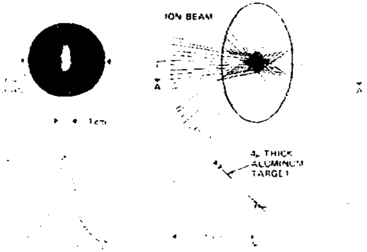

Fig. 17. X-ray pinhole photograph of the aluminum atomic excitation K-line radiation from a thin aluminum target.

efficiencies for 1 MeV protons (25 ns pulse) for the foil geometry used and the x-ray film sensitivity.[13]

This current density was further checked with blackbody temperature measurements of the thin aluminum foil targets. These measurements were made with bare aluminum cathode photoelectric diodes operated at 1 and 2 m from the target as shown in Fig. 13. The results shown in Fig. 18 (taken from the experiment photographed in Fig. 17) were obtained from the theoretical detection response versus blackbody temperature. This response was obtained by multiplying the blackbody spectra for several temperatures by the detection response curve and integrating these products over photon energy. This temperature measurement is compared with a hydrodynamic response calculation in Fig. 18. The theoretical temperature was determined with Sandia code CHART-D assuming a 0.8 MV proton beam incident upon a 4 micron thick aluminum foil at 60° from the normal angle. For the calculation the ion current pulse was assumed to be that shown in Fig. 18 and the expansion to be one dimensional. The current pulse used closely approximates that obtained with an ion collector at 5 cm (Fig. 15) with an allowance for the additional drift time to the target. The calculated temperature reaches 10 eV at approximately 50 ns prior to the observed peak in temperature. This discrepancy is at least partially due to the enormous boost in temperature expected at the front surface of the expanding foil plasma due to the current of low voltage ions which arrive late in the pulse. These ions would also be additionally delayed due to time-of-flight to the target. This calculation can only serve to qualitatively check the current density estimated above because of the variation in ion energy throughout the pulse. Future analysis of foil response temperatures will be made with a proper ion energy treatment.

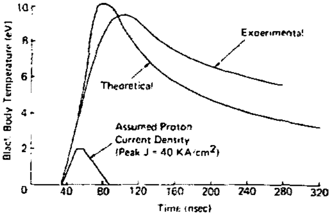

Fig. 18. Experimental and calculated temperature of 1 μm thick aluminum foil under the influence of the ion beam.

HIGH CURRENT LINEAR ION ACCELERATOR DEVELOPMENT

Introduction

Within the past year, an experimental program (Pulselac) has been initiated on the development of very high current pulsed linear ion accelerators.[14,15] Such devices have great promise for application as inertial fusion drivers.[15] They share with light ion diodes and conventional accelerator proposals the benefits of ions versus electrons or photons. These include high efficiency of production, focusing by nonmaterial lenses, and favorable classical interactions with matter which allow them to be considered for a wide variety of targets. In contrast to light ion diodes, the conversion of electrical to particle energy is expanded in time and space so that the power flow requirements are modest. Also, it is possible to decrease the inherent beam divergence from the injector by post-acceleration so that simple geometric standoff appropriate to a reactor scenario is theoretically feasible. When compared to conventional accelerators, there are a number of advantages, chief among them the fact that much lower beam energies can be used (while meeting the power and divergence requirements) and the cost per length of the accelerator should be comparable or less than a standard RF LINAC. A reduction in capital investment by an order of magnitude is not unreasonable.

Beam Neutralization

The major limitation on current transport in an ion linear accelerator is the space charge blowup of the beam; thus, the key to achieving higher currents is to provide for beam neutalization. The method we have studied is to locate sources of electrons on the conducting boundaries of the beam transport region that can rush in at the appearance of the beam. It has been found that in order for complete neutralization to occur, the electron distribution must have low energy and have sufficient time to be randomized in velocity. This can occur naturally if the electrons are prevented from flowing backwards in the potential gradient of the accelerator (by magnetic fields for instance). The process has been studied by computer simulation[17] with optimistic results. Under the proper circumstances, electrons can provide almost complete neutralization of intense ion beams with current rise times on the order of nanoseconds.

Application of Principles

The conditions for electron neutralization can be met in the Alpha configuration[14] (shown in Fig. 19), the basis of the Pulselac experiment. The accelerator consists of long drifts separated by narrow acceleration gaps pulsed in sequence as the beam bunch moves axially. Sets of four carefully designed coils[18] provide the magnetic fields shown. The radial magnetic fields insulate the acceleration gap, so that strong pulsed electric fields can be applied. They also prevent electron backflow, allowing the proper distribution for neutralization to be set up inside the drift tubes so that neutralization can occur if suitable electron sources are provided. Since the beam is unneutralized in the acceleration gap, keeping these narrow minimizes the effects of space charge. Shaping of the magnetic fields can influence the flow of electrons to form virtual electrodes to provide electrostatic focusing forces in the gaps. Since large currents are projected for such devices (many kiloamperes), the gaps must be powered by pulse forming components rather than stored radio frequency energy, which has technological precedence in inductive electron accelerators.[19]

The use of pulse line excitation for nonrelativistic beams raises the possibility of klystron-type instabilities. This has been studied numerically with the PILAC code,[15] and could prove to be a severe problem. A possible method of solution involves the development of high power voltage regulators[20] which can maintain constant gap voltage with good efficiency despite fluctuations in the beam current. The principle of these regulators is described elsewhere in this report.

Electron Sources

A key requirement for the success of Pulselac is the development of electron sources that can supply the high instantaneous currents needed for

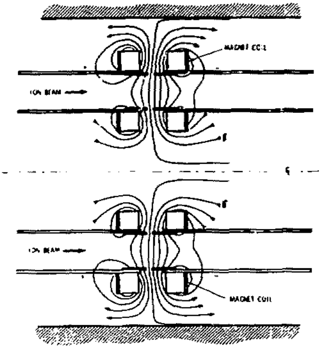

Fig. 19. Alpha configuration.

neutralization. An inspection of the Alpha configuration (Fig. 19) shows that large areas of the wall must supply electrons; to provide these with filaments would require a huge power input. A promising solution is the use of surface spark discharge plasma sources.[21] The concept of these devices is shown in Fig. 20.

A column of metal segments separated by small gaps is plated on a thin insulator. This assembly, along with a potted ballast resistor, is mounted to a conducting surface; in this case, the surface is the inside of a drift tube. A high voltage pulse (10 kV) is applied, and charges up the first capacitive element. When this reaches a certain voltage, a surface discharge occurs between it and the second element, producing a dense expanding plasma. This process continues down the line. Arbitrarily large areas can be handled by paralleling columns.

Experiments have been carried out with these sources. The ignition of a flashboard inside the Pulselac drift tube is shown in Fig. 21. Less than one joule is required to initiate 200 sparks over a 350 cm^2 area. Langmuir probe measurements at 1 cm from the board surface indicate the arrival at 0.5 microseconds of a plasma with $n_e \sim 10^{14}\ \mathrm{cm}^{-3}$, kTe ~ 6 eV, and a lifetime of somewhat over a microsecond. It should be possible to extract $\gtrsim 1\ \mathrm{kA/cm}^2$ of electrons for a short time from such a plasma. In practice, the flashboard will be fired approximately one microsecond before the beam passage to allow sufficient time for expansion. Optical measurement indicated a voltage transit time of about 100 ns through a 35 cm resistive-capacitive flashboard circuit.

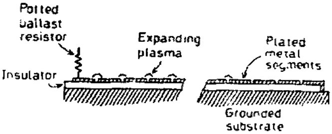

Fig. 20. Principle of flashboard electron source for producing a column of dense surface sparks.

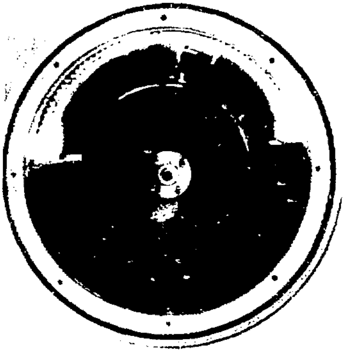

Fig. 21. Tests of flashboard in Pulselac drift tube (integrated photograph).

Pulsed Power Developments

The Pulselac experiment makes some unique demands on pusled power technology, and the resulting voltage system took considerable development. The primary requirement is that every time the beam bunch arrives at an acceleration gap, it sees a negative potential drop that is not additive over all gaps. The second requirement, a necessity motivated by the developmental nature of the device, is that the voltage system be extremely flexible and allow easy access to the machine for modifications. A circuit diagram is shown in Fig. 22. It was not feasible to purchase ferrite cores capable of driving 10 kA, so a sequenced electrostatic drive was chosen. In order to use only one switch per gap, the Blumlein lines are floated with respect to use only one switch per gap, voltage at each gap. Power for the Blumlein lines and triggers, diagnostic cables, magnetic field power and flashboard power are all brought through large high voltage isolation inductors. Triggering is accomplished with a low inductance, 100 kV Marx generator driving lengths of passive delay line. The charge resistors isolate the lines from one another as well as damping oscillations in the charge line.

The Blumlein lines are composed of 60 ohm, 40 kV coaxial cable. The cable has a relatively small diameter (7/8") so it is easy to handle; the pulse length as well as the characteristic impedance of a stage can be changed in about one half day. A stage can operate as low as 15 ohms. The system is completely air insulated (except for the Marx generators and line switch) so it can be opened quickly and cleanly. The entire assembly rests on an insulating track, so it can be broken at any point by one person. Fig. 23 shows a photograph of Pulselac with the injector stage in place. Fig. 24 shows typical injector voltage traces, as well as options for pulse shaping with the addition of shunt circuit elements. Over 500 shots at line charge up to 305 kV have been fired without cable failure.

Magnetic Insulation Results

The magnetic insulation properties of the first annular gap (used as the injector) were studied in the absence of ions by

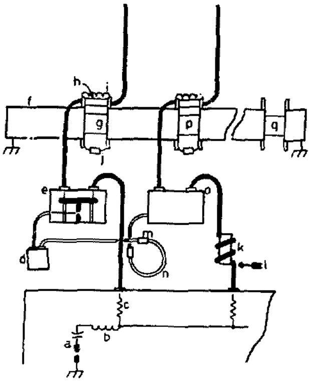

Fig. 26. Pulselac pulsed voltage system.

a) Marx generator, 25 kJ, 500 kV.
b) Prepulse suppression inductor.
c) Blumlein isolation and damping resistors.
d) Trigger Marx generator (100 kV).
e) Blumlein line switch.
f) Injector stage
g) Injector gap.
h) 400 kV Teflon plug.
i) Blumlein line charging inductor.
j) Shunt circuit elements for pulse shaping.
k) Second stage isolation inductor.
l) Entrance point for magnet power, trigger line, etc.
m) 100 kV plug.
n) Delay line.
o) Second stage switch.
p) Second gap.
q) Extraction gap voltage isolator.
Heavy lines indicate Belden 8871 cable, hollow lines indicate RG213.

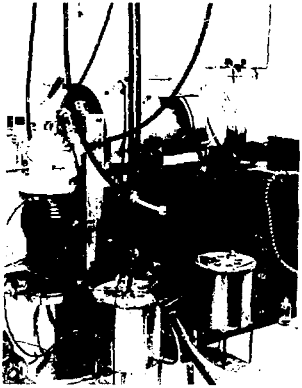

Fig. 23. Pulselac during injector testing.

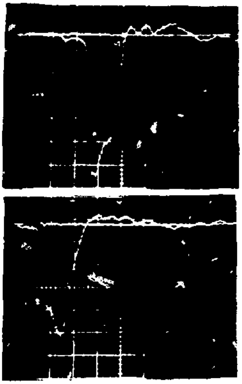

Fig. 24. Voltage traces of injector under ion load.

(A) Shunt resistors and inductors only.
(B) Addition of shunt capacitors.

using metal electrodes. These tests were important for three reasons. First, they would provide a test of the simultaneous operation of the pulse line with the invacuum insulation coils using inductive isolation to power the upstream coils at high voltage. Second, they would indicate the accuracy of the fairly complex annular magnetic field pattern. Third, they would show (by the presence of leakage currents) whether there were unanticipated electron drifts using the novel radial magnetic field insulation.

Typical results are shown in Fig. 25. As the magnetic field is increased, the diode electron perveance decreases significantly. Currents are measured by a shank monitor which registers only diode current with capability for measuring current as low as 100 A. In contrast to cylindrical magnetically insulated diodes, there is no unique definition of B* (the critical insulating field) and there is no sharp perveance cutoff, since B_r varies with radius. In general, the insulation above B* (defined at the maximum radius where the field is weakest) is excellent. The extremely low currents qt high magnetic field, (< 300 A) indicate there are no discontinuous electron drifts in the applied fields. These results imply that if ions could be extracted over the entire available area, a diode efficiency of 93% could be obtained (the electron perveance is reduced a factor of 600 from the maximum theoretical value.)

Injector Studies

Although Pulselac has the capability to accommodate a wide variety of light and intermediate ions, studies to the present have been limited to protons because of the familiarity of the surface flashover proton source. The injector anode in this case is a lucite annulus with copper epoxy inserts. The ion diode behaves as a high performance magnetically insualted ion injector. The major results are:

1. Current densities up to 30 A/cm^2 of protons have been obtained, in good agreement with Child-Langmuir predictions. This is to be expected, since the diode has a high degree of symmetry and electron orbits should be closed.

2. Extrapolation of current density measurements to the total diode area show that the efficiency is high, from 75 to 100 percent.

3. Damage plates show good azimuthal uniformity with a radial variation of current density. Peaking of the current density at the 10 cm radius (annular axis) is consistent with the distance of closest approach of the virtual cathode formed along the curved magnetic field lines.

4. Total currents of 6 kA at 250 kV were obtained using a 30 ohm line. With the 15 ohm line option and a slightly smaller gap spacing (7 mm was used), it should be easy to reach the 10 kA design level.

Propagation studies are presently being initiated. An interesting phenomenon is that under very good vacuum conditions, the emerging proton beam appears to be space charge unneutralized and rapidly expands to strike the drift tube wall. In all previous intense ion beam experiments, neutralization occurred automatically. This opens the possibility for definitive tests of the flashboard electron source and neutralized beam propagation studies across magnetic fields.

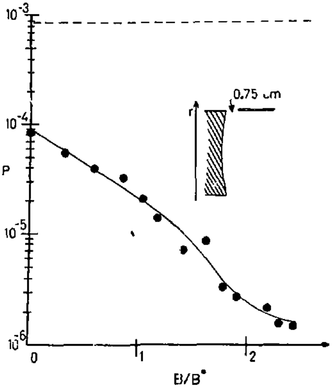

Fig. 25. Magnetic insulation results (no plasma sources).

PROGRESS ON A FIVE-FRAME X-RAY PINHOLE CAMERA

Introduction

In a shadowgraph mode, flash x-radiography has been proposed to study hydrodynamic instabilities in ICF targets during implosion, and a single-frame, gated camera has been designed and tested for this purpose. However, other relevant ICF phenomena such as e-beam pinches and pellet dynamics manifest themselves as luminous objects in the x-ray and UV regions. A five-frame, gated x-ray camera has been developed to look at such events with pinhole optics and is currently being evaluated. The camera should be useful for recording luminous events at five different sequential times or at the same time with different exposures or wavelengths.

The Five-Frame Camera

The camera (Fig. 26) consists of four major sections: a five pinhole optics stage; an x-ray-to-electron image converter; an electron transport stage; and an electron-to-optical image converter. In the first image converter stage, five independently gated microchannel plates (MCP) sample the x-ray images produced by the pinhole optics system in a 10 ns time interval and yield five electron images, which are transported by a curved magnetic field to a region outside the line-of-sight of the x-ray radiation beam. (This curved field allows the input plane of device to point directly at the x-ray object, rather than at an oblique angle). The second image converter (a MCP-phosphor pair) amplifies the electron images and converts them into visible images which may be recorded on ordinary polaroid film.

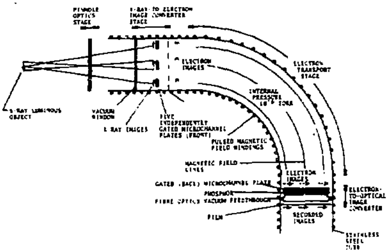

Fig. 26. Principle parts of five-frame pinhole camera for recording x-ray luminous events produced by a REB accelerator. (Only three images are shown.

This system has been used in pulsed and steady state modes to image the luminous target of a Febetron 706 x-ray source (5290 Fexitron tube) operated at 600 kV. The x-ray source is about 3 mm in diameter and is luminous for about 3 ns. As monitored from the voltage traces, the camera shutters can be gated in 10 ns time intervals, and some evidence exists that this time may be shortened to 6 ns with the present pulsers, and to shorter times with other existing technology. The optics can be aligned to produce five images with an object-to-pinhole distance of 25 cm and magnification of about 2X. The low intensity of the x-ray source used for testing set a limit on the smallest pinhole diameter to 0.8 mm, which also limited the resolution. Nevertheless, with this pinhole a nonluminous portion of the Febetron anode was visible on the Febetron target (as shown in Fig. 27). The five channel system is presently being adapted to the Proto I environment; at the time of writing the timing of the channel plate gating circuitry has been synchronized with the Proto I firing.

The resolution of the camera is limited by the size of the pinhole employed when operating in a mode for imagining self-luminous objects. When used in a radiographic mode, the image is generally magnified by a factor of 2 to 4, and the resolution is limited by the source size. As discussed in another section, a source size ~ 0.1 mm has been achieved. This source has been used to radiographically resolve the image of group of 0.13 mm diameter wires magnified by a factor of 4 onto the input channel plate.

Future Plans

The most pressing needs for this system are in developing a more reliable pulse

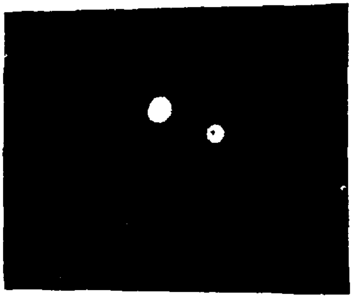

Fig. 27. Tests of imaging system with Febetron (3 ns, 600 kV) using several pinhole sizes. Center 0.031" pinhole; note dark spot in center corresponding the center of anode which does not emit x-rays. Left 0.063" pinhole giving inferior resolution. Other three pinholes were blocked.

monitor circuit (so that the time for each picture can be accurately known) and in tracking down the source of off-axis image distortions. These studies will lead to more manageable camera designs for the large e-beam machines. Also the image resolution will have to be examined on brighter available sources. Finally, the camera system may still be exploited to image UV and neutron emiting sources, as well as time-resolved soft x-ray from the interaction of protons on targets. The latter technique is expected to be of major importance in a thorough diagnosis of the powerful ion beam sources under development.

THE 3 NS PULSED D-T NEUTRON SOURCE

A simple REB diode has been developed to generate ~2 x 10^7 D-T neutrons in 3 ns. The simplicity of this diode design is illustrated schematically in Fig. 21. It consists of three parts: a circulator aperture cathode, a 3/8" rod anode tipped with CD_2 and an erbium tritide target. Electrons emitted from the cathode converge toward the CD_2 anode tip and the resulting anode plasma becomes a rich source of deuterium ions. The diode field accelerates these ions through the cathode aperture to interact with the tritium target, generating D-T neutrons.

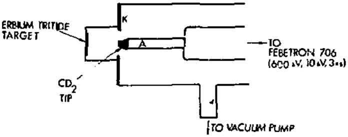

Fig. 28. A schematic of the neutron diode. The erbium tritide target contains ~ 2 Ci of tritium in a 5 μm thick 0.5 inch diameter wafer.

We have found in starting with a new CD_2 tip several shots need to be made before the output can reach ~10^7 neutrons per pulse. A probable cause for this effect is that during the first few shots surface contaminants and surface-absorbed gases are removed raising the deuterium concentration. After several shots, operation stablizes and a rather consistent output of ~10^7 D-T neutrons can be maintained. A new cathode and anode pair can last 50 to 80 shots without requiring breaking vacuum for resurfacing. A typical neutron output pulse as detected by a neutron time-of-flight detector placed 1.5 m away from the diode is shown in Fig. 29. Due to the detector response the neutron pulse FWHM is slightly longer than 3 ns. This 3 ns D-T neutron source has been useful in neutron detector calibration and characterization experiments, as well as in neutron transport experiments; for example, neutron transport through various thicknesses of lead has been examined.

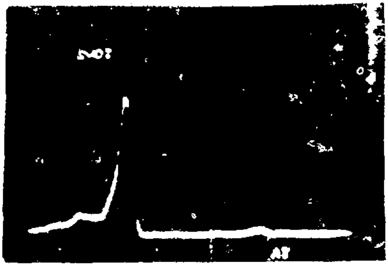

Fig. 29. A typical time-of-flight detector signal. The first (low amplitude) pulse is the x-ray output from the diode. The second pulse is the neutron pulse. The detector is placed 3 m away from the diode. Neutron pulse FWHM is 5.5 ns, which includes the detector response. Horizontal scale is ions/div.

REFERENCES:

1. P. A. Miller, R. I. Butler, M. Cowan, J. R. Freeman, J. W. Poukey, T. P. Wright, and G. Yonas, Phys. Rev. Lett. 39, 92 (1977).
2. P. A. Miller, L. Baker, J. R. Freeman, L. P. Mix, J. W. Poukey, and T. P. Wright, Proc. of 2nd International Topical Conf. on High Power Electron and Ion Beam Res. and Tech., Cornell University, Ithaca, NY, p. 393 (1977).
3. T. P. Wright, "Transport Studies of Cusp and Multichannel REB Fusion Concepts," submitted to J. Appl. Phys.
4. L. P. Mix, Electron Beam Fusion Progress Report - April-September 1977, SAND78-0080, Sandia Laboratories, Albuquerque, NM (April 1978).
5. J. Chang, this semiannual.
6. S. A. Goldstein, Electron Beam Fusion Progress Report - April-September 1977, SAND78-0080, Sandia Laboratories, Albuquerque, NM (April 1978).
7. J. P. VanDevender, Electron Beam Fusion Progress Report - April-September 1977, SAND78-0080, Sandia Laboratories, Albuquerque, NM (April 1978).
8. C. W. Mendel, Jr. and S. A. Goldstein, J. Appl. Phys. 48, 1004 (1977).
9. P. A. Miller, J. W. Poukey, and T. P. Wright, Phys. Rev. Lett. 35, 940 (1975).
10. F. C. Young, J. Golden, and C. A. Kapetanakos, Rev. Sci. Inst. 48, 432 (1977).
11. S. Humphries, Jr., J. Appl. Phys. 47, 2382 (1976).
12. D. Mosher, private communication.
13. C. M. Dozier, D. B. Brown, and L. S. Birks, J. Appl. Phys. 47, 3732 (1976).
14. S. Humphries, Jr., J. Appl. Phys. 49, 2, 501 (1978).
15. S. Humphries, Jr., Proc. of 2nd International Topical Conf. on High Power Electron and Ion Beam Res. and Tech., Cornell University, Ithaca, NY, p. 83 (1977).
16. S. Humphries, Jr. and G. Yonas, Proc. of 3rd International Conf. on Collective Methods of Acceleration, University of California, Irvine, California (1978).
17. J. W. Poukey, and S. Humphries, Jr., submitted to Appl. Phys. Lett.
18. Calculation courtesy of J. R. Freeman.
19. A. Faltens, E. Hartwig, D. Keefe, and W. Salsig, IEEE Trans. Nucl. Sci. NS-20, 1010 (1973).
20. S. Humphries, Jr., Patent Disclosure No. SD-3634.
21. S. Humphries, Jr., and J. J. Ramirez, Patent Disclosure No. SD-3696.

TARGET INTERACTION

OVERVIEW

Experimental target research is directed towards the development of particle beam driven magnetically insulated targets, the study of particle beam-target coupling, and implosion hydrodynamics.

During this reporting period we have strengthened the basis for performing future neutron production experiments with magnetic targets by developing technology to provide high quality targets, and by performing a series of "bench top" experiments to determine the initial conditions of preheat that exist at the time of electron beam irradiation. There is good agreement between the predictive capability of the codes and the experimental preheat measurements.

Implosion physics experiments have been carried out with ablatively driven cylindrical targets on the Hydra accelerator. The effect of shock convergence has been used to obtain uniformly converging implosions with non-uniformly irradiated, shimmed targets.

Development of time resolved neutron diagnostics has continued, and new results have been obtained in measurements of 3 ns DT neutron bursts from a REB pulsed neutron source. Preliminary design studies of a high resolution neutron time-of-flight spectrometer suitable for use on EBFA-I and II has begun.

PREHEATED ELECTRON BEAM TARGET EXPERIMENTS AND SIMULATIONS

Electron beam targets with preheated fuel are being studied as a method of obtaining measurable neutron yields with the accelerators presently available.[1] Two mechanisms are contributing in this approach. First, preheating the fuel to a few eV allows the electron beam driven compression to follow a higher adiabat, and second, the ohmic heating preheat current establishes a magnetic field interior to the target sufficient to reduce electron thermal conduction to the target walls. Experimental and numerical studies have been carried out which simulate the fuel preheating with an 8 kA, 500 ns current pulse. The goal of these studies was to determine the fuel initial conditions for actual compression experiments and simulations.

The numerical studies were made with the CHART B code which is a modified version of Sandia's CHART D model.[2] CHART D is a one-dimensional Lagrangian hydrodynamic code with Saha ionization, material equation of state, and radiation transport. For our purpose, however, the radiation transport is turned off with no loss of accuracy. CHART B adds a number of physical mechanisms of interest to electron beams to this basic code. The major difference is a B_θ magnetic field with convection and diffusion terms and additional terms for a penetrating electron beam. Also added are ohmic heating, $\vec{J} \times \vec{B}$ forces, arbitrary insulator/conductor regions, free-free and free-bound radiation losses, and electron thermal conduction. For the purpose of comparison with spectroscopic measurements the Saha ionization solution is also upgraded with tabulated and analytic partition functions. Typical calculated profiles of temperature and electron density are presented in Fig. 1 at $t = 200$ ns for a discharge in 100 Torr of $D_2 + 10\% \ O_2$. The details of temperature and density for $r \leq 0.2$ mm are dependent upon the intial conditions assumed for the discharge and may not be quantitatively correct. The larger radius behavior is independent of initial conditions and should be accurate. Note also that the spectroscopic measurements referred to as "axial," viewed out to a radius of 0.5 mm and hence up to a temperature $\gtrsim 10$ eV.

In the experimental arrangement an 80 kV Marx bank provided the heating current for a simple cylindrical target filled to a pressure of 30 to 200 Torr of D_2+10%O_2. Spectroscopic access was available as sketched in Fig. 2 both in the transverse and axial direction. Ultraviolet through visible spectra were obtained with a Czerny-Turner spectrograph coupled with an image converter camera operable either in the frame or streak mode. Schlieren photos were made of the plasma expansion using an Argon laser and the image converter in the framing mode, and the results were compared with CHART B calculations. In addition, the target

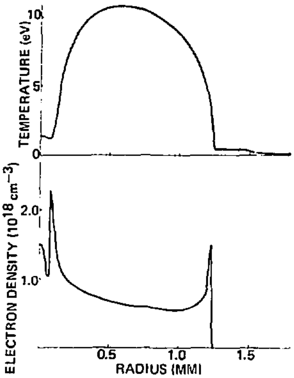

Fig. 1 Calculated Temperature and density profile from CHART B.

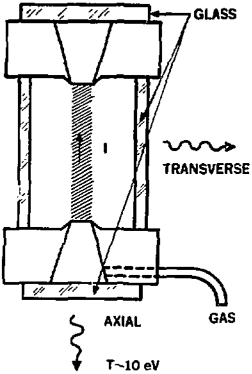

Fig. 2 The cylindrical discharge cell for spectroscopic measurements.

voltage drop and current were monitored current viewing resistor, respectively. In the following, the Schlieren photography will be compared with CHART B to establish that theory and experiment are in agreement with respect to the easily observed hydrodynamics of plasma expansion. Then the axial spectroscopy data will be presented to support the calculated ~ 10 eV peak temperature. Finaly, the transverse spectral analysis is given to discuss the difficulties in making meaningful temperature measurements via the line ratio method in spatially inhomogeneous plasmas.

The Schlieren photography system shown in Fig. 3 consisted of a cw Argon-ion laser, an enlarging lens, a spatial filter to block out light not refracted by the plasma, a laser line filter time-staggered mechanical shutters, and a fast framing camera. A typical sequence of frames of the cylindrically expanding plasma is given in the inset. In Fig. 4 the computed and measured (power law fit to the data) expansions are compared for 100 The agreement is more than sufficient to justify acceptance of CHART B as modelling

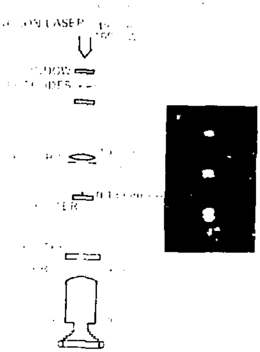

Fig. 3 Schlieren photography system. The inset shows 3 frames from a discharge in 100 Torr of air at t = 70, 250, and 350 ns.

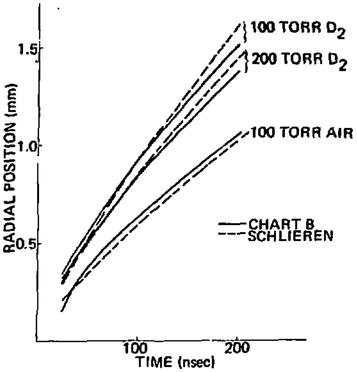

Fig. 4 Schlieren data and CHART B position of $\partial Ne/\partial r$ maximum for various gas fills. A linear fit to the data can also be made and when extrapolated to t = 0 gives an initial radius for CHART B.

this experiment. The bulk of the effort has accordingly been concerned with measuring the peak temperature of ~10 eV predicted by CHART B.

The axial spectra lend support to the predicted temperature by observation, in the streaking mode, of the NV (460 and 462 nm) and OVI (381 and 383 nm) lines where 10% of N_2 or O_2 is added to 100 Torr of D_2. At the 10^{18} cm^{-3} electron densities of these plasmas the NV and OVI line emissions will peak and then decrease as the temperature exceeds 8.4 or 11.7 eV, respectively. The temporal NV and OVI data in Fig. 5 shows the NV emission peaking and then falling off as the OVI is still increasing. The NV behavior gives $T \gtrsim 9.5$ eV. A CHART B calculation of the OVI emission as it would be viewed experimentally is also given for comparison of timing; the main peak is in good temporal agreement. (The initial peak is sensitive to the initial discharge configuration and may not be physically relevant.) Experiments were performed at higher current and/or smaller diameter which should have yielded temperatures high enough to cut off the OVI lines; where a sizable effect was expected the continuum intensity increased to the point of obscuring the OVI lines. We conclude that the measured $T \gtrsim 9.5$ eV is consistent with 10 eV CHART B predictions.

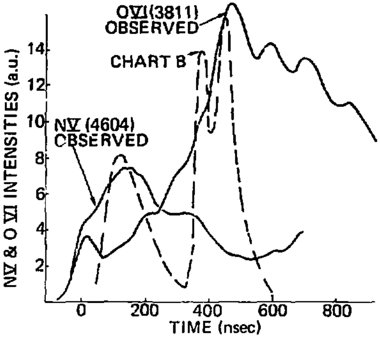

Fig. 5 Observation of NV and OVI lines compared to CHART B calculation of the OVI line.

The electron density assumed above, 10^{18} cm^{-3}, is a typical value from calculations and also supported by measurements. The plasma density has been observed in Stark broadening of the D_α and D_β lines in pure D_2 discharges. The D_α and D_β emission can be shown to peak in a region of ≈ 1.5 eV temperature on the outside of the expanding plasma where the temperature is falling quickly and the electron density has a sharp peak of 1 - 2 x 10^{18} cm^{-3}. Observed density of 0.8 x 10^{18} cm^{-3} from D_α broadening is in fair agreement with these peak values.

A final investigation involving radial spectroscopic measurement of temperature in these inhomogeneous plasmas will be summarized mainly as an illustration of difficulties therein. On the initial premise before calculation, that temperatures of a few eV would be observed, we measured a line ratio for OIII (326.5 nm)/ OII (340.7 nm) which gave T ~ 4 eV. CHART B calculations revised the expected temperature upward and due to the abundancy of oxygen spectra in the ultraviolet, the same measurement became a line ratio of OIII (326.5)/ OII + OIV (340.3 to 341.1) . Furthermore, the sharp temperature fall-off in Fig. 1 indicates that OII, OIII, and OIV were each emitting from regions of differing temperatures. In an attempt to salvage the measured ratios, we calculated an integrated OIII/ O (II + IV) ratio in CHART B to simulate the observation. These line ratios are compared in Fig. 6 for a pressure of 30 Torr (D_2 + 10% 0^2) where the continuum emission is low, allowing accurate ratios to be found. This apparent disagreement is attributed to (a) the strong temperature sensitivity of line ratio methods and (b) the expected strong temperature variation at the edge of the plasma where OII - OIV emission originates.

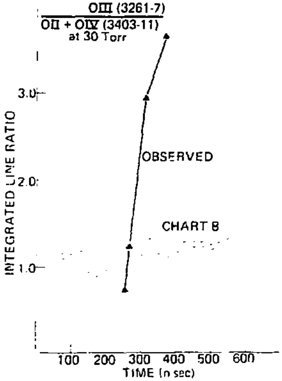

Fig. 6 Simulated and observed OII/ (OII + OIV) have ratio for discharge in 30 Torr of D_2 + 10% O_2.

That the OIII/(OII and/or OIV) emissions were not coming from the same spatial regions was further seen in analysis of Abel-inverted, spatially resolved spectra. (Spectrograph slit transverse to cylinder axis, image converter in framing mode, and source imaged onto the input slit.) The spatial distributions of the respective intensities are shown in Fig. 7. The OIII shows a hollow center after inversion because it originated in a well-defined zone, the combined OII + OIV did not invert to a hollow center because the two emitting regions and marginal spatial resolution did not result in a well-defined emission layer. These results are consistent with a central T ≥ 6 eV to provide an interior source of OIV. As previously discussed, observation of NV and OVI raises this estimate to T ≥ 9.5 eV, and also eliminates pathological configurations such as cold OII-emitting core and warm OIII-emitting exterior sheath.

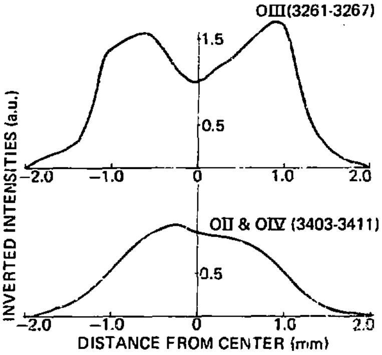

Fig. 7 Abel-inverted oxygen spectra obtain from transverse framing experiment. Spatial resolution has 0.1-0.2 mm.

The present conclusions of these experimental and numerical studies of fuel preheat are that (1) through detailed experimental and numerical comparisons we have arrived at a valid model for fuel preheating by an external driver in the 8 kA range and (2) we can model the initial conditions for actual compression experiments with increased certainty.

MAGNETICALLY INSULATED ("ϕ") TARGET FABRICATION

Progress has been made in developing the technology for target fabrication with dielectric materials. The requirements for uniform (within a few percent) low Z dielectric spheres from 3 to 7 mm in diameter are nearing realization with two approaches (parylene and polyimide). We expect that during the next six months we will be able to make the decision on the best approach for subsequent fabrication. In the interim, we plan to conduct a series of experiments with targets fabricated by joining molded hemishells of polystyrene.

Recently, several molded targets have been fabricated and tested for helium diffusion. The first sign of gas permeation took 15 seconds, and is expected to be longer for D_2 or T_2. It will be possible for us to fill such targets mounted in place in the diode within seconds of diode firing without risk of preshot contamination of the diode. Gas handling apparatus to do this remotely is currently under construction.

In the long term, we will require higher Z shells for use as ablative pushers. A recent development at LASL, the ability to evaporatively coat a high Z glass upon a substrate appears to have high potential for this application; the data base is presently too limited to assess this technique.

Parylene

Recently, the parylene conformal coating process has been used to fabricate seamless non-conducting hollow spheres. In this report, the parylene conformal coating process will be briefly described and the results of the characterization measurements will be discussed. The first actual targets fabricated with this technology will be available during the next several months.

The parylene conformal coating process a process patented by Union Carbide since 1971, consists of heat dissociation of the parylene dimmer into monomers which in turn polymerize on the surfaces to be coated. The resulting coating exhibits a high degree of uniformity, low rates of gas permeation, low reactivity to most aqueous solutions including acids, and high voltage breakdown strength. In forming hollow seamless spheres, we used the method of coating a leachable mandrel. A few of the initial 50 parts were sectioned and leached; measurements are discussed below.

Figure 8 shows a collection of parylene coated mandrels at high magnification. Two randomly selected targets were sectioned; Fig. 9 shows their cross sections. The targets were first painted with a thin coat of silver paint to provide higher contrast and then

Fig. 8 Parylene coated parts. A at *10X magnification and B at* 20X magnification.

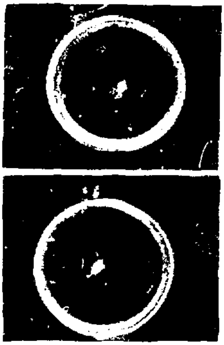

Fig. 9 Cross sections of two parylene coated mandrels at 20X magnification. Note the steady variation in coating thickness from one side of the sphere to the other side.

potted in epoxy. After curing the potted targets were cut, ground, and polished to the mid-plane of the mandrel. As shown in Fig. 9, the outer most layer is the parylene coating and the innermost region is the brass spherical mandrel. Variation in both I.D. and O.D. is better than 1 percent and in wall thickness are caused by the revolution of the mandrels in the parylene atmosphere during the coating process, which results in a faster coating rate for the leading edge and a corresponding slower rate for the trailing edge. This uneven coating rate has been corrected by changing the direction of revolution periodically.

The outside surface finish is shown in Fig. 10 with a considerable number of surface blemishes. The causes of these blemishes can probably be traced to dust, surface cleanliness, and coating rate. In discussions with researchers at NASA Lewis, LLL, Union Carbide Crystal Division, and Bendix, many remedies were suggested and the overall consensus is the surface finish can be improved. The inside surface mirrors the mandrel surface finish which is 8 microinches.

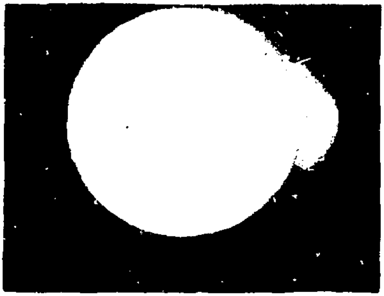

Fig. 10 A parylene hollow sphere at 20X magnification. The mandrel has been leached out.

A target with the mandrel leached out was used for leak testing and was found to be leak tight, and the dimensions were within the specifications of exploding pusher targets.

Polyimide

The polyimide target fabrication utilizes the method of rotational casting. The mandrels are rotated simultaneously about two axis and the material is sprayed and cured in alternate cycles. Outer surface finishes of 4000 Å, far in excess of requirements for exploding pushers, have been obtained. Wall non-uniformity of $\sim$ 20 percent is excessive; modifications of the spray system to employ four nozzles instead of one is expected to produce very uniform wall thickness. The selection of the best mandrel material, which must start with high uniformity, not interact with the raw polyimide, and be removable with an agent compatible with the polyimide must be made. Assuming such a material can be found, this process may produce pellets without the surface blemishes characteristic of the parylene used thus far.

IMPLOSIONS PHYSICS

Nuckolls et al.,[3] have recently considered several inertial confinement fusion (ICF) target designs which may be capable of achieving high gain and thus, reduce the power and energy conversion efficiency requirements of ICF drivers. The ablator-pusher concept inherent in these high-gain designs requires that the implosion be spherically symmetric to within a few percent. It was claimed in Ref. 1 that implosions with the required symmetry can be theoretically achieved by use of multiple beam irradiation, hot electron transport in the low density ablation atmosphere and, if necessary, the introduction of non-spherical variations in the shell radius and thickness during fabrication (shimming).

We have obtained experimental results demonstrating that a simple shimming technique for ablatively driven targets is capable of drastically *improving the implosion symmetry of a* target which is nonuniformly irradiated by a single electron beam. The Hydra relativistic electron beam accelerator[4] was employed for single beam irradiation[5] *of a specially designed cylindrical* target anode assembly, and multiple pulse holographic interferometry[6] was used to observe the implosion of the cylindrical target.

The Hydra electron accelerator, nominal characteristics 1 MeV, 350 kA, and 100 ns pulse duration, is presently being utilized to investigate the physics of ablatively driven implosions. Experiments are being conducted to investigate the stability of fusion targets, focusing of strong shock waves, equations-of-state of materials at high pressures (~ 1 TPa) and interaction of shock waves at material boundaries. In order to accomplish these goals, several target-diode configurations have been developed. Criteria selected for these configurations are two fold: (1) the targets must be designed so that the hydro-dynamic response is convergent, i.e., the geometry of the ablator-pusher system is at least quasi-spherical; (2) the implosion process itself must be accessible to optical diagnostics. These criteria impose constraints upon the allowable target geometries. In essence, the target configurations must be open, converging systems. Cylindrical shells have been chosen for these investigations, and a 4-pulse holographic interferometer was used to study the implosions.[7] Preliminary results with hemi-spherical targets has been presented elsewhere.[8]

In these experiments, the target cylinders were made of brass ($\rho = 8.5\ \mathrm{g/cm^3}$). For cylindrical shells with concentric inner and outer surfaces, the targets were obtained from extruded brass tubing. Cylindrical targets with eccentric inner and outer surfaces were fabricated by means of a gun-boring technique. Solid rods of brass were bored out along their axes, but the centers of the hollowed-out sections were displaced by an arbitrary amount from the geometric axis of symmetry of the outer surface. Targets fashioned in this manner had inner surfaces with smoothness of ~ *1300* .

The rationale for these eccentric (shimmed) targets is, of course, based upon the experimental observation that the deposi*tion loading on a symmetric target is* non-uniform. A measure of the deposition symmetry can be established by the velocity of the ablation layer. In our diode configuration, the 4-pulse holography system was used to *determine the angular dependence* of the ablation velocity. In general, because of limited field of view, it was often impossible to obtain simultaneous (same shot) information on both implosion and ablation velocity. For the present, data power depositions in the range 1-2 TW/g were inferred.

It is clearly seen from the holograms of Fig. 11 that the implosion proceeds in an asymmetric fashion. This set of holograms shows the late phase of the implosion where jetting occurs within the convergence volume. The implosion velocity from the high deposition side was determined to be about 0.5 cm/μs.

The shock velocity and pressure in the brass can be estimated as follows: if one uses the empirical equation-of-state for brass[9] connecting the shock and particle velocities, i.e.,

$$u_s = a + b\,u_p \qquad (1)$$

where a = 0.37 cm/μs and b = 1.43 and if one assumes that $u_p = u_{fs}/2$; then the shock velocity in the brass is 0.73 cm/μs. From conservation of momentum, the pressure in the brass can be estimated, i.e.,

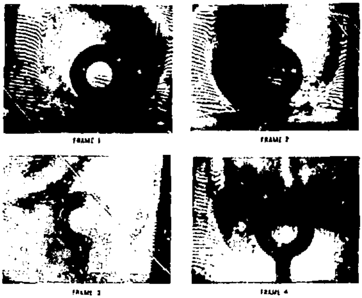

Fig. 11 Hologram sequence showing the implosion (and ablation) of a concentric cylindrical brass target. The interframe time is 27 ns, and the duration of a frame is 3 ns. This sequence clearly shows the asymmetric irradiation and subsequent jetting of material within the convergence volume. Time increases the way a book reads.

$$p = \rho_0 \, u_s \, u_p = 1.3 \text{ Mbar.} \qquad (2)$$

At this pressure, the interior surface of cylinder, upon isentropic release to zero pressure, is calculated to be near the melt temperature (~ 850° C) of the brass.

In Fig. 12 are shown holographic interferograms of the implosion sequence for an eccentric (shim) cylinder. The offset of the bored out region was 0.04 cm. One notes that the implosion proceeds initially from the low deposition (anode) side of the cylinder and the implosion velocity from that side is approximately 0.6 cm/μs. In the third hologram of the sequence there is a slight distortion of the reference fringes on the high deposition (cathode) side, and the fourth hologram indicates that material has rapidly imploded with a velocity of resultant convergence volume at that time is seen to be approximately spherically symmetric.

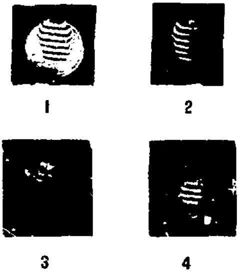

Fig. 12 Hologram sequence showing the implosion of an eccentric (offset) cylindrical brass target. The ablation region was blocked off in order to improve the contrast of the pictures. This sequence shows the implosion proceeding initially from the low deposition side and later from the high deposition side. The interframe time is 27 ns. Time increases the way a book reads.

An explanation of these phenomena proceeds as follows: first, we consider the implications of the high free surface velocity (1.8 cm/μs) observed in the data. If one employs the assumption that the free surface velocity u_{fs} is twice the particle velocity u_p, then the equation-of-state implies a peak pressure in the brass of about 13 Mbar. However, equation-of-state data for brass obtained by McQueen et al.,[9] indicates that such an assumption will be in considerable error at these pressure levels. Their data do not exceed P = 1.764 Mbar where the value of u_{fs} exceeds that of $2\,u_p$ by less than 5 percent. If one linearly extrapolates the McQueen data, $(u_{fs} - 2\,u_p)/2u_p$ vs pressure, one can by iteration find Hugoniot parameters which are mutually self-consistent. For the observed u_{fs} = 1.8 cm/μs one finds that a consistent set are u_p = 0.74 cm/μs, u_s = 1.44 cm/μs and p = 9 Mbar.

In the present experiment, the inferred pressure of 9 Mbar and shock velocity of 1.44 cm/μs can only be explained by radial convergence and shock focusing.

If one were to assume that such pressures were achieved only by electron energy deposition, then the shock velocity on the "hot" side is too high to agree with the observed implosion sequence. In other words, material from the hot side would always arrive earlier at the center of the cylinder - contrary to observations. Previous experiments[8] with Hydra have shown that ultra-high pressures (10-20 Mbar) are achieved by means of shock-focusing in hemispherical configurations. In fact, the high pressures (and high shock velocities) rise extremely rapidly near the curved inner boundary of the material. Such convergence effects can qualitatively explain the implosion sequence observed in this experiment.

The consequences of these results for inertial confinement fusion are the following: in order to minimize the power and energy requirements for the driver (E-beam, ion or laser) it is necessary to investigate the potential use of high-gain pellet designs. These pellets will very likely employ multiple shells where high densities are obtainable by hydrodynamic compression. The presence of loading and implosion asymmetries may seriously degrade the quality of hydrodynamic compression. We have shown in these experiments that if sufficient care is taken in target design and fabrication, then deleterious effects of these phenomena can be minimized.

SCINTILLATOR-PHOTOMULTIPLIER RESPONSE TO A SIMULATED REB GENERATED DT THERMONUCLEAR NEUTRON PULSE

The April-September 1977 semi-annual report[10] presented measurements of the DD thermonuclear neutron signature. During the present period, the diode of the Febetron Model 706 used to produce the 3 ns DD neutron bursts of Ref. 1 has been modified so as to produce 3 ns DT neutron bursts with total yields as high as 2 x 10^7. With this source, the DT thermonuclear neutron signature as detected on fast plastic scintillator-photomultiplier combinations (SPM) has been measured.

DT Thermonuclear Neutron-Signature

The neutron total yield was monitored by a standard silver activation counter[11] and by a lead activation counter.[12] The SPM detector used was a EGG NPM-54.[13]

As an example of SPM response, Fig. 13 shows three DT neutron pulses detected through 1.9 cm, 10.2 cm and 20.3 cm of lead shielding. The NPM-54 SPM has a rise time of 2.2 ns, and a FWHM response of 3.5 ns when used to observe a single instantaneous event such as a cosmic ray. In Fig. 13a, the prompt x-ray bremsstrahlung pulse of the Febetron as well as the neutron burst is observed through 1.9 cm of lead at a distance of 3 m. The neutron time-of-flight from this trace is 19.5 ns/m consistent with 14.1 MeV DT neutrons. The neutron pulse has a rise time of < 3 ns and a FWHM of about 6.0 ns. In Fig. 13b, the x-ray bremsstrahlung pulse is completely attenuated by the 10.2 cm of lead, and the neutron pulse is observed to have a 3.5 ns rise time and a FWHM of approximately 6.0 ns. In Fig. 13c, the neutron pulse is observed to have a 3.5 ns rise time and a FWHM of approximately 6.0 ns when detected through 20.3 cm of lead. It is seen that in all cases the DT neutron pulses have very fast rise times, narrow FWHM widths, and that tails are introduced on the pulses by the various thicknesses of lead shielding. These pulse shapes are in agreement with pulse shapes predicted by neutron Monte Carlo calculations to be presented in the next section.

The thermonuclear neutron "signature" has been established using a fast plastic scintillator-photomultiplier combination shielded by several cm of lead in conjunction with a 3 ns wide neutron source which directly simulates the expected DT thermonuclear neutron pulse from a REB imploded target. The DT thermonuclear neutron pulse shape is found to have a sharp leading edge of < 3.5 ns, a narrow FWHM of some 6.0 ns, and a tail that can extend to 40 ns.

Fig. 13 Oscilloscope traces comparing neutron scintillator photomultiplier detector response to a 3 ns wide DT neutron pulse when the neutron pulse is detected through 1.9, 10.2, and 20.3 cm of lead shielding.

(a) 5.0 volts/div, 10 ns/div
The detector was shielded by 1.9 cm of lead and the total neutron yield was 2.4 x 10^7. Note the prompt x-ray pulse.

(b) 5.0 volts/div, 20 ns/div
The detector was shielded by 10.2 cm of lead and the total yield was 6.3 x 10^6. The lead shielding completely attenuated the x-ray pulse.

(c) 5.0 volts/div, 20 ns
The detector was shielded by 20.3 cm of lead and the total yield was 8.5 x 10^6. Once again, the lead shielding completely attenuated the x-ray pulse.

Monte Carlo Neutron Transport Scintillator Response Calculations

Monte Carlo neutron transport calculations similar to those reported in the October 1976 through March 1977 semi-annual report[14] have been carried out to predict the DD and DT response of a plastic scintillator shielded by as much as 30.5 cm of lead. Figures 14 and 15 show calculations which used square wave sources of 2.45 MeV and 14.1 MeV neutrons, 3 ns wide in time located at a distance of 350 cm from the scintillator. Calculations were performed for 0.0 cm, 10.2 cm, 20.3 cm, and 30.5 cm thicknesses of Pb shielding and a 5.6 cm x 6.7 cm diameter cylindrical plastic scintillator. A sharp leading edge response is found for lead shielding thickness of up to 30.5 cm. In agreement

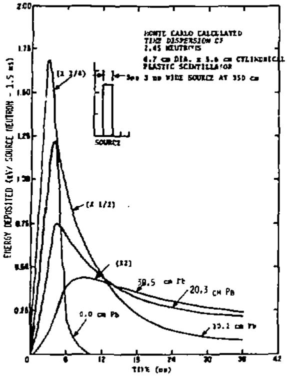

Fig. 14 *Monte Carlo calculated time dispersion* of 2.45 MeV neutrons incident on a 5.6 x 6.7 cm diameter cylindrical plastic scintillator through 0.0 cm, 10.2 cm, 20.0 and 30.5 cm thicknesses of lead shields. The source was 3 nsec wide and located 350 cm from the scintillator.

with experiment (see previous section), the major effect of the lead is to disperse and shape the pulse in time while attenuating the leading edge.

Monte Carlo Neutron Spectrometer Calculations

The yield and energy distributions of the neutrons that are emitted from a electron beam or ion beam driven pellet containing a mixture of deuterium and tritium gases provide a signature of the reacting ions. They contain information about the plasma density, temperatures, and the mechanism of the reactions. X-ray emission from the fuel, which in principle might provide data about the reactants, is masked by radiations from the high Z materials used to construct the shell of the target. Furthermore, unlike the α-particle distribution, the neutron energy distribution is virtually unperturbed by neutron passage through either the compressed gas or the pellet shell. Consequently, the measurement of the DT reaction neutron energy distribution is an important and powerful diagnostic of target performance.

The plasma ion temperature may be measured by neutron time-of-flight since the plasma generated in a REB imploded pellet provides an excellent temporal and spatial "point" source of neutrons. By measuring the "neutron line width" ΔE, the DT ion temperature θ_i may be extracted from the relationship[15]

$$\Delta E = 177\sqrt{\theta_i},\ \theta_i \text{ in keV}\ . \qquad (1)$$

This relationship also implies that neutron energy resolutions of the order of 25 to 65 keV are required with correspondingly large neutron flight paths of some 45.0 to 125.0 m.

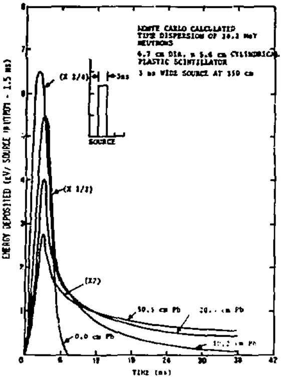

Fig. 15 Monte Carlo calculated time dispersion of 14.1 MeV neutrons incident on a 5.6 cm x 6.7 cm diameter cylindrical plastic scintillator through 0.0 cm, 10.2 cm, 20.0 and 30.5 cm thicknesses of lead shielding. The source was 3 nsec wide and

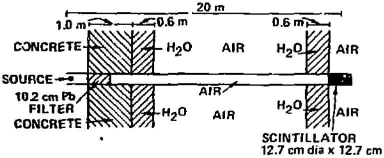

Fig. 16 Neutron time-of-flight spectrometer used in the Monte Carlo calculations described in the text.

Keeping the above requirements in mind, preliminary design studies of a high resolution neutron time-of-flight spectrometer suitable for use on the EBFA-I and EBFA-II relativistic electron beam accelerators has begun. In these design studies the neutron Monte Carlo code SORS[16] is being used. The spectrometer being modeled is shown in Fig. 16. The spectrometer's length is kept at 20 m so that good neutron statistics are obtained for modest amounts of computer time. As our design study advances, longer spectrometer systems will be modeled. An important question to be answered by this study is whether the neutron pulse width will be modified by the use of high Z lead filters in the neutron flight path. These lead filters will probably be necessary to attenuate the intense bremsstrahlung burst of the EBFA generation of accelerators, such that the neutron time-of-flight detectors will not saturate. The first result of these calculations is shown in Fig. 17 for a 3 ns wide neutron pulse. The Monte Carlo predicted neutron pulse has a 3.9 ns FWHM width in agreement with a expected pulse width of 3.9 ns found by adding in quadrature the 3.00 ns pulse width of the source with a time dispersion of 2.47 ns due to neutrons interacting throughout the entire length of the 12.7 cm scintillator. Consequently the high Z lead filter does not seem to affect the width of the neutron pulse. Further calculations are presently being carried out.

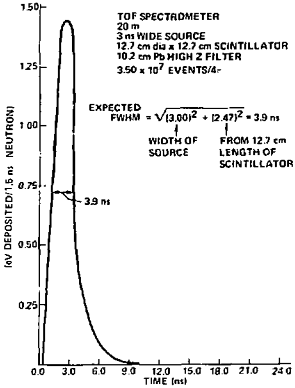

Fig. 17 The Monte Carlo predicted neutron pulse.

REFERENCES

1. J. Chang, M. M. Widner, A. V. Farnsworth, et al., "Neutron Production from Advanced REB Fusion Targets," Proc. 2nd Int'l Topical Conf., Cornell University, Ithaca, NY, Oct. 3-5, 1977.
2. S. L. Thompson, "Improvement in the CHART-D Radiation-Hydrodynamic Code II," Sandia Labs. Report SC-RR-71-0713, 1971.
3. J. H. Nuckolls, R. O. Baugerter, J. D. Lindl, W. C. Mead and Y. L. Pan, "High Performance Inertial Fusion Targets," Lawrence Livermore Laboratory, paper presented at the European Conference on Laser Interaction with Matter, Oxford, England, Sept. 19-23, 1977.
4. G. H. Martin, IEEE Trans. Nucl. Sci. NS-20, 289 (1973).
5. J. Chang, M. M. Widner, G. W. Kuswa and G. Yonas, Phys. Rev. Lett. 34, 1266 (1975).
6. L. P. Mix and R. W. Kessler, Sandia Report, SAND 77-0209, March 1977.
7. M. J. Clauser, S. A. Goldstein, R. J. Leeper, C. W. Mendel, L. P. Mix, J.N.Olsen, F. C. Perry, and A. J. Toepfer, Eighth European Conference on Controlled Fusion and Plasma Physics, Prague, Czechoslovakia, Sept. 19-23, 1977, p. 245.
8. L. Baker, M. J. Clauser, J. R. Freeman, L. P. Mix, J. N. Olsen, F. C. Perry, A. J. Toepfer and M. M. Widner, Proceedings of the 2nd International Topical Conference on High Power Electron and Ion Beam Research and Technology, Cornell University, Oct. 3-5, 1977, p. 169.
9. R. G. McQueen and S. P. Marsh, J. Appl. Phys. 31, 1253 (1960).
10. The April-Sept. 1977 semi-annual report, SAND 78-0080, April 1978.
11. R. J. Lanter and D. E. Bannerman, Los Alamos Report LA-3498-MS, (1966).
12. C. E. Spencer and E. L. Jacobs, IEEE Trans. on Nucl. Sci. NS-12, 407 (1965).
13. Available from EG&G Inc.-Las Vegas, Nevada.
14. Oct. 1976 to March 1977 semi-annual report, SAND 77-1414, October 1977.
15. H. Brysk, Plasma Phys. 15, 611 (1973).
16. J. Kimlinger and E. F. Plechaty, Lawrence Livermore Laboratory Report UCRL-50532, October 1968.

APPLICATIONS

REP-RATE PULSE POWER TECHNOLOGY

Overview

Inertial confinement fusion reactors will require efficient, high-average power drivers constructed with reliable, long lasting components. Reliable, repetitively operated drivers will be needed for test facilities (such as system integration facilities and material test facilities) long before a demonstration power plant is developed. A research program to establish the pulse power technology base that will be required to design and successfully put into operation these drivers is underway on a limited basis at Sandia Laboratories. Reactor systems will require 1-5 MJ of particle beam or laser energy to be deposited in the fuel pellets 1-10 times per second.[1] A reactor system is expected to consist of 20-60 modules with about 50 kJ of energy delivered to the target in less than 10 ns from each module. Since drivers with 1-40 percent efficiency are being considered, the pulse power energy storage requirements vary from 0.25-5 MJ for each module. Table I indicates system lifetimes for three types of reactors that will be developed before ICF reactors can become commercially feasible. Therefore, an ICF driver module will have a 2.5-50 MW pulse power energy storage capability and a system lifetime of 10^7-10^{10} pulses.

TABLE I

Reactor System Lifetimes

	f	R pps	Life yrs	P.A.	System Life Pulses
Experimental Power Reactor	1.0	1-10	3	.2	10^7 - 10^8
Demonstration Power Plant	.25	1-10	5	.7	10^8 - 10^9
Commercial Power Plant	0.1	1-10	30	.7	10^9 - 10^{10}

(P.A. is the plant availability factor)

The most efficient driver is the pulse power driver electron or light ion beam accelerators. The efficiency of the energy transfer steps for a typical 50 kJ module is outlined in Table II. The 350 kV, 300 J, 100 pps, 30 kW average power test facility (RTF-I)[2,3] that was designed and is being used extensively in this program represents the present state of the art for such repetitively operated drivers. Therefore, the average power, peak power and beam energy must be increased above the present state of the art by 40, 400 and 170 respectively to achieve the desired parameters for a single reactor module and at least 20 modules will be required for a reactor. Successful development of these systems will require extensive research at each step in the energy transfer process.

TABLE II

Particle Beam Module Efficiency

COMPONENTS	EFFICIENCY	ENERGY (kJ)	COMMENT
Capacitor Bank ↓ Transformer ↓ PFL	0.9	122 110	With dual resonant charging, .9+ efficiency has been measured for 300 J system.[4]
PFL ↓ Vacuum Transmission Line	0.9	110 99	Losses are energy dissipated in the switches and reflected energy during the pulse risetime.
Vacuum Transmission Line ↓ Diode	0.9	99 89	[illegible] percent efficiency has been measured for a [illegible] m long, 1.1 TW, [illegible] transmission line.[5]
Diode ↓ Beam	[illegible]	89 71	This efficiency reflects losses during pinching of the electron beam or focusing of the ion beam. More than [illegible] percent of the current has been extracted in a few mm diameter electron beam & ion pinching occurs (60 percent of the total diode energy was extracted).[5] With [illegible] percent of the diode energy has been focused within the diode[6] and it is expected that this value can be extracted in a beam.
Beam ↓ Target	[illegible]	71 50	Beam propagation, beam overlapping and beam absorption efficiency are assumed to be 0.7. A 370 kA electron beam has been propagated 1 m with 90 percent efficiency. Initial calculations indicate that if the appropriate channel conditions (high conductivity with [illegible] kA of channel current) can be achieved propagation from over a few meters for either electrons or ions [illegible] is possible. Beam overlapping[8] and absorption are being vigorously investigated at this time. Light ions pose fewer problems in this area than electrons.

During this period, a new data acquisition system has been placed in operation for the RTF-I facility. This system has been used to establish the breakdown voltage distribution as a function of gas flow rate for the 700 kV, two electrode spark gap. Electrode erosion data has been collected for all three spark gaps in this system with up to 10^6 pulses in a continuous run. Development of high voltage transformers and low loss Marx generators are continuing efforts.

RTF-I, 300 J, 100 pps TEST FACILITY EXPERIMENTS

Data Acquisition System For RTF-I

A computer based data acquisition system has been developed for the 700 kV, 100 pps test facility (RTF-I). Incoming data are analyzed as received to provide a real time monitor of system performance. A CRT display of selected data is available. The same data are optionally stored on magnetic tape for subsequent off line processing. Provision has been made to implement partial control of the facility by the computer if that becomes desirable.

The data acquisition system is based on CAMAC; an internationnaly adopted set of conventions for the handling of data in computer based systems. Prior to the adoption of standards like CAMAC, the addition of a computer to an experiment typically involved development of two units. An input module was needed to convert experimental signals, which are almost always analog, to a digital format. A second module, the interface, was needed to transfer these digital data to the computer. Generally the addition of a second input module required building a second interface. CAMAC circumvents this by standardizing the communication between the input units and the interface. Thus any CAMAC interface can work with any CAMAC input module through what is effectively a standard language. The wide variety of *commercially available CAMAC input* modules simplifies implementation of a wide variety of monitoring functions.

RTF-I, as is shown schematically in Fig. 1, is a transformer driven 700 kV pulser which operates repetitively at frequencies up to 100 Hz.[2,3] A single cycle is initiated by closing triggered spark gap S_1 to discharge capacitor C_1 (1.5 μF, 21 kV) through the primary L_p of an impulse transformer. A dual resonance discharge which produces the voltage waveform of Fig. 2 is used because all of the energy stored in C_1 less small resistive losses can be transferred to C_2 at the peak of the negative voltage excursion. The

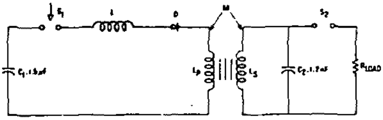

Fig. 1. RTF-I, a 350 kV, 100 pps test facility.

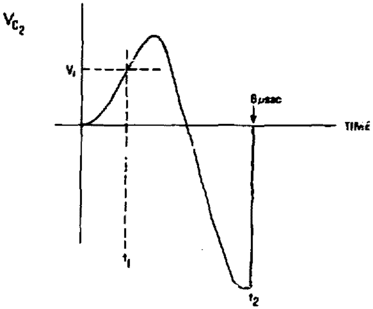

Fig. 2. PFL voltage waveform.

transformer charges a 1.5 nF oil pulse forming transmission line (PFL) which is shown in Fig. 1 as capacitor C_2. When untriggered spark gap switch S_2 closes, a 350 kV, 30 ns pulse is delivered into a matched load resistor, R_{LOAD}.

The philosophy used to construct a monitor for RTF-I is that a few digital words per event can be accumulated to form statistical ensembles which characterize system performance. Analog-to-digital converters (ADC's) and time-to-digital converters (TDC's) sample probe waveforms from RTF-I to produce these digital words then signal the CAMAC interface that an event has occurred.

Upon receipt of these event signals the interface, a microcomputer, goes into a loop in which it reads from a list in its own memory the commands required to read out the data stored in each input module and clear it in preparation for the next event. Most CAMAC modules actually generate several data words per event making use of a CAMAC language feature that the command to read the second word from a module is simply the command to read the first word incremented by one. Thus to read the eight words stored in an octal TDC, the interface fetches from its memory the command to read the first word and the number of words in the module, e.g., eight. It reads successive words by issuing the read command then incrementing the command by one, eight times. To add a second TDC to the system a second read command is stored in the interface memory and a second eight. Also the total number of words per event counter is increased by eight, a trivial software modification.

Each word from the input modules is immediately stored in an input data buffer in the computer memory by the interface. The main computer processor is not involved in the transfer leaving it free to analyze the incoming data. The interface keeps a count of data transferred and when the available buffer of the main computer is full it interrupts the computer, resets itself, and goes into a wait state.

In response to an interrupt the computer transfers the experimental data to an analysis buffer then disables the transfer code for as long as is required to save the data on magnetic tape, if this option is selected. The interface is released from its wait state and allowed to fill the input buffer but the analysis buffer is protected until it has been saved. Simultaneously the computer proceeds to analyze the data currently in the analysis buffer and display the results as instructed by the operator.

The procedure used to monitor the stability of the breakdown of switch S_2 in time is illustrated in Fig. 3. Discriminator D_1 produces an output when the output of a voltage probe across C_2 crosses a preset voltage level V_1 at time t_1 (see Fig. 2). This voltage level is selected to be above the switching noise generated by S_1 near $t = 0$. The output of D_1 starts the time digitizer (TDC). The voltage waveform on C_2 is also differentiated and the rapid change in slope when switch S_2 closes at time t_2 is detected by discriminator D_2 which produces a TDC stop signal. The TDC produces a digital output proportional to the time between the start and stop inputs, with a least count corresponding to 10 ns. The computer then generates histograms of these switch breakdown times according to operator instructions.

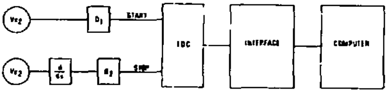

Fig. 3. High voltage switch breakdown time monitor procedure.

High Voltage Spark Gap Stability Experiment

A series of histograms showing the increase in the breakdown stability of the 700 kV, two electrode switch (represented by S_2 in Fig. 1 and sketched in Fig. 6) with an increase in the rate at which gas is flowed through S_2 is shown in Fig. 4. Gas flow is needed to purge S_2, that is to rebuild its dielectric strength after a breakdown. If insufficient gas is supplied, premature breakdowns occur and the histogram contains events at early times. At high flow rates the distribution becomes symmetric. approximately Gaussian. Fig. 4 shows the root mean square (rms) deviation of the time distribution about its mean as a function of gas flow rate. Note the decrease with increased flow to what appears to be a constant value at the higher gas flow rates. The minimum rms deviation is typically 30 ns for a total waveform duration of 6 μs or about 0.5 percent. This compares to 12 ns for a 2 μs dual resonance waveform (0.6 percent) for data taken at 1 pps with UV preionization. These latter data were taken on the REPIT facility[3] earlier this year.

The output switch should be operated with a flow rate corresponding to the minimum rms deviation. The required flow depends on the voltage on C_2 and may depend on the current drawn after S_2 closes. Experiments to characterize these dependencies are in progress.

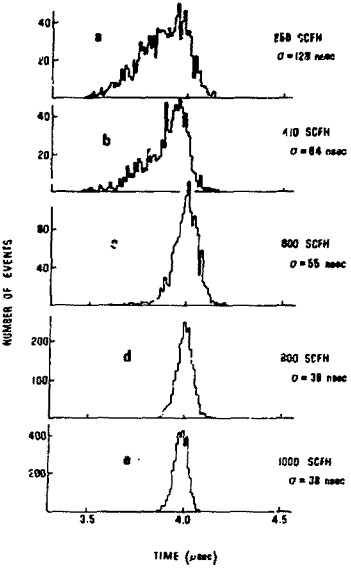

Fig. 4. Histograms of 700 kV spark gap breakdown times as a function of gas flow rate.

Spark Gap Electrode Erosion Experiments

A one million shot continuous test run was made on RTF-I to demonstrate overall system endurance and to measure the erosion rate on the spark gap switches in the system. The pulse rate was 40 pps at a voltage of 530 kV on the PFL which corresponds to approximately 7 kW average power.

To determine the amount of eroded material, the electrodes of the 16 kV, 20 kA rail gap switch (Fig. 5) and of the 530 kV, 11 kA high voltage spark gap (Fig. 6) were weighed before and after the run. Discharge current through the transformer primary circuit was monitored throughout the run to determine the coulombs and action ($\int I^2 dt$) passed by the rail gap switch. The PFL voltage waveform and the output voltage and current waveforms were used to analyze the operating conditions of the 700 kV spark gap. Table III and IV summarizes the results of the test run.

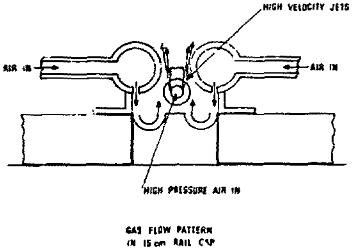

Fig. 5. Rail gap switch.

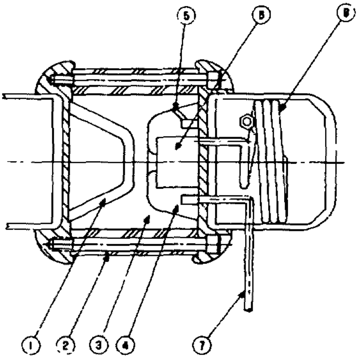

Fig. 6. High voltage spark gap.

TABLE III

Rail Gap Switch

	Erosion Data
Mass loss, main electrode #1 (brass), g	2
Mass loss, main electrode #2 (brass), g	1.9
Mass loss, trigger electrode (60/40 Elkonite), g	5.4
Charge transfer per shot, ($\int I dt$), C	36×10^{-3}
Charge transfer total, C	36×10^{3}
Action per shot, ($\int I^2 dt$), A^2-sec	592
Action, total, A^2-sec	592×10^{6}
Erosion, g/C	
Main electrode #1	55.6×10^{-6}
Main electrode #2	52.8×10^{-6}
Trigger (half of two-arc total)	75.0×10^{-6}
Erosion, g/A^2-sec	
Main electrode #1	3.38×10^{-9}
Main electrode #2	3.21×10^{-9}
Trigger (half of two-arc total)	4.56×10^{-9}

Based on the data in Table IV for the large electrode of the high voltage switch, the erosion rate is 2×10^{-8} cm^3/pulse ($\rho = 18$ g/cm^3). The damage pattern on this electrode has an area of 60 cm^2. Assuming that an erosion induced increase in the gap of 20 percent can be tolerated, the switch could survive removal of 0.4 cm from the face of this electrode corresponding to a total volume loss of 24 cm^3. At the observed erosion rate of 2×10^{-8} cm^3/pulse, the estimated switch lifetime is 1.2×10^{9} pulses.

TABLE IV

High Voltage Switch

	Erosions Data
Mass loss, large electrode (Elkonite), g	0.352
Mass loss, small electrode (Elkonite), g	0.187
Charge trnasfer per shot, C	6.5×10^{-4}
Charge transfer total, C	650
Action per shot, A^2-sec	5
Erosion, g/C	
Large electrode	5.4×10^{-4}
Small electrode	2.9×10^{-4}
Erosion, g/A^2-sec	
Large electrode	7×10^{-8}
Small electrode	4×10^{-8}

The average power dissipation in the rail gap was monitored during the million shot run by measuring the temperature rise (75°F) in the air flowing (2.23 lb/min) through the switch. Based on these measurements the average power dissipation was 704 watts or 17.6 J/pulse, a full 10 percent of the total system power. This energy is dissipated during the PFL charge cycle and during a lower amplitude ringdown period after the high voltage switch fires if residual energy is left in the system.

Data show that 6 percent of the energy stored in the 1.5 μF capacitor is lost during the dual resonance charge cycle. From measured values of equivalent series resistance in the capacitor and transformer, it is estimated that each accounts for approximately 17 percent of the energy loss leaving 66 percent assumed dissipated in the rail gap switch, the only other significant loss element in the primary circuit. With the output switch operating at 95 percent of peak, 10 percent of the originally stored energy remains in the primary circuit when the PFL is discharged. Calculations have shown that very little of this energy couples through the transformer and is dissipated in the PFL load during the ensuing ringdown. For the conditions of the million shot run, an estimated 1.7 J/pulse was dissipated in both the transformer and capacitor and 6.5 J/pulse in the rail gap switch during the PFL charge cycle and 17 J/pulse remained in the primary side after the output switch fired. Assuming that the proportionate energy loss remained constant during the late time ringdown, an additional 2.9 J were deposited in the transformer and capacitor and 11.2 J in the switch making a total of 4.6 J/pulse in the transformer and capacitor and 17.7 J/pulse in the switch. Although the absolute accuracy of the close correlation to the measured 17.6 J/pulse may be viewed with considerable reservation, it does illustrate that significant heat deposition can occur in system components when comparatively small fractions of energy are left in the system.

Liquid-Cooled Rail Gap Switch Design

During this period a modified rail gap switch was designed and fabricated. The new switch is designed for long life ($>10^7$ shots) and low maintenance. It is physically similar to the earlier prototype models[3] (Fig. 5) but the air cooled brass main electrodes have been replaced with liquid cooled tungsten-copper alloy electrodes. The trigger electrode is similar with a series of small holes on each side of the central trigger bar that directs air jets through the gap to remove shot to shot arc debris and heat. The base of the new switch is made from a machinable glass ceramic that should withstand the long term heat build up which damaged the earlier polycarbonate parts.

When tested, the switch will be monitored for power dissipation and erosion as functions of power level and number of pulses. General switching performance is expected to be nearly identical to the prototype models.

TRANSFORMER DEVELOPMENT

Exposed Primary Transformer

The exposed primary high voltage transformer[10] shown in Fig. 7 has been tested to 1 MV and operated at 44 pps for as long as 30 minutes on the REPIT test facility[9] To reach 2 MV, which is the design goal for this transformer, a new output switch and load capacitor have been designed and are currently being installed.

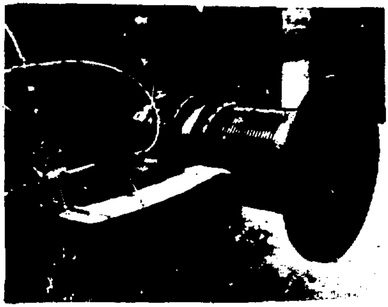

Fig. 7. Exposed-primary, high voltage transformer.

This transformer, a lower cost design than the transformers being tested on RTF-I has an exposed single turn primary to enhance heat removal for repetitive pulse service. The flange connections to the primary also facilitate access to the secondary winding if it should ever need to be repaired.

The transformer has the following measured parameters:

Primary inductance: 340 nH
Secondary inductance: 390 μH
Coupling coefficient: 0.8

Although primarily intended as an experimental unit to demonstrate long term endurance with voltage stresses in the transformer winding in the range of 400 kV/cm, the transformer is also being used as a high voltage source for general testing on the REPIT facility and is adaptable to RTF-I.

3 MV Transformer

A new transformer (Fig. 8) has been fabricated and assembled. It will be tested to 3 MV to demonstrate reliable operation up to that voltage level and to observe secondary winding endurance under the

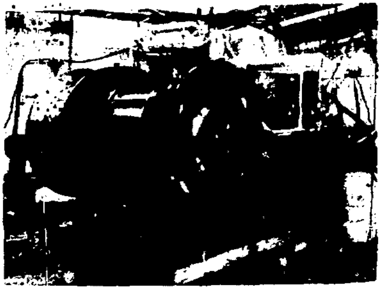

Fig. 8. Three megavolt transformer.

combined conditions of high total voltage and a maximum winding stress of 400 kV/cm. Experiments testing the dielectric strength of laminates indicate that the breakdown threshold of this transformer winding should be at least 580 kV/cm.

The experiment (Fig. 9) involves discharging a ±50 kV, 0.93 μF capacitor bank through the single primary turn of the transformer and measuring the secondary voltage step up on a 1.1 nF water capacitor. The water capacitor is subsequently discharged through a self-break spark gap into a copper sulfate load resistor.

Fig. 9. Three megavolt transformer experimental set-up.

Initially the transformer is being tested in a single swing charging mode. Under these conditions the calculated maximum voltage rise with a ±50 kV charge on the capacitor bank will be 2.2 MV which represents 52 percent energy tansfer. Thus far the system has been operated to 1.6 MV with a bank charge of ±50 kV. At this level a minor breakdown occurred between the torus on one end of the core and one of the case grading rings. This track along the edge of the mylar stack caused very little damage. The breakdown path has been cleaned and the transformer reimpregnated.

The cause of the breakdown is not clear since the calculated voltage stress in the oil at the point of breakdown was only 150 kV/cm, well below the measured 550 kV/cm bulk breakdown of x-ray oil or 580 kV/cm breakdown of mylar x-ray oil laminates. The only unusual feature around the breakdown area was a puddle of epoxy between the torus and first insulation wrap. The possibility exists that air bubbles in the epoxy puddle caused an initial breakdown which eventually propagated through the oil.

Subsequent tests will include single swing charge operation to over 2 MV. Following these tests, the transformer will be converted to a dual resonance charge cycle and tested to 3 MV.

Repetitively Pulsed Marx Generator Design Studies

Design was completed for the high-voltage, high-power Marx generator test facility, RTF-II (1 MV, 10 kJ per pulse, 10 to 100 pulses-per-second). The facility will be used to study electron beam accelerator components at time averaged power levels approximately one order of magnitude larger than those of RTF-I.[2,3] The Marx generator is designed with inductive isolation between stages to minimize power loss in the generator itself which could be substantial at time averaged power flows approaching one megawatt.

Previous analysis using the SCEPTRE[11] network analysis program demonstrated that the energy loss in the charging inductors can be reduced to a few percent. Subsequent analysis indicates that loss due to stray capacitances can be held within this same limit. It, therefore, appears reasonable to expect 90-95 percent overall energy transfer efficiency through the Marx generator.

RTF-II is shown schematically in Fig. 10. With each of the sixteen 0.35 μF capacitors charged to 62.5 kV, the output voltage is 1 MV and total stored energy is 11 kJ. A "Z" type[12] Marx generator configuration with the first two gaps triggered is shown to optimize erection while minimizing losses. Provision will be made to UV preionize the remaining gaps if it is necessary to achieve stable operation.

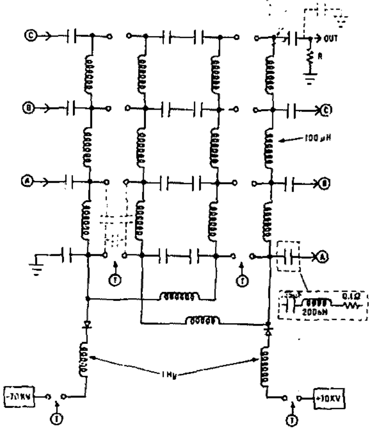

Fig. 10. Schematic diagram of RTF-II, a 1 MV, 10 kJ repetitively operated Marx generator

Development of the spark gaps is seen as the primary challenge in constructing this system. These 125 kV gaps are required to operate at peak currents of 50 kA and with a dwell period between shots of 0.01 to 0.1 seconds. The operating voltage level of these gaps is intermediate between the rail and output gaps of RTF-I. The peak operating current is about twice the equivalent current in the existing gaps and the pulse duration is about 20 percent of the rail gap duration. To explore this switching regime the spark gap test facility (SGTF), shown in Fig. 11 is being constructed. SGTF will be a bipolar device with a dual modulator section charging two 0.15 μF capacitors in 2 ms. Semiconductor diodes are used to hold the voltage. The gap under test is triggered switch S_2. A third switch, S_3, can be added to test the untriggered Marx switches. Using existing components, with the exception of the switches, SGTF will be able to reproduce the voltage, current, pulse duration, and repetition rate required of the Marx spark gaps, although it will not reproduce the exact wave shape.

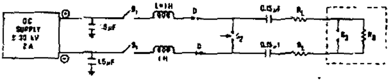

Fig. 11. Spark gap test facility (SGTF) schematic diagram.

A thyratron controlled trigger system has been developed for SFT. and tested to pulse rates in excess of 100 pps. The thyratron pulser delivers 20 kV pulses which are used to trigger a four stage, 0.25 nF, "doorknob" capacitor Marx generator. This Marx will be used to trigger the spark gap under test in SGTF. It will also be used to trigger RTF-II.

The spark gap shown in Fig. 12 has been built as a first candidate for the Marx spark gap. Its design parameters are scaled down from the 700 kV output spark gap of RTF-I. A trigger electrode has been added in the configuration shown. The gap employs rotating airflow with exhaust through the main electrodes, a configuration which has proved efficient in purging previous switches.

The specifications for the primary energy supply for the RTF-II and other general laboratory use have been written and a request for purchase initiated. A dc power supply capable of opeating in the eight modes of Table V was chosen.

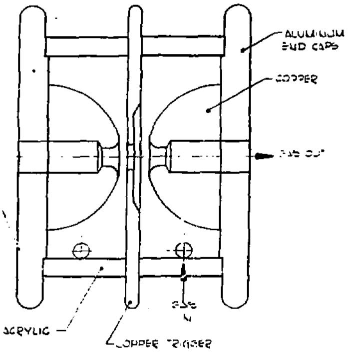

Fig. 12. Marx spark gap prototype.

TABLE V

Power Supply Operating Levels

Maximum Voltage	Maximum Unipolar Current	Maximum Bipolar Current
80 kV	25 A	12.5 A
40 kV	50 A	25 A
20 kV	100 A	50 A

The supply will derive its power from existing 4160 V, 3 ϕ power mains which with the appropriate switching and safety gear that are now available in the rep rate laboratory.

Capacitors for the Marx generator have been ordered as have the Marx tank and tankage for approximately 20,000 gallons of transformer oil. Assembly hardware is being designed. The Marx tank was designed to accommodate up to 24 stages so the maximum output voltage may be raised to 1.5 MV if desired.

Alternatively the extra space may be filled with a Type A Guillemin pulse forming network[13] for generating 1.5 μs, 500 kV pulses suitable for driving a 37 Ω large area, electron beam diode for laser excitation applications. Such a network that would use existing components has been designed with the SCEPTRE program. The calculated output voltage pulse into a matched resistive load from a two element PFN is shown in Fig. 13. An associated diode is being designed.

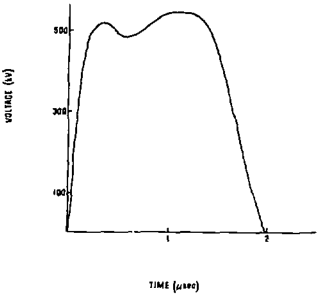

Fig. 13. RTF-II PFN output voltage.

REACTOR SYSTEM STUDIES

Overview

Substantial progress was made during this period on initial efforts in reactor design studies. A general conceptual design criteria for particle beam driven reactors has been established with the combustion chamber operating at pressures in the range of 0.1-1 atm and the beams propagated to the target through plasma channels. Investigation of the major physics issues for this type of reactor scenario has been initiated. Efficient particle beam drivers will allow economically feasible operation of relatively small reactor systems (100 Me). Economic and reactor design issues for these small pure fusion reactors is underway. Bechtel Corporation has nearly completed a 1000 MWe electron beam-driven, hybrid-reactor, design study.

GENERAL CONCEPTUAL DESIGN

Current design concepts for particle-beam driven reactors (PBDR--electrons and light ions) employ a gas in the combustion chamber for beam propagation along ionized channels from the particle source to the pellet. The range of gas pressures which satisfy requirements for beam propagation is quite large: 50-760 torr. The ability to have a gas in the combustion chamber at these pressures is the principal factor leading to a great deal of flexibility in conceptual reactor size, power, and configuration.

The principal criteria which govern the design of particle-beam-driven reactors have been determined and analysis of them is underway. These include the beam injection geometry, power flow efficiencies, x-ray and debris attenuation, the magnitude of the blast overpressure, and the energy transport through the gas.

Beam Injection Geometry

A possible geometrical arrangement for injection of an electron beam into the combustion chamber is shown in Fig. 14. The major parts are the diode, the injection channel, and a fast-shutter for diode protection. The sequencing is as follows: (1) The fast-shutter opens. In Fig. 14, the shutter consists of two rotating wheels. The aperture in the synchronous "rep-rate" valve is open for about 3 ms. The two apertures are collinear with the beam line 10 times per second for 10 Hz operation. (2) The plasma anode is formed. Plasma is created between the anode plates either by flashover of an insulator in a gas or by plasma guns. This plasma establishes the anode equipotential in the beamline so that significant material damage is prevented when the electron beam is extracted and focussed. (3) The channel lasers are fired. With relatively small amounts of energy and power (~1 J/cm^3, 1 μs pulse), two sets of lasers provide sufficient pre-ionization (~1 percent) to guide the channel discharges that are for particle beam propagation. The beamline laser set consists of one laser per injector. The return current laser set consists of two lasers, one located at the top of the combustion chamber and one below. The lasers could be CO_2 systems providing direct photo-ionization or shorter (UV) wavelength systems providing two-step excitation and ionization. (4) Voltage is applied to the upper and lower channel electrodes establishing arcs along the preionized paths from these electrodes to the injector anodes. While the arc currents increase to the required level (~50 kA) in 2-5 μs, the shock waves created by the arcs expand to ~1 cm in diameter, leaving a low-density plasma channel. (5) The main pulse is applied to each diode. The intense electric field in each diode causes an electron beam to form. As it traverses the diode gap, self-magnetic fields cause the beam to pinch down to a diameter of ~1 cm.[14] The electron beam propagates along, and is confined by, the current-carrying plasma channels.[5] The beam entry ports in the chamber wall should be several times a beam diameter, perhaps 5-10 cm in size.

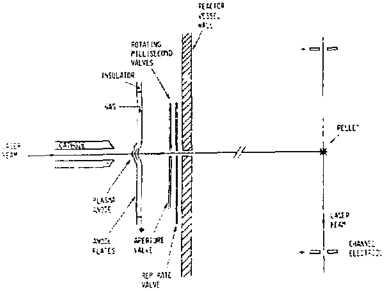

Fig. 14. Electron beam injection geometry.

A similar geometrical arrangement for the injection of ions is shown in Fig. 15. The valving and laser-preionization configuration is similar to that in Fig. 14. In the diode, ions are extracted from an anode plasma created by surface flashover and accelerated to a virtual cathode (electrons tied to magnetic field lines define the cathode equipotential).[15] Since the anode surface is a spherical section, the space-charge-neutralized ions ballistically focus at a point which is one end of the channel. The ions are then magnetically confined in the channel as they propagate to the pellet.

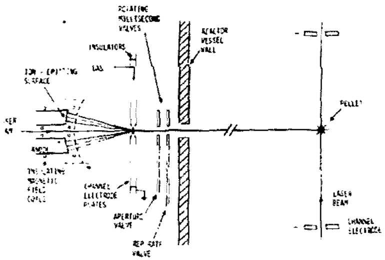

Fig. 15. Ion beam injection geometry.

The injection geometry, therefore, influences the reactor design in several ways: (1) A chamber "prefill" in the range of 50 torr-atmospheric pressure is required for beam propagation along ionized channels. At pressures below 50 torr, the channel expansion time might be less than that required to build up the necessary channel currents with reasonable-inductance capacitor banks. (2) The use of hollow diodes allows for direct-path laser preionization, minimizing the number of ports in the chamber wall. (3) Introduction of the particle beams into the combustion chamber after spatial focusing permits small entry ports into the chamber to be used.

Power Flow Efficiencies

The efficiencies involved in the power conditioning and transmission steps of a particle beam driver are shown in Fig. 16. The value of energy present (top) or lost (bottom) at any point in the driver is normalized to 1 MJ absorbed by the target. The magnitudes of the efficiencies have been extrapolated from present experiments and represent expected values. The overall efficiency from wall plug to absorption by the target will likely be in the 30-40 percent range.

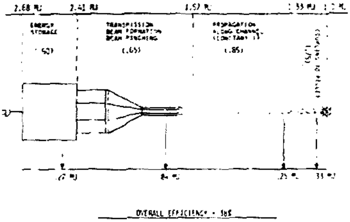

Fig. 16. Power flow efficiencies.

The effect of power flow efficiencies on reactor design is seen in the energy lost to the chamber gas (energy lost in propagation along the plasma channels and coupling to the pellet) and the amount of energy which must be recirculated to the drivers between microexplosions.

X-ray and Debris Attenuation

Particle beam pellets are expected to be more massive than laser targets because of the greater range of high-energy electrons and light ions in materials compared to photons. As a result, the mean x-ray debris ion energies tend to be lower. Characteristic values for an electron beam pellet may be 350 eV for the x-ray black body temperature and 50 eV/a.m.u. for the debris ions. The debris ions would then have energies less than 1 MeV and would be easily stopped in the >100 torr-meters gas thickness in the combustion chamber.

Table VI shows the mean free path for 350 eV (monoenergetic) x-rays in several gases for 1 atm and 100 torr pressure.[16] For adequate x-ray attenuation, at least 3 mean free paths should be obtained in the chamber radius. The values given in Table VI indicate that nearly any gas other than hydrogen will adequately attenuate the imploson x-rays at pressures around 100 torr in a chamber with radius >1 m.

TABLE VI

Mean Free Path in Laser for 350 eV X-rays

GAS	MFP AT 1 ATM. (cm)	MFP AT 100 TORR (cm)
H_2	55.3	420.1
He	3.7	28.3
Li	0.65	4.9
N_2	0.4	3.0
Ne	0.14	1.05
Ar	0.03	0.21

The effect the chamber gas prefill has on reactor design is, therefore, very significant. The walls will not be subject to the fast transient x-ray and ion heating, and the resultant melting, ablation, sputtering or spalling will not occur. The dense buffer gas acts as an excellent wall protector, but it does give rise to other problems which must be considered, such as the blast overpressure.

Blast Overpressure

The very sudden absorption of the x-ray and debris ion energy by the combustion chamber gas results in a hydrodynamic shock. The dynamics of the shock have been studied using CHARD D[17] and were described in detail in a previous report.[18] Results of a calculation for a 60 MJ pellet, from which 18 MJ of x-ray and ion energy was deposited in 100 torr air, are shown in Fig. 17. Because the ion energy is the greater part of the deposited energy, and the deposition of this energy is very local, the overpressure begins as a strong shock and decays approximatley as R^{-3}. As it propagaters outward the overpressure moves through a transition to a weak shock and decays approximately as R^{-1}. At R = 4 meters, the overpressure has decayed to ~1 atmosphere. The dependence of overpressure on gas prefill pressure is weak at this radius, increasing only 60 percent for a tenfold increase in gas pressure.

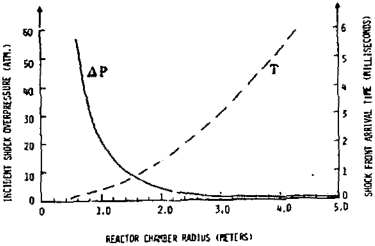

Fig. 17. Shock wave overpressure and arrival time vs. radius for a 60 MJ pellet in 100 torr of nitrogen.

The impact of the overpressure on reactor design is to require that the chamber wall be capable of surviving the "reflected" overpressure, usually about 2.5 times as large as the incident overpressure for very weak shocks. This force can be taken as a hoop stress. The relation between the stress in a wall of thickness t and the reflected overprerssure P is

$$\sigma_w = \frac{P + P_o - P_B}{2t} R,$$

where P_o is the initial chamber pressure and P_B is the pressure behind the wall. As an example from Fig. 17, if P = 2.5 atm at R = 4 m, the stress in a 1 cm thick wall is 33 MPa (4.9 ksi).

Figure 17 also shows the time of arrival of the shock front as a function of radial distance. The calculation indicates that 5 ms will elapse after the microexplosion before the shock reaches a wall with a 4 m radius. This amount of time is sufficient to allow a valve to close, thereby protecting the entire driver system from everything but the pellet neutrons. Since the entry ports are only a few centimeters in diameter and since hollow diode geometries appear feasible, damage to the driver systems is expected to be minimal.

Energy Transport Through the Combustion Chamber Gas

After the pellet x-ray and debris ion energy has been absorbed by the combustion chamber gas, conduction, convection, and re-radiation of the energy to the reactor walls begins. The rate is sensitive to the gas pressure and distance to the walls, and probably to the gas type. At the present time, the transport phenomena have been studied using CHART D without hydrodynamic effects included (i.e., no convection). These calculations are described in detail in another section of this report. Results of a calculation for a 75 MJ pellet in 100 torr air with the vessel wall radius at 4 m and a repetition rate of 10 Hz are shown in Fig. 18. The curve shows the rate at which energy is transported to the wall between the 23rd and 24th shot. In this particular case, equilibrium conditions were obtained prior to the 23rd pellet shot. At t = 0, before the first shot, the background gas temperature was assumed to be 750°K (the wall temperature). At equilibrium, the gas temperature is ~7700°K. This value may be acceptable since the wall temperature remains at 750°K. For lower pressures and smaller vessel radii, the energy transport is more rapid and the equilibrium gas temperature lower. The dependence of the energy transport on gas type is difficult to determine due to the lack of available opacity data in this low temperature range.

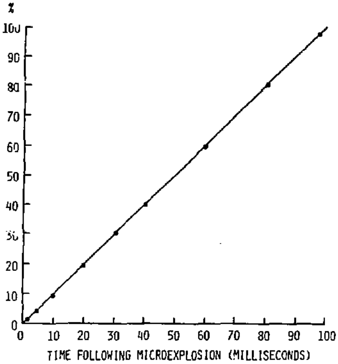

Fig. 18. Percentage of non-neutronic energy form 75 MJ pellet transported from 100 torr air to chamber wall at R = 4.0 m as a function of time following microexplosion.

The effect of the absorption and transport of x-ray and debris ion energy by the gas in the combustion chamber is to "smooth out" over many milliseconds the pellet energy which would otherwise appear at the wall as a fast transient accompanied by large thermal stresses.

Reactor Chamber Sizing

For gas-filled, particle-beam-driven reactors the design criteria which might result in an upper size limit on the chamber radius are (1) the energy transport time through the gas which is achievable without recirculating the gas between microexplosions and (2) the potential difficulty of producing long (>5 m) ionized channels and achieving satisfactory beam propagation through them.

The design criterion which results in a lower size limit is the wall hoop stress produced by the reflected overpressure from the hydrodynamic shock. Figure 19 shows the minimum chamber radius as a function of pellet yield for constant 10 ksi loading in a 1.0 cm thick liner at a chamber prefill of 100 torr. Also shown are the values of neutron wall loading for 10 Hz operation with the indicated radii. For cylindrical vessels with unity height-to-diameter ratios, the values shown would be the peak values, and average loadings would be two-thirds of the peak values.

Figure 19 shows that the minimum vessel size determined by the overpressure stress in the 1-cm-thick wall is consistent with "economic" values of neutron wall loading at moderate repetition rates, and that this complementary pair of constraints scales to small vessel sizes. Even the numbers shown in Fig. 19 are not minimum values, however. If the vessel walls were made thicker and

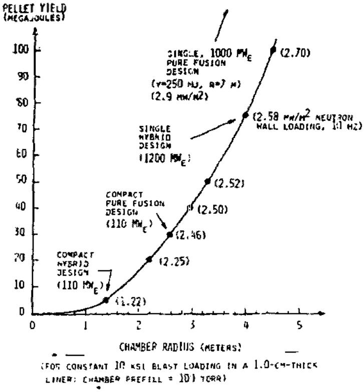

Fig. 19. E-beam reactor chamber sizing based on reflected overpressure from hydrodynamic shock.

incorporated front-surface or internal cooling to limit thermal stresses, the vessel sizes could be reduced--or alternatively, the yield increased--so that higher values of neutron wall loading, perhaps above 5 MW/m^2, would be obtainable with more frequent wall replacement.

ECONOMIC CONSIDERATIONS

Minimum "Economic" Pellet Gain and Yield

For inertial confinement fusion reactors, the product of driver efficiency and pellet gain, $\eta_D Q$, is an important economic figure of merit. In power systems where the majority of recirculating power is associated with the driver, this product is related to the plant thermal efficiency η_{th} and recirculating power fraction f by the equation (1)

$$\eta_D Q \simeq \frac{1}{\eta_{th} f} \qquad (1)$$

Since all recirculating power must pass through the balance of plant, which accounts for the greatest fraction of plant costs, the cost of the power plant is very sensitive to the recirculating power fraction when $f \gtrsim 0.25$ (cost $\sim f/1-f$). For a thermal conversion efficiency of 0.4, the value of $\eta_D Q$ necessary to keep the recirculating power below 25 percent is 10.

Table VII shows the pellet gain required for use with several values of driver efficiency. Also shown are the minimum pellet yields allowed by this economic criterion for pellet input energies of 0.25 MJ and 1.0 MJ. If an input energy of 1.0 MJ is required to get significant pellet gain, a one percent efficient driver will require pellets having a gain of 1000 and a yield of 1000 MJ while a 40 percent efficient driver could be used with pellets having a gain of 25 and a yield of only 25 MJ. Furthermore, since these drivers are fast pulsed systems, they require either capacitive or inductive storage systems the size of which is inversely proportional to driver efficiency.

TABLE VII

Required Pellet Gain vs. Driver Efficiency for Pure Fusion System

ECONOMIC IMPLICATIONS: PURE FUSION SYSTEMS

$(\eta_D Q)_{MIN} = 10$

	DRIVER EFFICIENCY (η_D)		
	.01	.04	.4
GAIN Q	1000	250	25
YIELD (.25 MJ IN)	250	62.5	6.25
YIELD (1 MJ IN)	1000	250	25

The essence of the economic requirement on the $\eta_D Q$ value is that lower efficiency drivers require larger storage systems, higher gain and higher yield pellets and, therefore, larger or more complex reactor vessels.

Effect of Driver Replacement Costs

Table I on page 111 shows the characteristics which are generally believed to be required for experimental, demonstration, and commercial power reactors. In this table, f is the recirculating power fraction. The lifetimes of reactor components (especially driver components) could be considerably less than the values given in Table I for the "system" lifetime provided that (1) system reliability is sufficiently high to allow the plant availability factor required for economic operation to be achieved with moderate down-time for component replacement, and (2) component replacement costs do not substantially increase the cost of power generation. Replacement cost includes the cost of the component and of the manpower for replacing such items. If D represents this cost in mills/joule, E_s is the pulse power energy storage in joules and L is the component lifetime, then the driver replacement cost (B) that must be recovered each hour of reactor operation is given by equation (2)

$$B = 3.6 \times 10^3 \; R \frac{DE_s}{L} \qquad (2)$$

The output power (P) in kW is given by equation (3) and (4)

$$P = \frac{E_s}{1000} \eta_D \eta_T Q \,(1 - f)\, R \qquad (3)$$

$$P = \frac{E_s}{1000} \, \frac{(1 - f)}{f} \, R \qquad (4)$$

Thus the replacement cost that must be regained for each kWh sold is

$$B/P = \frac{3.6 \times 10^6 \; D}{L} \, \frac{f}{1 - f} \qquad (5)$$

An estimate of the costs of the components most likely to be expended is 700 mil/J for capacitors, 100 mil/J for low voltage switches and 500 mil/J for high voltage switches or 1300 mil/J for the total cost. Thus if the worst case is such that all of these components must be replaced each year (2×10^8 shots) on a reactor with a recirculating power fraction of 0.25, then the contribution to the power cost would be 8 mil/kWh. If the recirculating power fraction of 0.1 or the life is three years, the contribution to power cost drops to 2.6 mil/kWh, a negligible amount. Thus under the above assumptions these components must last 1-3 years to have negligible impact on the cost of power.

Parametric Analysis of Power Reactor System Costs

The system model which is used for determining economic parameters of conceptual reactor designs (EBM) has been described in a previous report.[19] In this period, the model was modified in order to make it more accurate for the parameter determination of small reactor systems. The original code was optimized for use with reactors in the 500 MWe to 1200 MWe range; for systems outside that range significant errors were encountered. New algorithms permit reasonably accurate economic analysis for reactors ranging in size from 100 MWe to 2000 MWe. The changes which have been made for the various components comprising direct and indirect costs are summarized in Table VIII. All other algorithms in the code remain unchanged. The costs are in 10^6 1976 \$ and reactor sizes are in MWe. The new algorithms are presented graphically in Fig. 20.

TABLE VIII

EBM Cost Algorithms

	[illegible]	[illegible]		
[illegible]		[illegible]	[illegible]	[illegible]
[illegible]	[illegible]	[illegible]	[illegible]	[illegible]
[illegible]	[illegible]	[illegible]	[illegible]	[illegible]
[illegible]	[illegible]	[illegible]	[illegible]	[illegible]
[illegible]	[illegible]	[illegible]	[illegible]	[illegible]
[illegible]	[illegible]	[illegible]	[illegible]	[illegible]
[illegible]	[illegible]	[illegible]	[illegible]	[illegible]
[illegible]				
[illegible]	[illegible]	[illegible]	[illegible]	[illegible]
[illegible]	[illegible]	[illegible]	[illegible]	[illegible]
[illegible]	[illegible]	[illegible]	[illegible]	[illegible]

[illegible]

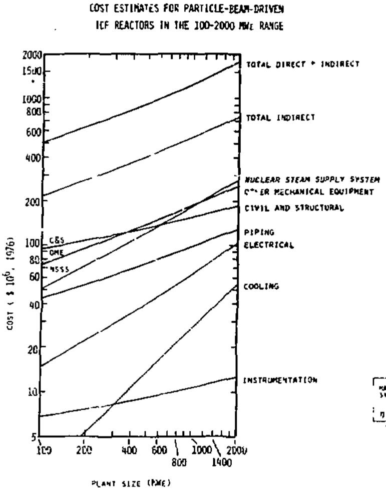

Fig. 20. Graphical presentation of EBM cost algorithm.

SPECIFIC REACTOR (POINT) DESIGNS

Hybrid Reactor Design Studies

The Bechtel Corporation engineering design of a conceptual 1000 MWe electron-beam-driven fusion-fission power reactor is approximately 80 percent complete. Information concerning driver size and configuration, beam propagation, and energy transport through the 100 torr nitrogen chamber gas has been provided by Sandia. The power reactor generates 720 MW of fusion power with a 10 Hz repetition rate and a pellet energy gain of 18. By employing a depleted uranium blanket having a neutron energy gain ~6, a total plant thermal power of 3440 MW and net electric power of 1090 MW are obtained. In one year, this plant design would produce nearly 3000 kg of fissile fuel, an amount sufficient to power six light water reactors of equivalent electrical output. A cost analysis of the plant design is currently underway.

Compact Pure-Fusion Reactors

An example of the energy flow in a single shot of a compact particle beam reactor is shown in Fig. 21. For this example, a hypothertical pellet with an input energy of 1 MJ and a gain of 30 has been chosen. (One type of pellet which might provide such performance is the "magnetically insulated pellet".)[20] The reactor vessel radius is 2.6 m, and 10 Hz operation leads to a net plant power level of 110 MWe. The recirculating power fraction is 24.9 percent, and the net plant efficiency is 30.0 percent.

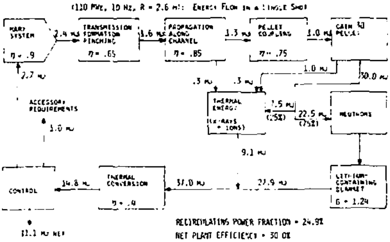

Fig. 21. Energy flow for a single shot of a compact particle-beam-driven, pure-fusion reactor.

A drawing of the geometry of such a reactor, with the approximate size of associated components, is given in Fig. 22. The figure shows the energy storage, pulse forming, and transmission sections of the drivers, the gas filled reactor vessel and its blanket, and the beamline and return current plasma channels.

The compact reactor unit described here could serve either as a stand-alone 100 MWe unit or a module of a larger power system incorporating several units. It should also be emphasized that a unit

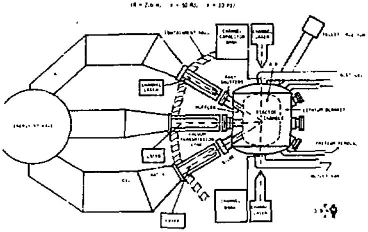

Fig. 22. Compact 100 MWe particle-beam-driven power reactor.

of this kind could serve as a small prototypical power reactor to demonstrate the technical feasibility of the approach at a comparatively low cost.

Summary

Gas-filled, particle-beam-driven reactors are sized on the basis of the reflected overpressure from the hydrodynamic shock and on the neutron wall loading. These constraints are complementary and scale similarly over a wide range of reactor sizes.

The high efficiency of particle-beam drivers allows low values of recirculating power to be achieved at relatively small pellet gains. The combination of the two, i.e., a highly-efficient driver and the ability to employ a chamber prefill in the 50 torr to 1 atm range may permit the following:

1. Small pellet gains (near to intermediate term physics) to be used economically.

2. Small pellet yields to be used economically.

3. The construction of a small (chamber radius <2 m), relatively inexpensive (perhaps at a cost in the $170-$200 M range) experimental power reactor (recirculating power fraction = 1) of the 50 MW (thermal) class using a pellet gain of only ~4. This could be based on pellet experiments projected for EBFA II in 1985-86.

4. The construction of a small (chamber radius <3 m), relatively inexpensive demonstration power reactor (recirculating power fraction = 0.25) of the 100 MWe class using a pellet gain of only ~30.

5. The construction of commercial power plants using multiple reactor vessels in a system which could allow derated turbine operation during replacement of complete reactor modules. With the potential of maintaining large fractional plant output during module replacement, the possibility of operating at higher stresses and neutron fluences may be enhanced.

LOW-CURRENT DENSITY DIODE PHYSICS STUDIES

Overview

Several candidate laser systems for fusion reactor application require large area, low current density (1-40 A/cm^2), microsecond pulse duration electron beams to provide excitation of either the gas laser medium or a photolytic driver. Space charge limited flow for these low-current density beams are achieved with 10-50 kV/cm mean electric fields in the anode cathode gaps. With these low values of electric fields, it is difficult to achieve the desired spatially and temporally uniform current densities at the anode. In addition, to achieve efficient operation of these diodes, it will be necessary to suppress emission from cathode support structures. During this period, investigations of cathode plasma instabilities occcurring with highly field enhanced emitters continued. Techniques for enhancing or suppressing electron emission were extended to additional materials and different voltage waveshapes.

One technique to circumvent the inherent difficulties involved in forming the cathode plasmas in low current density diodes is to inject plasma into the anode-cathode region. The plasma can either be produced within the diode or injected from plasma guns.[23] Depending upon the plasma density, these diodes could operate in several different modes and extensive research will be required to model each of these modes. If the plasma density is high ($\sim 10^{17}$ ions/cm^3) and the plasma located only in the cathode region, the didoe should function in much the same manner as a cold-cathode diode but without the field-emission and the metallic whisker explosion phase. With lower densities ($\sim 10^{11}/cm^3$), a sheath is formed near the cathode as ions are removed and space charge limited electron and ion flow cross this sheath.[22] For a constant impedance, a stable situation, where ions are replaced by plasma flow or impact ionization within the plasma at the same rate that they are removed from the sheath area, must be established. A third mode could be at still lower densities ($<10^9$ ions/cm^3) where the plasma is quickly removed from the anode cathode gap but the ions heat the cathode and enhance electron emission.

During this period, several techniques for generating large area plasma sources by surface flashover that are compatible with operation in a high voltage diode were investigated. Initial diode experiments to investigate impedance behavior with plasma injected from either of these sources or plasma guns have been initiated.

Needle Cathode Instabilities

Data taken in the preceding six months confirm our previous results on the relation between the onset time of instability in needle cathode diodes and the current density being drawn. Figure 23 displays the type of instability observed, a "spike" in current density to more than five times the ambient, presumably space charge limited value. The upper trace in Fig. 23a is the diode voltage which peaks at 160 kV. The lower trace is the axial current density which becomes unstable at 270 ns into the pulse and goes off the bottom of the picture. The total current in Fig. 23b increases at this time to 80 percent of the short circuit value. The instability is over in less than 40 ns.

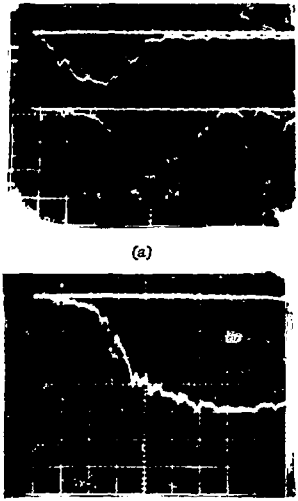

Fig. 23. Typical voltage and current waveforms displaying current density "spike" (time base 100 ns/cm).

a) Diode voltage, 87 kV/cm (upper trace). Current density on axis, 60 A/cm^2/cm (lower trace).
b) Total diode current, 3 kA/cm.

Using LPN accelerator, a Nereus Marx generator with a two element Guillemin Type A pulse forming network (PFN) to generate a 1.1 μs, 200 kV pulse with 200 ns risetime (see Fig. 27), data were taken at various anode-cathode gaps to observe the relation between instability onset time and current density. Additional data were taken without the PFN and with a 44 μH inductor between the Marx generator and diode to slow the voltage risetime and investigate risetime effects in instability onset. In each case current density on the axis of the needle, total diode current, and voltage were recorded. The diode is shown in Fig. 24 together with a masked Faraday cup on axis for current density measurement, a CVR to measure

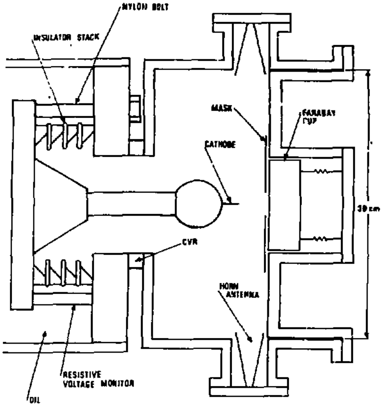

Fig. 24. LPN diode.

total diode current and a resistive voltage monitor. Figure 25 shows the relation between instability onset time and current density on axis. The solid curve is a semi-empirical fit to data in the range 10^2 A/cm^2 j $\le 10^4$ A/cm^2. There is qualitative agreement. Note the "knee" in the j vs. t plot near t = 200 ns which is the risetime on the voltager pulse. The plotted points fall rapidly with increasing j until t $\simeq$ 200 ns. Thereafter instability occurs at approximately constant time independent of j. The data show a strong tendency for instability to occur at the end of the rising portion of the waveform. When the risetime was increased, the instability occurred later in time, near the end of the voltage rise. However, the current density was reduced also and the resultant data point, the uppermost on Fig. 25, is on the same curve as the earlier data.

Impedance waveforms have been fit to a diode model based on the concentric sphere Child-Langmuir space charge limited flow calculation. Two variable parameters, the speed of closure of the A-K gap by the cathode plasma and a

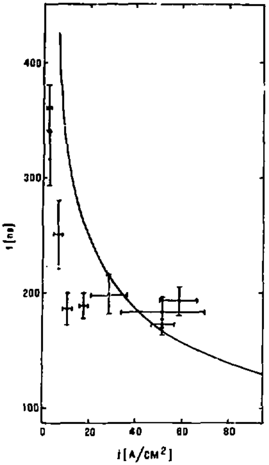

Fig. 25. Current density vs. instability on-set time for blade and needle cathode data.

normalization were selected by a least squares minimization. The mean closure speed versus A-K gap is shown in Fig. 26 where the solid points are the fit values. The circles are the closure speed calculated from the diode short time averaged over many shots. A tendency to increasing speed with larger gaps is obvious. At the largest gap (6 cm) the diode shorts somewhat later than the fit would predict. Based on the success with this model at smaller gaps and its ability to reproduce the 6 cm data at earlier times, the data may be suggesting a slowing of plasma expansion late in time.

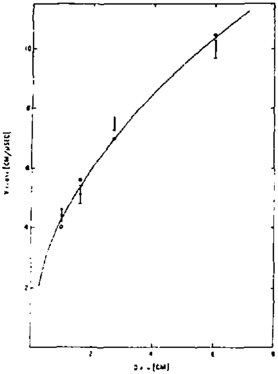

Fig. 26. Anode-cathode (A-K) mean closure speeds vs. A-K gap spacing.

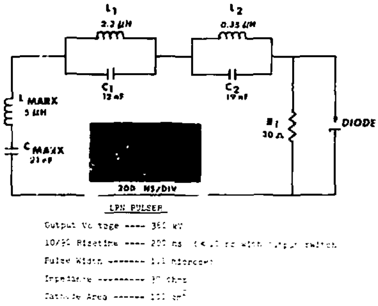

Fig. 27. LPN circuit diagram and voltage waveform.

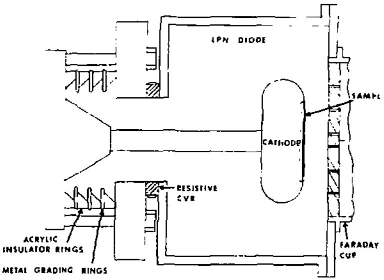

Fig. 28. Diode configuration.

Emission Enhancement

A polyurethane material which is filled with carbon particles has been investigated as part of the continuing study of electron emission enhancement from cathodes subjected to low electric fields (20-55 kV/cm). The material (ECCO-SORB, Emerson and Cuming, Inc., Gardinia, CA) consists of a polyurethane-latex base containing a 30 percent concentration of fine carbon particles. The emission quality and uniformity were investigated while being pulsed with the above fields having a pulse duration of one microsecond. The emission pattern was observed using open shutter photographs, radiochromic film, and a segmented Faraday cup. This investigation was performed on the LPN accelerator, whose equivalent circuit, parameters, and voltage waveform are shown in Fig. 27, with the diode test configuration shown in Fig. 28.

Open shutter photographs were taken of the emission sites on a 10.2 cm diameter cathode while recording the total diode current flowing through a current viewing resistor (CVR). The photographs are pictures of the cathode reflection in a polished metal anode. At 22 kV/cm, the current flow was indistinguishable when the diagnostics were adjusted to measure 0.1 amp cm^{2}; however, the photographs indicated cathode plasma had formed at several points in a cluster. When the electric field was increased to 25 kV/cm, 0.27 amp/cm^{2} of current was recorded and the open shutter photographs indicated more plasma points at the site of the original cluster with other clusters beginning to light up. The current rise lagged behind the voltage rise by 0.65 μs. Increasing the electric field in discreet steps to 52 kV/cm caused the current turn on time to decrease at each step with a corresponding increase in plasma clusters as shown in Fig. 29. In contrast to the earlier reported work with graphite felt, the emission sites of this material were randomly situated across the cathode surface with only a few of the plasma clusters reappearing at the same location on a shot-to-shot basis or electric field variation.

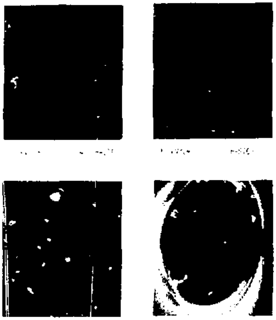

Fig. 29. Apparent emission sites on a carbon-polyurethane cathode at low electric fields.

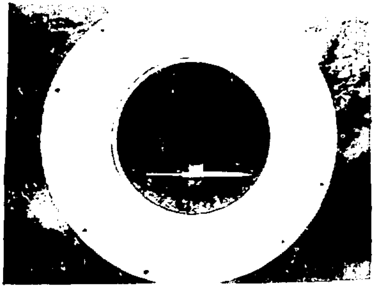

Fig. 30. Four segment Faraday cup.

A segmented ring Faraday cup was used as the anode to determine if the beam current was uniform across the anode surface. The sum of the peak beam currents impacting upon the four segments shown in Fig. 30 were in good agreement with the total peak current measured by the CVR. Calculations of the beam density from the peak current on each Faraday cup indicated the beam density to be uniform within ±10 percent for some shots but ±25 percent on others. However, these measurements indicated that the beam currents arrived at the individual segments at different times. The variation in time of maximum current or current rise varied up to 0.5 μs and did not seem to be dependent upon the applied electric field. Cathode plasma instabilities (described in the preceding section of this report) were also evident from these Faraday cup measurements.

Radiochromic dosimetry maps implied the beam arrived at the anode in annular shaped beamlets that impacted on the anode in an incidental fashion. It appears the current density at any given point is a function of the number and intensity of the individual beamlets which may be superimposed on each other. A typical radiochromic map is shown in Fig. 31. The beamlets are probably

Fig. 31. Radiochromic film map of anode current density.

launched from the individual plasma clusters and the spatial and temporal uniformity of the total beam density could be improved by a more uniform distribution of these clusters. Surface irregularities of the test sample may have contibuted to this nonuniformity. Samples which possess a better surface finish and higher carbon concentration will be tested in the near future.

Emission Suppression

The results of electron emission suppression experiments using somewhat nonuniform field cathodes have appeared in previous semi-annual progress reports. The results of experiments using uniform field cathodes to evaluate the effects of dielectric coatings in suppressing electron emissions in low-current density electron beam diodes with a one microsecond pulse duration are reported here. The goal of suppression experiments is to find a dielectric coating that can be easily and economically applied to large cathode support structures to suppress spurious electron emissions that occur during long pulse durations.

The uniform field cathodes were contoured of aluminum to approximate a 15 cm diameter Bruce profile[23] as shown in Fig. 32. Diamond polish with particle sizes decreasing progressively from 15 microns to 1/4 micron was used to hand polish the surface to a bright shine. A bare aluminum cathode was used as a test control sample for comparison of the effectiveness of the various dielectric coatings. Ten different types of dielectrics were applied to the above substrates and subjected to pulsed electric fields of 70-175 kV/cm using the LPN accelerator, Fig. 27. All of the following data was taken with a 1 cm anode-cathode spacing using the test set-up shown in Fig. 33. Examination of the cathodes, after being tested, indicated the test set-up did exhibit uniform field qualities. Emission sites appearing on the cathode surfaces were randomly spread across the entire surface area.

AS MACHINED

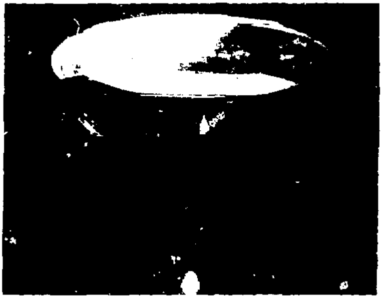

PREPARED FOR TESTING OR COATING

Fig. 32. Bruce profile electrode for emission suppression tests.

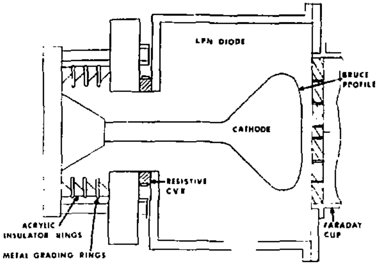

Fig. 33. Experimental set-up for emission suppression experiment.

Test results of the experiments are shown in Table IX where F_o is the maximum applied mean electric field at which no detectable emission occurred (<0.1 amp/cm^2), F_e refers to the mean electric field at which emission currents greater than 0.1 amp/cm^2 were detected, t_e is the time into the voltage pulse at which emission first became evident. Each value in the table has an associated rms standard deviation which is an indication of repeatability.

In order for a dielectric coating to be considered of value in suppressing electron emission, it must withstand a high electric field for a relatively long time; therefore the product $F_e t_e$ may be considered as a relative figure of merit when used in conjuction with the hold-off electric field (F_o). Of course, it is necessary that the standard deviation be small to insure reliable operation. A comparison of these qualities is required in order to select the coating which is the most beneficial.

Of the dielectric coatings tested, Krylon 1303 (Borden Chemical Co., Columbus, OH), Rustoleum epoxy paint (Rustoleum, Inc., Evanston, IL), and soft anodizing (a sulfuric acid process) seem to possess the best properties for the above criteria. Other coatings may meet the criteria in one category but not another. Krylon 1303 acrylic is easy to apply by spray to any metal but some samples did exhibit flaking after prolong testing. Control samples were cycled from vacuum to atmospheric pressure to see if the exposure to vacuum caused the flaking; however, no flaking occurred in this test. The flaking is probably due to poor preparation and application of the coating. Rustoleum can also be applied to any metal of unlimited size and shape but has the disadvantage of being a three coat process. Soft anodizing is limited to aluminum structures and does impose a practical size limitation although it is a relatively cheap process for small structures.

TABLE IX

Dielectric Strength of Various Coatings in Vacuum

Cathode Coating	F_o kV/cm	F_e kV/cm	t_e μs	$F_e t_e$
Polished Aluminum	154 ±24	[illegible]	[illegible]	[illegible]
Soft Anodize	236 ±30	[illegible]	[illegible]	[illegible]
Krylon Acrylic	227 ±11	[illegible]	[illegible]	[illegible]
Rustoleum Epoxy	219 ±[illegible]	[illegible]	[illegible]	[illegible]
Acrylic #2	207* ±28	[illegible]	[illegible]	[illegible]
X-500 Urethane	201 ± 7	[illegible]	[illegible]	[illegible]
H-22 Paint	194* ± 3	[illegible]	[illegible]	[illegible]
Glyptal Varnish	186 ±[illegible]	[illegible]	[illegible]	[illegible]
Epoxy Powder	183 ± C	[illegible]	[illegible]	[illegible]
Cat-A-Lac Epoxy	182* ± 1	[illegible]	[illegible]	[illegible]
Hard-coat Anodize	166 ±30	[illegible]	[illegible]	[illegible]

*Does not include one sample which withstood machine limit ([illegible] kV/cm) without emission.

PLASMA INJECTED, MICROSECOND E-BEAM DIODES

Vacuum Surface Flashover Tests

A bench test facility was built in which various configurations for vacuum surface flashover plasma sources were tested. The output of either a 50 ns, 50 Ω cable pulse, or a capacitive discharge pulser was fed into a vacuum chamber in which the surface flashover specimens were placed. The output switch was a manually activated, ball plane, oil dielectric switch. For these tests the test chamber was evacuated to less than 1 x 10^{-4} torr.

One class of flashover samples that were tested had the general configuration shown in Fig. 34. Insulating materials included acrylic board, fiberglass epoxy board, glass, and alumina ceramic. The cable pulser was used for these tests, and the charge voltage varied from 10-50 kV. The tests consisted of determining the number of channels/unit length produced when the high voltage pulse was applied to the sample. The best results were obtained with the highest charge voltage (50 kV) and smallest gap spacing (2 mm). No strong preference for either polarity was apparent. Glass and ceramic insulators gave better performance than acrylic or fiberglass epoxy. The number of channels produced using the fiberglass epoxy sample was significantly increased by undercutting the insulator surface at the gap by ~.01 cm. This procedure left a rough surface at the gap with a large number of exposed ends of the fiberglass filaments. The location of the arc channels was regularized by using a serrated edge on one of the electrodes. By placing graphite bridges across the gap, the location of the arc channels was further stabilized and the number of channels increased. Figure 35 is an open shutter photograph of a 7.6 cm long glass substrate sample.

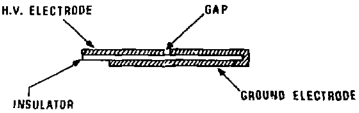

Fig. 34. General configuration of surface flashover sample.

A further extension of this technique is shown in Fig. 36. Here a 24 cm long fiberglass epoxy sample has two 0.32 cm gaps in series running the length of the board. The high voltage pulse is applied to the left gap. After this gap closes with a relatively small number of channels, a large number of channels are formed in the second gap. This phenomenon is analogous to multichannel switching where the first gap acts as a pulse sharpening switch. This technique appears to be a promising method for developing large area plasma sources.

Fig. 35. Open shutter photograph of 7.6 cm long glass substrate sample. The cable pulser was charged to 40 kV.

Fig. 36. Open shutter photograph of 24 cm long fiberglass epoxy board with two 0.32 cm gaps in series. The high voltage pulse was applied to the left side of the board.

A slightly different approach using printed circuit boards was also investigated. Figure 37 is a photograph of one such board. Each row of pads is independently fed from one end while the other end of the row is held at local ground. A series resistor is used on each row in order to limit the current flowing through the gaps and to maintain the voltage on the remaining rows once a row of gaps has completely closed. These boards were driven by a capacitive discharge pulser. Both fiberglass epoxy and "Kapton" boards were tested. As in the cases discussed above, better overall performance was obtained by placing a spot of graphite on each of the gaps. All of the gaps on the board shown in

Fig. 37. Sample printed circuit board used for large area plasma source.

Fig. 37 were simultaneously flashed over with a total stored energy of 0.5 J (10 nF and 10 kV). This represents a channel density of 1.8 channels/cm^2 over a total area of 240 cm^2. Problems encountered with this type of flashover plasma source include: arcing from one row to its neighbor row, arcing to the edges of the board, and incomplete breakdown along some of the rows. No significant performance differences were found for "Kapton" and fiberglass epoxy boards. Figure 38 is an open shutter photograph of the arcs formed on a 17 cm x 19 cm board containing 8 rows with 25 gaps in each row. An unexplained feature of this type of board can be seen in this figure. The first and last gaps of each row is much brighter than the remaining gaps in the row. The conditions for optimum operation of this type of plasma source has not been established, however, no problems have been found which would limit the overall size of a source when operating at the above channel density. Due to the small amount of energy dissipated in the gaps, no observable damage is done to the boards, thus making this type of source a promising candidate for repetitively pulsed applications.

A third approach to plasma sources was *a surface flashover across an acrylic* ring as shown in Fig. 39. The high voltage pulse was applied to the bottom electrode while the top electrode was held at ground. The center pins were connected to the bottom electrode either directly or through a series resistor. The surface flashover gaps were 2 mm. The acrylic insulator positioned and insulated each pin. The cable pulser was used for these tests. Even at 50 kV charge only about half of the gaps closed. Placing graphite across the gaps did not improve the number of closures. This technique is not very promising for making large area plasma sources.

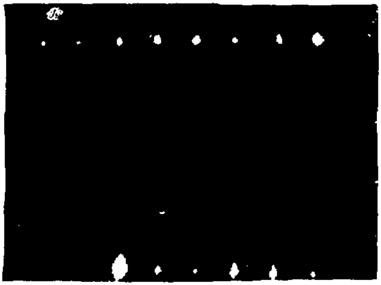

Fig. 38. Open shutter photograph of a 17 cm x 19 cm circuit board containing 200 gaps in eight rows.

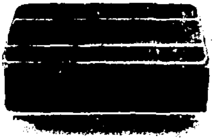

Fig. 39. Flashover sample using a pin array.

A fourth approach makes use of the high dielectric constant of barium titanate ($BaTiO_3$). A sketch of the geometry is shown in Fig. 40a. One end of a 2 nF, 40 kV capcitor has been removed to expose the $BaTiO_3$ surface. A guard ring is placed on this surface and held at ground while the high voltage pulse is applied to the opposite electrode of the capacitor. Figure 40b is an open shutter photograph of the resulting discharge when voltage is applied with the cable pulser. The surface discharges appears

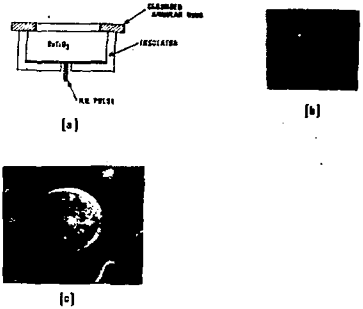

Fig. 40. a) Sketch of flashover sample using $BaTiO_3$.
b) Open shutter photograph of discharge on $BaTiO_3$ surface, cable pulser charged to 50 kV.
c) Discharge tracks left on carbon layer placed on top of $BaTiO_3$ surface.

to start at the edge of the ground electrode and to propagate inward. A test was made where the $BaTiO_3$ surface was coated with a thick layer of graphite. Figure 40c is a picture of the capacitor surface after firing. The performance of the device was essentially the same with or without the carbon coating. Further testing showed that the discharge channels always started at the edge of the ground electrode irrespective of the shape of this electrode. These tests indicated that it should be possible to make a large area plasma source using this technique.

Preliminary Tests Using Surface Flashover Plasma Source

Experiments were performed on the LEGS accelerator to determine the characteristics of a microsecond diode with a surface flashover plasma cathode. A $BaTiO_3$ capacitor, configured as shown in Fig. 40a was mounted on the cathode shank. The surface flashover discharge was driven coincident with the main diode voltage pulse.

LEGS has a four stage, pulse forming network (PFN) that applies a 1 μs voltage pulse to the diode (see Fig. 41). The voltage across the last stage of the PFN was used to drive the surface flashover plasma source. For these tests, the inductance across the last stage of the PFN, L3, was increased to obtain about 50 kV pulse to drive the plasma source. The remaining inductors in the PFN were adjusted to maintain, as closely as possible, the original voltage waveshape. Typical diode waveforms obtained using this setup are shown in Fig. 42. The resulting anode current density pattern was measured using radiochromic dosimetry; it showed a high density pattern (which closely reproduced the discharge pattern on the $BaTiO_3$ surface) superimposed on a circular pattern of uniform density.

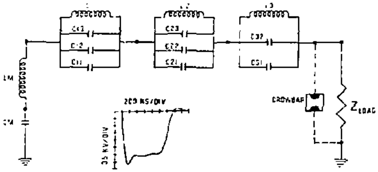

Fig. 41. Electrical schematic of LEGS pulser.

Fig. 42. Typical diode waveforms obtained for $BaTiO_3$ flashover source driven by voltage across last stage of PFN.

Some uncertainty existed as to the exact time at which the plasma was formed on the $BaTiO_3$ surface. The manner in which the flashover source was driven was changed to ensure that the cathode plasma was formed on the $BaTiO_3$ surface at the beginning of the diode voltage pulse. For this case, the rear electrode of the $BaTiO_3$ capacitor (originally driven by the last state of the PFN) was connected to ground via a 400 Ω, 1 KΩ or 2 KΩ resistor. Results obtained with the 1 KΩ and 2 KΩ resistors were similar to those obtained with the PFN driven plasma source described above. When a 400 Ω grounding resistor was used, a strong tendency for the diode to short late in the voltage pulse was observed; possibly due to a greater amount of plasma being fed into the diode by the flashover source.

These tests showed the feasibility of operating a plasma injected, microsecond electron beam diode to gain control of the diode impedance behavior. It was apparent, however, that significantly more control over plasma conditions was necessary than could be obtained with the above methods. A separate pulser was built capable of driving the plasma sources independent of the main diode voltage.

Tests with Independently Driven Surface Flashover Plasma Source

For these tests a plasma source utilizing a "KAPTON" board described earlier was used. This flashover board was placed inside a hollow cathode as shown in Fig. 43. The output of a capacitive discharge pulser was fed via a transit time isolator, through the center of the cathode shank, to the flashover board. The time between the firing of the plasma source and the application of the main diode voltage, ΔT, was made variable. The diode could thus be operated in a mode where the plasma was just entering the A-K gap through the screen mesh or in a partially or totally filled plasma diode mode. The density of the plasma in the gap was varied by changing the time delay, ΔT, between firing the plasma source and the main Marx. The screen mesh served the purpose of isolating the flashboard from the main diode voltage and defining the cathode equipotential.

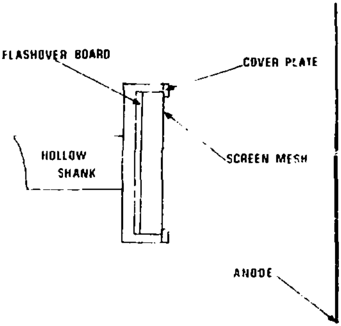

Fig. 43. Diode geometry for cathode with flashover board.

A large number of shots have been taken with this mode of operation to establish the general diode operating characteristics. An investigation of plasma filled diodes using conical theta pinch plasma guns was conducted on LEGS in conjunction with this study. Results from those investigations are presented in the following section. Many features of diode operating characteristics were found to be common to both the plasma guns and the vacuum surface flashover plasma sources. Conclusions and results common to both studies are presented in a separate section.

One of the first problesm encountered in using the surface flashover plasma source, with the configuration shown in Fig. 43, was the immediate and continued shorting of the diode. For these tests a 0.2 μF capacitor was used to drive the plasma source. It was apparent that too high a density plasma was being injected into the anode-cathode gap. It was determined that the amount of plasma generated could be changed by adding a current limited series resistor to the plasma trigger supply. The diode impedance behavior was found to be critically dependent on the value of this resistor and on ΔT. Eventually the 0.2 μF capacitor was replaced by a 10 nF capacitor. This capacitance value was found to be adequate for driving the flashover source; in fact shorts could still be obtained using this supply.

This dependence of the impedance behavior on ΔT can be seen from a series of shots shown in Fig. 44. All shots were taken with identical conditions except for the delay time. Delays of 1, 2, 3, 5 and 10 μs are shown. At 1 μs, plasma starts entering the gap sometime into the voltage pulse. At 2 μs some plasma is present in the gap when the voltage pulse is applied. As can be seen from the remaining waveforms, as the delay time is increased, the overall value of the current rises. Another apparent feature is that the leading edge of the current pulse becomes less sharp while the trailing edge of the pulse becomes more prominent at the longer delay times. Eventually the leading edge disappears entriely while the trailing edge remains. This feature is shown in Fig. 45 for a different set of initial plasma conditions and a time delay of 400 μs.

The dependence of the diode behavior on the energy delivered to the flashover plasma source is shown in Fig. 46. Two sets of data are shown here; taken with a time delay of 1 μs. The driver for the plasma source consisted of a 10 nF capacitor charged to 20 kV in one case and 15 kV in the other. The desired voltage and current waveforms were obtained at 15 kV charge, but at 20 kV charge the diode shorts halfway through the voltage pulse.

A number of shots were taken without the cathode screen. Without the screen, the diode tended to short more readily early in the voltage pulse. The screen evidently changes the properties of the plasma present in the anode-cathode gap, however, it also tended to light up at one or more discrete points. These hot spots resulted in non-uniform anode current densities as measured with radiochromic dosimetry material.

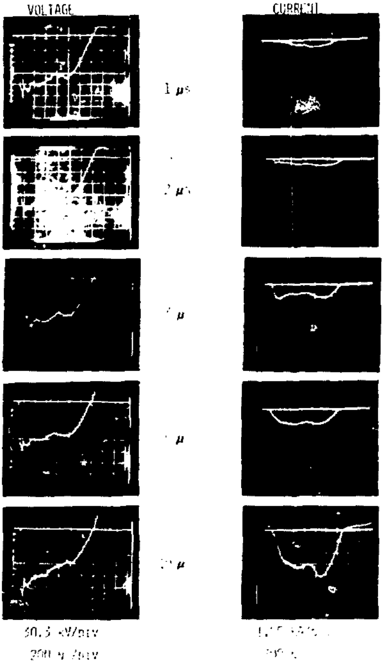

Fig. 44. Diode voltage and current waveforms obtained for various time delays.

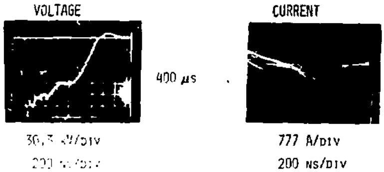

Fig. 45. Diode voltage and current waveforms obtained for long delay times.

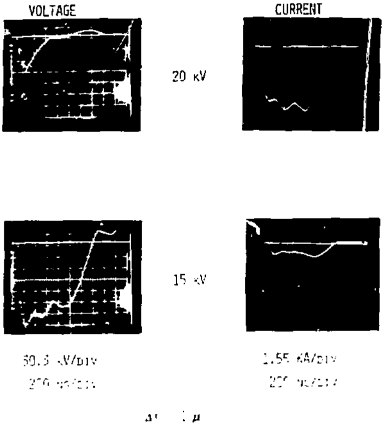

Fig. 46. Voltage and current waveforms as a function of energy delivered to flashover board.

Tests Using Plasma Guns

The objective of plasma injection into the diode using a flashover gun is to control the diode impedance in a manner which will produce temporally flat voltage and current waveforms and spatially uniform current density. The injection geometry is shown in Fig. 47. An insulator flashover gun developed by C. Mendel[21] emits a plasma which is typically a few microseconds wide with a bulk velocity of 5 cm/μs and a density of $\sim 10^{13}/\mathrm{cm}^3$ at a distance of 20 cm from the gun exit. This plasma expands as it passes down the drift tube and through the cathode mesh into the diode.

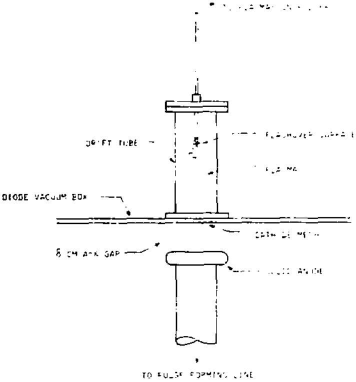

Fig. 47. Plasma gun experimental set-up.

A large number of factors which influence the diode behavior have been experimentally varied and the extent of their effect has been partially determined. These factors have been grouped together under five major headings: (1) Plasma Gun Driving Circuit, (2) Plasma Guns, (3) Machine Parameters, (4) Electrode Parameters, and (5) Operation.

1. Plasma Gun Driving Circuit

a. Capacitor Voltage

The voltage to which the driving capacitors are charged appears to be very important, with higher voltages allowing more plasma to be produced. Since the spark gap triggers unreliably below 14 kV, control of the plasma by altering the charging voltage is possible only over the range 15-20 kV.

b. Capacitor Size

The amount of plasma formed seems to be a direct function of stored energy. Values of .2 μf - 1.8 μf were used, with best results generally found at .2 μf per plasma gun.

c. Capacitor Charging Polarity

Delivering a negative pulse to the plasma gun center electrode has been found to be more effective in producing a fast rising plasma pulse than using a positive one. This may be partially understood in terms of the gun geometry which could allow for higher field emission with a negative pulse on the small inner conductor than the spiral shape outer conductor.

d. Plasma Gun Bias

The outer conductor of the plasma gun was biased ±300 volts from the potential of the drift tube and cathode mesh (ground). No effect of the bias was observed.

e. Series Resistance

The value of the series resistance placed in the plasma gun circuit has a very large effect in determining the amount of plasma which is injected into the diode. The mechanism of control is not fully understood, although the main influence seems to be that of a current limiting resistor. This is an easily varied parameter which can prevent most diode shorts.

2. Plasma Guns

a. Gun design

Figure 48 shows three modifications of the basic gun. The core angle determines the dispersion of the plasma. The best diode behavior is produced using a wide (120°) cone.

b. Gun-to-Cathode Distance

The uniformity of the plasma in the diode improves with drift distance while the density decreases. At small distances (1-3 cm) the diode often shorts. At large (30 cm) distances, the current rises slowly. At intermediate (10 cm) distances, the wide-angle guns seem to produce moderate density ($\sim 10^{13}/cm^3$) plasmas in the diode.

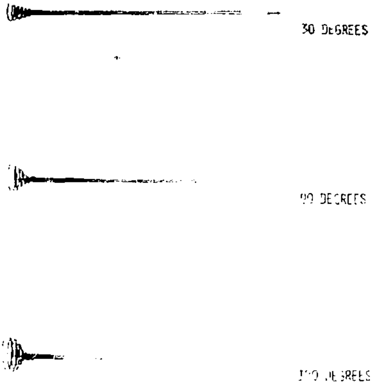

Fig. 48. Modified plasma gun.

c. Gun Coating

The teflon insulator in the rigid coax is coated with several layers of graphite to produce a carbon plasma at flashover. When 0.6 μf at 15 kV is used for each gun, the carbon coating life is ~10 shots. When 0.2 μf at 15 kV is used, the coating life is ~40-50 shots. When early diode shorts occur, part of the coating can be removed as a flake in a single shot.

3. Machine Parameters

a. Voltage Level

The voltage level to which the Marx is charged seems to have no appreciable effect on the magnitude of the impedance collapse. For lower voltages, the current rise occurs later in time but results in approximately the same final impedance, as seen from the diode current and voltage waveforms in Fig. 49.

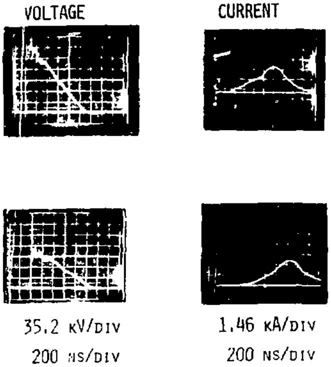

Fig. 49. Voltage and current waveforms vs. Marx charge voltage for plasma filled diode.

b. Delay Time

The main Marx pulse is delayed a number of microseconds from the time the plasma guns are fired. The diode behavior is a strong function of this delay. Presumably, the delay time determines the plasma density in the diode at the time of the main pulse and has some effect on current uniformity. The best performance occurs with delay times in the range 20-70 μs indicating that the diode performs best as a plasma filled diode. The effect of the delay is greatest with the most transparent cathode meshes. There is an optimum delay time for each series resistance in the plasma gun driving circuit. This is probably due to the control which both the resistance and delay time have on the plasma density in the diode.

c. Diode Residual Pressure

By using a controllable leak, the air pressure in the diode was varied. For series resistance in the gun circuit of 200-1000 Ω, a transition from routine diode operation to continued shorting was found to occur between 3×10^{-5} torr and 2.0×10^{-4} torr with the diode A-K gap set at 8 cm. Little benefit in terms of current uniformity in space or time was found by operating at pressures above the normal base pressure of $5\text{-}8 \times 10^{-5}$ torr.

4. Electrode Parameters

a. Cathode Mesh

The type of cathode mesh used has been found to have a strong effect on the ability to obtain temporally flat voltage and current waveforms. Figure 50 shows voltage and current waveforms for various delay times when no cathode mesh was used. Figure 51 shows the waveforms when a 50 percent transparent mesh was used. The most desirable current waveforms have two peaks of approximately equal size. The effect of a fine cathode mesh is to cut down the first peak and enhance the second, resulting in a decreasing impedance. High transparency meshes have a small, but noticeable effect.

5. Operation

a. Single Gun Operation

More than 280 diode shots have been taken with the single gun geometry (Fig. 47). These shots have given substantial indications of what does and does not work for obtaining flat waveforms, but have been generally unreproducible on a day-to-day basis to better than ~30 percent. The most reproducible shots have been those in which the drift tube was not covered by a cathode mesh. The waveforms, impedance, and electron energy spectrum from one of the better shots are shown in Fig. 52. A carbon anode was used in the shot with a gun-to-cathode mesh distance of 10 cm and a gun series resistance of 55 Ω.

b. Multiple Gun Operation

Three plasma guns with 120° cone angle were placed into drift tubes in a geometry similar to that in Fig. 47. An 8" x 20" (1000 cm^2) aluminum anode area, so that the current density remained constant. The value was

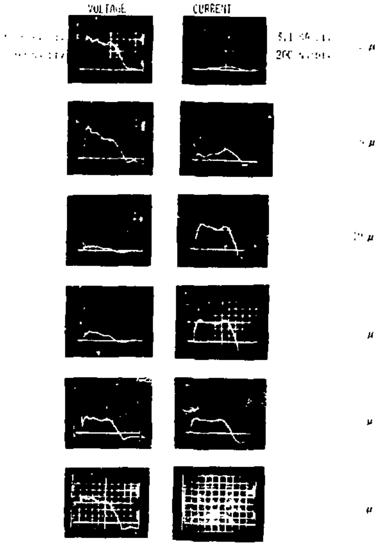

Fig. 50. Diode voltage and current waveforms vs. time of plasma injection without cathode mesh.

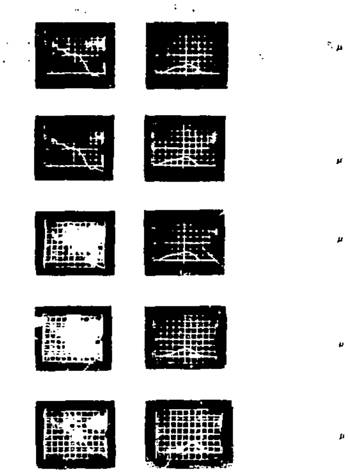

Fig. 51. Diode voltage and current waveforms vs. plasma injection time with 50 percent transparent cathode mesh.

~5-10 amps/cm^2 for diode voltages of 200-330 kV. The diode operated at impedances of 20-50 Ω. Reproducibility using the three gun geometry was improved over that using the single gun geometry.

c. Fast Framing Camera Observations

A fast framing camera was used to observe the optical emission from the diode. Figure 53 shows the progression (top-to-bottom) during a normal shot and during a short. The sequence is as follows:

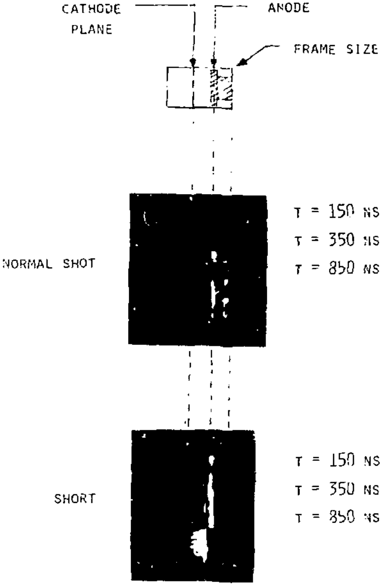

Fig. 52. Voltage, current, impedance, power and electron spectrum for single plasma gun shot.

Fig. 53. Framing camera experimental set-up.

(1) The anode lights up on the sides and at the back. There is no light observed at the cathode.

(2) The light at the anode brightens.

(3) If the shot is a short, visible light occurs at the anode front surface.

(4) The anode front surface plasma expands into the A-K gap at a rate of 3 cm/μs.

Summary and Conclusions

A number of techniques have been identified for generating large area plasmas; some of these have been used to study the operation characteristcs of plasma injected, microsecond, electron beam diodes. It has been established that these diodes can be made to display a wide range of impedance characteristcs by controlling the injected plasma conditions. The strongest control over diode impedance was obtained by adjusting the time between formation of the injected plasma and the application of the high voltage to the diode. It was determined that, within this wide dynamic operating range, it is possible to obtain temporally uniform voltage and current waveforms. Some spatial non-uniformities in anode current densities have been observed with radiochromic dosimetry. It does not appear that these non-uniformities are inherent to the operation of these diodes and thus it is expected that both spatial and temporal uniform current densities can be obtained using plasma injected diodes. Work is continuing to obtain a quantitative description of the performance of the various plasma sources and to obtain a model which describes the observed impedance behavior of these diodes.

REFERENCES

1. J. H. Nucholls, Tech. Digest of Topical Mtg. on Inertial Confinement Fusion, Feb. 7-9, 1978, San Diego, CA, Optical Society of America, Washington, DC (1977).
2. G. J. Rohwein, M. T. Buttram and K. R. Prestwich, Proc. of the 2nd Int'l. Topical Conf. on High Power Electron and Ion Beam Res. and Tech., Oct. 3-5, 1977, Cornell Univ., Ithaca, NY.
3. Electron Beam Fusion Progress Report, April-Sept. 1977, SAND78-0800, p. 169.
4. J. P. VanDevender, 1978 IEEE Int'l. Conf. on Plasma Sci., Monterey, CA, May 15-17, 1978, Paper 3A5-6.
5. P. Miller, et al., Phys. Rev. Letters 39 92 (1977).
6. D. L. Johnson, et al., 1978 IEEE Int'l. Conf. on Plasma Sci., Monterey CA, May 15-17, 1978, Paper 4A-8.
7. S. A. Goldstein, 1978 IEEE Int'l. Conf. on Plasma Sci., Monterey, CA, May 15-17, 1978, Paper 4A1-2.
8. P. A. Miller, et al., Proc. of the 2nd Int'l. Topical Conf. on High Power Electron and Ion Beam Res. and Tech., Oct. 3-5, 1977, J. Nation and R. Sudan Ed., Cornell Univ., Ithaca, NY.
9. Electron Beam Fusion Progress Report, Oct. 1976-March 1977, SAND77-1414, p. 143.
10. Electron beam Fusion Progress Report, April-Sept. 1977, SAND78-0800, p. 178.
11. J. C. Bower and S. C. Sedore, Sceptre, A Computer Program for Circuit and Systems Analysis, Prentice Hall, Inc., Englewood Cliff, NY, 1971.
12. D. L. Johnson and K. R. Prestwich, An 18 MV Marx Generator, IEEE Trans. Nucl. Sci., 1969.
13. Pulse Generators, Ed. by G. M. Glasoe and J. V. Lebacqz, Mass. Inst. of Tech. Rad. Lab. Series, Vol. 5, McGraw Hill Book Co., NY, 1948.
14. G. Yonas, et al., Nucl. Fusion, 14, No. 5 (1974).
15. G. W. Kuswa, et al., Proc. 2nd Int'l. Topical Conf. on High Power Electron and Ion Beam Res. and Tech., Cornell Univ., Oct., 1977.
16. F. Biggs, Sandia Laboratories Report SC-RR-71-0507.
17. S. L. Thompson, Sandia Laboratories Report SLA-73-0477.
18. Electron Beam Fusion Progress Report, April-Sept. 1977, SAND78-0800, p. 63.
19. Ibid, p. 201.
20. M. M. Widner, APS Plasma Phys. Mtg.,, Atlanta, GA, Nov. 1977.
21. C. W. Mendel and S. A. Goldstein, A Fast-Opening Switch for Use in REB Diode Experiments, J. Appl. Phys., Vol. 48, No. 3, March 1977, p. 1004.
22. P. A. Miller, et al., Phys. Rev. Lett. 35, No. 14, Oct. 6, 1975, p. 940.
23. F. M. Bruce, Proc. Inst. Elect. Engs. 94, (1947) 138.

PUBLICATIONS

ELECTRON BEAM DRIVEN IMPLOSIONS, L. Baker, M. J. Clauser, J. R. Freeman, S. A. Goldstein, L. P. Mix, J. N. Olsen, F. C. Perry, A. J. Toepfer, and M. M. Widner, Proc. of the 2nd International Topical Conf. on High Power Electron and Ion Beam Research and Technology, Cornell University, Ithaca, New York, October 3-5, 1977, p. 169.

HIGH POWER MAGNETICALLY INSULATED RADIAL DIODE, G. W. Kuswa, S. Humphries, D. J. Johnson, R. J. Leeper, and J. R. Freeman, Proc. of the 2nd International Topical Conf. on High Power Electron and Ion Beam Research and Technology, Cornell University, Ithaca, New York, October 3-5, 1977.

REB PROPAGATION AND COMBINATION IN PLASMA CHANNELS, P. A. Miller, L. Baker, J. R. Freeman, L. P. Mix, J. W. Poukey, and T. P. Wright, Proc. of 2nd International Topical Conf. on High Power Electron and Ion Beam Research and Technology, Cornell University, Ithaca, New York, October 3-5, 1977.

RECLAIMING SULFUR HEXAFLUORIDE -- A SYSTEM TO REPURIFY STORE, AND RECIRCULATE SF_6, G. E. Staller and M. F. Aker, Jr., SAND77-1127 (October 1977).

MECHANICAL ENGINEERING DESIGN CRITERIA FOR THE MAGNETICALLY INSULATED TRANSMISSION EXPERIMENT ACCELERATOR, G. E. Staller, I. D. Hamilton, M. F. Aker, and H. G. Fifer, SAND77-1958 (February 1978).

NEUTRON PRODUCTION FROM ADVANCED REB FUSION TARGETS, J. T. Chang, M. M. Widner, A. V. Farnsworth, R. J. Leeper, T. S. Prevender, and L. Baker, Proc. of the 2nd International Topical Conf. on High Power Electron and Ion Beam Research and Technology, Cornell University, Ithaca, New York, October 3-5, 1977, p. 195.

POWER FLOW STUDIES OF MAGNETICALLY INSULATED LINES, D. H. McDaniel, J. W. Poukey, K. D. Bergeron, J. P. VanDevender, and D. L. Johnson, Proc. of the 2nd International Topical Conf. on High Power Electron and Ion Beam Research and Technology, Cornell University, Ithaca, New York, October 3-5, 1977.

EBFA-II CONCEPTUAL DESIGN PROPOSAL, G. W. Barr and G. Yonas (March 1978).

DATA ACQUISITION AND PROCESSING ON ELECTRON BEAM FUSION ACCELERATORS, W. B. Boyer, IEEE Trans. Nuc. Sci., NS-25, 1 (February 1978).

ELECTRON DEPOSITION IN THIN TARGETS, M. M. Widner, M. J. Clauser, J. W. Poukey, J. P. Quintenz, E. J. T. Burns, L. P. Mix, F. C. Perry, A. J. Toepfer, Proc. of the 2nd International Topical Conf. on High Power Electron and Ion Beam Research and Technology, Cornell University, Ithaca, New York, October 3-5, 1977.

DESIGN AND DEVELOPMENT OF A 350 kV, 100 pps ELECTRON BEAM ACCELERATOR, G. J. Rohwein, M. T. Buttram, and K. R. Prestwich, Proc. of the 2nd International Topical Conf. on High Power Electron and Ion Beam Research and Technology, Cornell University, Ithaca, New York, October 3-5, 1977.

E-BEAMS FOR LASER EXCITATION, J. J. Ramirez, K. R. Prestwich, R. S. Clark, and M. T. Buttram, Proc. of the 2nd International Topical Conf. on High Power Electron and Ion Beam Research and Technology, Cornell University, Ithaca, New York, October 3-5, 1977.

DESIGN OF THE BLANKET AND SHIELD FOR A HIGH-FIELD COMPACT TOKAMAK REACTOR (HFCTR), D. L. Cook, L. M. Lidsky, S. Herring, W. Stephany, Proc. of the 7th Symposium on Engineering Problems of Fusion Research, Knoxville, Tennessee, October 25-28, 1977.

ELECTRON BEAM TARGET DESIGN EMPLOYING AN ELECTRICALLY PREHEATED, MAGNETICALLY INSULATED FUEL PLASMA, M. M. Widner and A. V. Farnsworth, SAND77-1585 (October 26, 1977).

BREAKEVEN FUSION TARGETS CONTAINING PREHEATED FUEL AND LARGE MAGNETIC FIELDS, A. V. Farnsworth and M. M. Widner, SAND77-1583 (October 1977).

INTENSE ION BEAM ACCELERATION AND TRANSPORT, S. Humphries, Proc. of 2nd International Topical Conf. on High Power Electron and Ion Beam Research and Technology, Cornell University, Ithaca, New York, October 3-5, 1977.

HIGH CURRENT PULSED LINEAR ION ACCELERATORS, S. Humphries, J. Appl. Phys., 49, 2, 501 (February 1978).

THE CORNELL INTENSE ION BEAM PROGRAM, S. Humphries, Jr., P. L. Dreike, C. B. Eichenberger, J. Friedman, D. A. Hammer, R. V. E. Lovelace, J. E. Maenchen, A. Mankovsky, E. Ott, R. N. Sudan, and L. G. Wiley, Proc. of the 2nd International Topical Conf. on High Power Electron and Ion Beam Research and Technology, Cornell University, Ithaca, New York, October 3-5, 1977.

HIGH POWER ION DIODES FOR INERTIAL CONFINEMENT FUSION EXPERIMENTS, D. J. Johnson and G. W. Kuswa, RS 5244/1003, Internal Memorandum (January 1978).

IONIZATION FRONT ACCELERATOR FEASIBILITY INVESTIGATIONS, C. L. Olson, J. P. VanDevender, and A. Owyoung, Proc. of the 2nd International Topical Conf. on High Power Electron and Ion Beam Research and Technology, Cornell University, Ithaca, New York, October 3-5, 1977.

THERMODYNAMIC INCONSISTENCY OF THE MODIFIED SAHA EQUATION AT HIGH PRESSURES, M. A. Sweeney, Astrophysical Journal, 220, 335 (February 1978).

PULSED POWER CONVERSION WITH INDUCTIVE STORAGE, Proc. of the 7th Symposium on Engineering Problems of Fusion Research, Vol. II, p. 1049, IEEE Pub. No. 77 CH 1267-4-NPS, Knoxville, Tennessee, October 1977. (T. P. Wright)

LOW ν/γ BEAM HANDLING TECHNIQUE USING ASYMMETRIC CUSP MAGNETIC FIELDS, T. P. Wright, SAND77-2076 (January 1978).

SPACE CHARGE EFFECTS IN LONG COAXIAL VACUUM TRANSMISSION LINES, J. W. Poukey and K. D. Bergeron, Appl. Phys. Lett., 32, 1, 8 (January 1978).

CALCULATIONS FOR THE RADIAL LINE ELECTRON ACCELERATOR, J. W. Poukey, RS 5241/240, Internal Memorandum (March 1978).

PRESENTATIONS

PARTICLE BEAM FUSION PROGRAM AT SANDIA LABORATORIES, G. Yonas, Accelerator Technology Workshop, Lawrence Livermore Laboratory, Livermore, California, January 25-27, 1977.

PARTICLE BEAM FUSION PROGRAM AT SANDIA LABORATORIES, G. Yonas, 1977 Particle Accelerator Conference, Chicago, Illinois, March 16, 1977.

SANDIA'S RECENT RESULTS IN PARTICLE BEAM RESEARCH, G. Yonas, 8th European Conf. on Controlled Fusion and Plasma Physics, Prague, Czechoslovakia, September 19-23, 1977.

THE SANDIA PARTICLE BEAM FUSION PROGRAM, G. Yonas, Seminar Presentation, Lawrence Livermore Laboratory, Livermore, California, October 18-19, 1977.

ELECTRON BEAM PROPAGATION, G. Yonas, ABRES Nuclear Technical Interchange Panel (ANTIP) Meeting, Los Alamos, NM, November 2-3, 1977.

PARTICLE BEAM FUSION RESEARCH AT SANDIA, G. Yonas, U.S./IAEA Conference on Inertial Confinement Fusion, San Francisco, California, February 1-3 and 6, 1978.

ELECTRON AND ION BEAM INERTIAL CONFINEMENT FUSION IN THE UNITED STATES, G. Yonas, Topical Meeting on Inertial Confinement Fusion, San Diego, California, February 7-9, 1978.

THE STATUS OF INERTIAL CONFINEMENT FUSION RESEARCH BASED ON PARTICLE BEAMS, G. Yonas, Foster Panel Presentation, Washington, DC, March 14, 1978.

FUSION POWER USING PARTICLE BEAMS, G. Yonas, Princeton University Colloquium, Princeton, New Jersey, March 16-17, 1978.

ELECTRON BEAM DRIVEN IMPLOSIONS, L. Baker, M. J. Clauser, J. R. Freeman, L. P. Mix, J. N. Olsen, F. C. Perry, A. J. Toepfer, and M. M. Widner, 2nd Topical Conf. on High Power Electron and Ion Beam Research and Technology, Cornell University, Ithaca, New York, October 3-5, 1977.

HIGH POWER MAGNETICALLY INSULATED RADIAL DIODE, G. W. Kuswa, S. Humphries, D. J. Johnson, R. J. Leeper, and J. R. Freeman, 2nd Topical Conference on High Power Electron and Ion Beam Research and Technology, Cornell University, Ithaca, New York, October 3-5, 1977.

REB PROPAGATION AND COMBINATION IN PLASMA CHANNELS, P. A. Miller, L. Baker, J. R. Freeman, L. P. Mix, J. W. Poukey and T. P. Wright, 2nd Topical Conf. on High Power Electron and Ion Beam Research and Technology, Cornell University, Ithaca, New York, October 3-5, 1977.

HEURISTIC MODEL FOR NONLINEAR RAYLEIGH-TAYLOR INSTABILITY, L. Baker and J. R. Freeman, Plasma Physics Meeting of the American Physical Society, Atlanta, Georgia, November 7-11, 1977.

RAYLEIGH-TAYLOR INSTABILITY OF A SHOCK-ACCELERATED INTERFACE, L. Baker and J. R. Freeman, 1978 Annual Meeting of the APS/AAPT, San Francisco, California, January 23-26, 1978.

REB PINCHING, TRANSPORT, AND COMBINATION IN PLASMA CHANNELS FOR ICF, P. A. Miller, L. Baker, J. R. Freeman, L. P. Mix, J. W. Poukey and T. P. Wright, Inertial Confinement Fusion Meeting, San Diego, California, February 7-9, 1978.

HYDRODYNAMICS OF PARTICLE BEAM BLOWOFF PLASMA, A. V. Farnsworth, Jr., M. M. Widner, M. J. Clauser, and K. E. Laungren, Plasma Physics Meeting of the American Physical Society, Atlanta, Georgia, November 7-11, 1977.

NEUTRON PRODUCTION FROM ADVANCED REB FUSION TARGETS, J. T. Chang, M. M. Widner, A. V. Farnsworth, Jr., R. J. Leeper and T. S. Prevender, 2nd International Topical Conference on High Power Electron and Ion Beam Research and Technology, Cornell University, Ithaca, New York, October 3-5, 1977.

RECENT DEVELOPMENTS IN PARTICLE BEAM INERTIAL CONFINEMENT FUSION, A. V. Farnsworth, Jr., presented as a Seminar at the College of Engineering, Arizona State University, Tempe, Arizona, December 2, 1977.

PARTICLE BEAM TARGETS CONTAINING PREHEATED FUEL AND MAGNETIC FIELDS, A. V. Farnsworth, Jr., M. M. Widner, L. Baker, R. J. Leeper, J. T. Chang, and J. N. Olsen, CLEOS/Inertial Confinement Fusion Meeting, San Diego, California, February 7-9, 1978.

EFFECTS OF TURBULENCE ON THE RAYLEIGH-TAYLOR INSTABILITY, M. J. Clauser and L. Baker, Plasma Physics Meeting of the American Physical Society, Atlanta, Georgia, November 7-11, 1977.

TARGET EXPERIMENTS ON PROTO I, J. W. Poukey, Plasma Physics of the American Physical Society, Atlanta, Georgia, November 7-11, 1977.

ENHANCED ELECTRON DEPOSITION IN FOILS, J. W. Poukey, Plasma Physics of the American Physical Society, Atlanta, Georgia, November 7-11, 1977.

TIME DEPENDENT COAX CALCULATIONS, J. W. Poukey, Plasma Physics of the American Physical Society, Atlanta, Georgia, November 7-11, 1977.

NONUNIFORM MESH DIODE SIMULATION CODE, J. W. Poukey, Plasma Physics of the American Physical Society, Atlanta, Georgia, November 7-11, 1977.

IONIZATION FRONT ACCELERATOR FEASIBILITY INVESTIGATIONS, C. L. Olson, J. P. VanDevender, and A. Owyoung, 2nd International Topical Conference on High Power Electron and Ion Beam Research and Technology, Cornell University, Ithaca, New York, October 3-5, 1977.

ELECTRON DEPOSITION IN THIN TARGETS, M. M. Widner, M. J. Clauser, J. W. Poukey, J. P. Quintenz, E. J. T. Burns, L. P. Mix, F. C. Perry, A. J. Toepfer, S. A. Goldstein, J. N. Olsen, and J. A. Halbleib, 2nd International Topical Conference on High Power Electron and Ion Beam Research and Technology, Cornell University, Ithaca, New York, October 3-5, 1977.

VOLTAGE SHAPING WITH ELECTRON-BEAM TARGETS, M. A. Sweeney and M. J. Clauser, Plasma Physics of the American Physical Society, Atlanta, Georgia, November 7-11, 1977.

TARGET EXPERIMENTS ON PROTO I, L. P. Mix, E. J. T. Burns, M. J. Clauser, S. A. Goldstein, R. J. Leeper, C. W. Mendel, J. N. Olsen, J. W. Poukey and J. P. Quintenz, Plasma Physics Meeting of the American Physical Society, Atlanta, Georgia, November 7-11, 1977.

TURBULENT STABILIZATION AND RECENT SOVIET TARGET DESIGNS, M. J. Clauser, USERDA Meeting on Thin Shell Targets, Los Alamos Scientific Laboratory, Los Alamos, NM, March 3, 1977.

EFFECTS OF TURBULENCE ON THE RAYLEIGH-TAYLOR INSTABILITY, M. J. Clauser and L. Baker, Colloquium at P. N. Lebedev Physical Institute, Moscow, USSR, September 26, 1977.

IMPLODING PLASMA RADIATION SOURCES, M. J. Clauser, USERDA Inertial Confinement Fusion Target Meeting, Las Vegas, Nevada, October 13-14, 1977.

RECENT TARGET RESULTS AT SANDIA, M. J. Clauser, Heavy Ion Fusion Workshop, Lawrence Livermore Laboratory, Livermore, California, December 7, 1977.

TARGETS FOR HEAVY ION FUSION, M. J. Clauser, Symposium on Relativistic Heavy Ion Research, Darmstadt, West Germany, March 7-10, 1978.

EXPERIMENTAL INVESTIGATIONS OF SHOCK-FOCUSING AND DOUBLE-SHELL TARGETS, F. C. Perry, M. M. Widner, M. A. Sweeney, R. J. Leeper, and A. J. Toepfer, Plasma Physics Meeting of the American Physical Society, Atlanta, Georgia, November 7-11, 1977.

SHOCK-FOCUSING TARGETS, M. A. Sweeney, Albino Consultants Panel Meeting, Los Alamos Scientific Laboratory, Los Alamos, New Mexico, August 9, 1977.

MATERIAL RESPONSE MEASUREMENTS ON RELATIVISTIC ELECTRON BEAM TARGETS, L. P. Mix, F. C. Perry, A. J. Toepfer, and M. M. Widner, APS General Meeting, San Francisco, California, January 22-26, 1978.

SANDIA PULSED POWER PROGRAM, T. H. Martin, DNA Advanced Concepts Review Meeting, NELC, San Diego, California, March 28-31, 1977.

SUPER POWER GENERATORS, T. H. Martin, D. L. Johnson, and D. H. McDaniel, 2nd International Topical Conference on High Power Electron and Ion Beam Research and Technology, Cornell University, Ithaca, New York, October 3-5, 1977.

PULSED POWER TECHNOLOGY, T. H. Martin, Invited Colloquium at Lawrence Livermore Laboratories, Livermore, California, October 21, 1977.

PULSED TECHNOLOGY FOR FUSION EXPERIMENTS, T. H. Martin, D. L. Johnson and D. H. McDaniel, Inertial Confinement Fusion Meeting, San Diego, California, February 7-9, 1978.

E-BEAM FOR LASER EXCITATION, J. J. Ramirez, K. R. Prestwich, R. S. Clark and M. T. Buttram, 2nd International Topical Conference on High Power Electron and Ion Beam Research and Technology, Cornell University, Ithaca, New York, October 3-5, 1977.

DESIGN AND DEVELOPMENT OF A 350 kV, 100 pps ELECTRON BEAM ACCELERATOR, G. J. Rohwein, M. T. Buttram, and K. R. Prestwich, 2nd International Topical Conference on High Power Electron and Ion Beam Res. & Tech., Cornell University, Ithaca, New York, October 3-5, 1977.

RADIAL PULSE LINE ACCELERATORS, K. R. Prestwich, Seminar AFWL, Albuquerque, New Mexico, October 14, 1977.

STUDIES ON MICROSECOND, E-BEAM DIODES OPERATING AT LOW ELECTRIC FIELDS AND CURRENT DENSITIES, R. S. Clark, J. J. Ramirez and K. R. Prestwich, Plasma Physics Meeting of the American Physical Society, Atlanta, Georgia, November 7-11, 1977.

DEVELOPMENT OF HIGH AVERAGE POWER DRIVER TECHNOLOGY FOR THE INERTIALLY CONFINED FUSION (ICF), K. R. Prestwich, M. T. Buttram, G. J. Rohwein, Topical Meeting on Inertial Confinement Fusion, San Diego, California, February 7-9, 1978.

STABILITY AND PERFORMANCE OF ELECTRON BEAM FUSION MODEL TARGETS, F. C. Perry, L. P. Mix, and A. J. Toepfer, APS General Meeting, San Francisco, California, January 22-26, 1978.

STABILITY OF THIN FOIL ACCELERATED BY A HIGH VELOCITY PISTON WORKING ON A LOW DENSITY GAS, A. J. Toepfer and W. J. Tiffany, APS General Meeting, San Francisco, California, January 22-26, 1978.

ADVANCES IN ELECTRON AND ION BEAM FUSION, A. J. Toepfer, APS General Meeting, San Francisco, California, January 22-26, 1978 (Invited Paper).

STABILITY OF MULTIPLE SHELL ICF CAPSULES, A. J. Toepfer, and W. Tiffany, Topical Meeting on Inertial Confinement Fusion, San Diego, California, February 7-9, 1978.

HIGH POWER MAGNETICALLY INSULATED RADIAL DIODE, G. W. Kuswa, S. Humphries, D. J. Johnson, R. J. Leeper, and J. R. Freeman, 2nd Topical Conference on High Power Electron and Ion Beam Research and Technology, Cornell University, Ithaca, New York, October 3-5, 1977.

A HIGH RESOLUTION TIME RESOLVABLE FLASH X-RADIOGRAPHY SYSTEM, J. T. Chang, G. W. Kuswa, and C. W. Mendel, Topical Meeting on Inertial Confinement Fusion, San Diego, California, February 7-9, 1978.

POWER FLOW STUDIES OF MAGNETICALLY INSULATED LINES, D. H. McDaniel, J. W. Poukey, K. D. Bergeron, J. P. VanDevender, and D. L. Johnson, 2nd International Topical Conference on High Power Electron and Ion Beam Research and Technology, Cornell University, Ithaca, New York, October 3-5, 1977.

THEORY OF DOUBLE SHEATHS IN PLASMAS, K. D. Bergeron and T. P. Wright, Plasma Physics Meeting of the American Physical Society, Atlanta, Georgia, November 7-11, 1977.

DATA ACQUISITION AND PROCESSING ON ELECTRON BEAM FUSION ACCELERATORS, W. B. Boyer, IEEE Nuclear Science Symposium, San Francisco, California, October 19-21, 1977.

DATA ACQUISITION REQUIREMENTS FOR SANDIA'S E-BEAM FUSION, W. B. Boyer, Workshop on CCD Applications to Transient Digitizer, Lawrence Livermore Laboratory, Livermore, California, January 24-25, 1978.

CURRENT DENSITY AND ELECTRON BEAM TARGET TEMPERATURE MEASUREMENTS ON PROTO I, E. J. T. Burns, S. A. Goldstein, J. N. Olsen, and L. P. Mix, Plasma Physics Meeting of the American Physical Society, Atlanta, Georgia, November 7-11, 1977.

TEMPERATURE OF THIN FOIL HEATED BY RELATIVISTIC ELECTRON BEAM, J. N. Olsen, E. J. T. Burns, and S. A. Goldstein, Plasma Physics Meeting of the American Physical Society, Atlanta, Georgia, November 7-11, 1977.

AN EXPERIMENTAL STUDY OF CURRENT INSTABILITY IN RELATIVISTIC ELECTRON BEAM DIODES, M. T. Buttram and R. S. Clark, Plasma Physics Meeting of the American Physical Society, Atlanta, Georgia, November 7-11, 1977.

MICROWAVE SCATTERING FROM NEEDLE CATHODE BURSTS, C. W. Mendel and M. T. Buttram, Plasma Physics Meeting of the American Physical Society, Atlanta, Georgia, November 7-11, 1977.

THE RESPONSE OF HEAVILY SHIELDED PLASTIC SCINTILLATOR-PHOTOMULTIPLIER COMBINATIONS TO NANOSECOND NEUTRON PULSES, R. J. Leeper, and J. T. Chang, Plasma Physics Meeting of the American Physical Society, Atlanta, Georgia, November 7-11, 1977.

A SHORT PULSE NEUTRON SOURCE, J. T. Chang, and R. J. Leeper, Plasma Physics Meeting of the American Physical Society, Atlanta, Georgia, November 7-11, 1977.

SCINTILLATOR-PHOTOMULTIPLIER RESPONSE TO A SIMULATED REB GENERATED THERMONUCLEAR NEUTRON PULSE, R. J. Leeper, and J. T. Chang, Topical Meeting on Inertial Confinement Fusion, San Diego, California, February 7-9, 1978.

DESIGN OF THE BLANKET AND SHIELD FOR A HIGH FIELD COMPACT TOKAMAK REACTOR (HFCTR), D. L. Cook, L. M. Lidsky, S. Herring, W. Stephany, 7th Symposium on Engineering Problems of Fusion Research, Knoxville, Tennessee, October 25-28, 1977.

ELECTRON BEAM PINCHING EXPERIMENTS ON THE PROTO II ACCELERATOR, S. A. Goldstein, P. A. Miller, D. H. McDaniel, and D. J. Johnson, Plasma Physical Meeting of the American Physical Society, Atlanta, Georgia, November 7-11, 1977.

ELECTRON BEAM PINCHING FROM DISCRETE LARGE DIAMETER CATHODES, C. W. Mendel, and S. A. Goldstein, Inertial Confinement Fusion Meeting, San Diego, California, February 7-9, 1978.

PROBLEMS OF INTENSE ION BEAM TRANSPORT, S. Humphries, Jr., 2nd International Topical Conference on High Power Electron and Ion Beam Research and Technology, Cornell University, Ithaca, New York, October 3-5, 1977.

THE CORNELL INTENSE ION BEAM PROGRAM, S. Humphries, Jr., P. L. Dreike, C. B. Eichenberger, A. Friedman, D. A. Hammer, R. V. E. Lovelace, J. E. Maenchen, A. Mankovsky, E. Ott, R. N. Sudan, and L. G. Wiley, 2nd International Topical Conference on High Power Electron and Ion Beam Research and Technology, Cornell University, Ithaca, New York, October 3-5, 1977.

MAGNETICALLY INSULATED INTENSE ION BEAM ACCELERATORS FOR FUSION APPLICATIONS, S. Humphries, Jr., Plasma Physics Meeting of the American Physical Society, Atlanta, Georgia, November 7-11, 1977, Invited Paper.

FOCUSING AND STEERING OF INTENSE ION BEAMS IN A CYLINDRICAL MAGNETICALLY INSULATED DIODE, S. Humphries, Jr., M. Greenspan, and R. N. Sudan, Plasma Physics Meeting of the American Physical Society, Atlanta, Georgia, November 7-11, 1977.

PROPAGATION AND FOCUSING OF INTENSE PULSED PROTON BEAMS FROM A MAGNETICALLY INSULATED FIELD INCLUSION DIODE, S. Humphries, L. Wiley, J. Maenchen, and R. N. Sudan, Plasma Physics Meeting of the American Physical Society, Atlanta, Georgia, November 7-11, 1977.

INTENSE PULSED LINEAR ION ACCELERATORS FOR INERTIAL FUSION, S. Humphries, Jr., Topical Meeting on Inertial Confinement Fusion, San Diego, California, February 7-9, 1978.

PRODUCTION OF FOCUSED ION BEAMS FOR INERTIAL CONFINEMENT FUSION BY MEANS OF MAGNETICALLY INSULATED DIODES, S. Humphries, Jr., M. Greenspan, D. Hammer, J. Maenchen, R. N. Sudan, and L. Wiley, Topical Meeting on Inertial Confinement Fusion, San Diego, California, February 7-9, 1978.

THE SANDIA LABORATORIES DIAGNOSTIC SYSTEM FOR PARTICLE BEAM FUSION EXPERIMENTS, R. J. Leeper, 2nd Topical Conference on High Temperature Plasma Diagnostics, Santa Fe, New Mexico, March 1-3, 1978, Invited Paper.

ION ACCELERATION IN A TRAVELING VIRTUAL CATHODE, R. B. Miller, Plasma Physics Meeting of the American Physical Society, Atlanta, Georgia, November 7-11, 1977.

EXCITATION OF Xe_2 EXCIMERS WITH A RADIALLY CONVERGING ELECTRON BEAM, A. W. Johnson, and J. J. Ramirez, Plasma Physics Meeting of the American Physical Society, Atlanta, Georgia, November 7-11, 1977.

ENERGY DEPOSITION E-BEAM EXCITED GAS LASER SYSTEMS - THEORY VS. EXPERIMENT, J. J. Ramirez, and J. A. Halbleib, Sr., Plasma Physics Meeting of the American Physical Society, Atlanta, Georgia, November 7-11, 1977.

POWER FLOW STUDIES FOR FUSION ORIENTED PARTICLE ACCELERATORS, J. P. VanDevender, Inertial Confinement Fusion Meeting, San Diego, California, February 7-9, 1978.

PULSED POWER CONVERSION WITH INDUCTIVE STORAGE, T. P. Wright, 7th Symposium on Engineering Problems of Fusion Research, Knoxville, Tennessee, October 1977.

REB PROPAGATION AND COMBINATION IN PLASMA CHANNELS, T. P. Wright. 2nd International Topical Conference on High Power Electron and Ion Beam Research and Technology, Cornell University, Ithaca, New York, October 3-5, 1977.

PARTICLE BEAM FUSION PROJECT, G. W. Barr, Division of Laser Fusion Program Manager's Meeting, Sandia Laboratories, November 1977.